1-1-2006

Improvement of titanium-aluminum-vanadium alloy wear resistance in vacuum using the thermal oxidization method.

Mohammad Mehdi Yazdanian
University of Windsor

IMPROVEMENT OF Ti-6Al-4V ALLOY WEAR RESISTANCE IN VACUUM USING THE THERMAL OXIDIZATION METHOD

By

Mohammad Mehdi Yazdanian

A Thesis
Submitted to the Faculty of Graduate Studies and Research
through Engineering Material
in Partial Fulfillment of the Requirements for
the Degree of Master of Applied Science at the
University of Windsor

Windsor, Ontario, Canada

2006

Your file Votre référence
ISBN: 978-0-494-35947-1
Our file Notre référence
ISBN: 978-0-494-35947-1

ABSTRACT

Dry sliding wear of surface treated Ti-6Al-4V alloy using a thermal oxidization method examined using a ball-on-disk tribo-tester built in-house to perform tests under vacuum of 7×10^{-6} torr. 52100 steel, Ti-6Al-4V and thermally oxidized Ti-6Al-4V were used as counterfaces. For comparison, the same tests were performed in ambient air. Tribological behaviour of treated Ti-alloy was investigated by means of SEM, EDS, XRD. The excellent enhancement in wear of thermally oxidized Ti-6Al-4V alloy was observed while they were in contact with a ball of the same material in high vacuum. Also, thermally oxidized samples tested against themselves in vacuum showed the lowest coefficient of friction and minimum counterface damage. However, a shift from adhesion wear for untreated Ti-alloy to abrasive wear was encountered in treated samples tested in vacuum. In addition, the dry sliding wear between surface treated Ti-6Al-4V and 52100 steel balls caused severe damage at the tip of counterface.

TABLE OF CONTENTS

LIST OF TABLES

LIST OF FIGURES

CHAPTER II

CHAPTER IV

CHAPTER V

Appendix A

Appendix C

Nomenclature

For the sake of completeness, the most relevants notation used in this thesis are summarized below:

A	Real area
A_n	apparent contact are
A_p	Arrhenius constant
a	Thermal diffusity
b	Burger vector
C	Constant used in the model for mild oxidational wear
d_c	Size of the cell or grain size
f	fraction of oxygen in the oxide film
$\tilde{F}$	Normalized force
k	Locking parameter (it measures the relative hardening contribution of grain boundary)
H	Indentation hardness of the soft surface
H_o	Hardness at room temperature
K	Wear coefficient
m	Mass of the disk holder
Q	Volumetric wear rate:
Q_o	Activation energy
R	Molar gas constant
R_d	Radius of disk (wear track)
R_n	Resistance of strain gauge
r_o	Radius of circular nominal contact area
r_p	Radius of pin (ball)
T_c	Temperature of real contact
t	Time
V	Velocity / Volumetric wear loss according to the ASTM standard G99
V_{in}	Input voltage
V_{out}	Output voltage

$\tilde{V}$	Normalized velocity
v	Dislocation velocity
W	Normal Load:
$\tilde{W}$	Normalized wear rate
w	Width of wear track
Z_c	Critical film (oxide) thickness
ε	Strain
$\dot{\varepsilon}_d$	Plastic deformation rate
ε_o	Constant
$\dot{\varepsilon}_r$	Plastic deformation rate
σ_e	External stress
σ_f	Flow stress at the strain ε
σ_i	Internal stress
σ_s	Yield stress / Saturation stress (the stress at which work-hardening becomes zero)
σ_o	Internal friction stress during dislocation motion / Bulk flow strength
$\dot{\rho}$	Rate of dislocation
ρ	Density of oxide
λ	Length of dislocations
τ_n	Torque (n=1, 2, 3) (1: the net torque of the rotational disk, 2: the applied torque, 3: the initial torque of rotary shaft
μ	Coefficient of friction

CHAPTER I

INTRODUCTION

Wear mechanisms and frictional behaviour of metals and their alloys are greatly affected by the atmospheric conditions. Among the wear mechanisms, oxidative wear has been observed while dry or lubricant sliding process taken place in ambient air, or in a corrosive media [1-7]. Applied load and sliding velocity strongly affect the oxidation phenomenon [2, 3, 8, 9]. The presence of oxygen leads to the creation of the thin oxide film on the metal surfaces [10]. That provides protection against surface damage during the sliding between two metal surfaces [11]. Thus, elimination or reduction in amount of oxygen from the environment around the contact surfaces is expected to increase adhesion between metallic mating surfaces. As the surfaces robbed on each other, strong metallic bonds create on the contact surface. The metallic particles become transferred from one surface to another while they are pulled apart [8].

The sliding contact of materials, in low atmospheric pressure, commonly occurs in space and aerospace engineering. Titanium and its alloys have vast applications in these industries for their high strength at room and elevated temperature and excellent chemical properties. Yet, they have a reputation for having poor tribological characteristics [12]. Studies have shown that oxidative and delamination types of wear occur in dry sliding wear of the Ti-6Al-4V alloy in air [13-14]. On the other hand, massive plastic deformation takes place in vacuum [14]. During this process material at the contact spots can be easily deformed due to the mechanical and adhesive forces applied by the counterface [12, 14]. Recently, a new surface treatment has been developed in order to enhance the wear resistance of titanium and its alloy. The treatment consists of thermal oxidization (TO) of titanium and its alloys, i.e. Ti-6Al-4V can be heated at 600 °C in ambient air for 60 to 70 hr [15-18]. The resulting TO-treated Ti-6Al-4V has improved wear resistance compared to untreated Ti-6Al-4V [4, 15-18].

However, tribological characteristics of TO-treated Ti-alloys have not been addressed under low atmospheric pressure. Therefore, investigation of wear mechanisms and frictional behaviour of thermally oxidized Ti-6Al-4V alloy in high vacuum is the aim of this work. The methodology consists of the following steps:

1. To conduct dry sliding tests in high vacuum. A pin (ball)-on-disk apparatus was designed and built in-house for this purpose. This devise could run under high vacuum of 7×10^{-6} torr.
2. Ti-6Al-6V surfaces underwent thermal oxidization process. The wear tests were carried out on the TO-treated and untreated Ti-alloy using two types of counterfaces made of 52100 steel, Ti-6Al-4V and TO-treated Ti-alloy.
3. Using scanning electron microscopy (SEM), energy dispersive system (EDS), X-ray diffraction (XRD), and analysing the coefficient of friction (COF) and wear rates, the effect of surface treatment on the wear resistance of Ti-6Al-4V alloy in high vacuum was determined.

1.1. Outline of the Thesis

This thesis begins with a broad description on dry sliding wear in ambient air and low atmospheric pressure. Then, an introduction was made to the titanium and Ti-6Al-4V alloy, their wear mechanisms and frictional performance of Ti-6Al-4V alloy. Thermally oxidized Ti-6Al-4V and its tribological properties in air and corrosive media were examined in Chapter.2. The objectives of current project are also given at the end of Chapter.2. Details of a new tribo-tester functioning under high vacuum are given in Chapre.3. Chapter.4 deals with the materials and experimental procedures. Chapter.5 describes the results obtained, and Chapter.6 gives a coherent discussion based on the results of current investigations and available information from literature survey. Finally, conclusions are presented in Chapter.7.

CHAPTER II

Literature Survey

2.1. Introduction

Adhesion, friction, and wear of materials generally are associated with the intrinsic properties of materials. Crystal structure, orientation, order-disorder reactions, ductile to brittle transitions, texturing and segregation of alloy for metals, chemical interaction between metals in contact with metals, and environment are among the factors that affect friction and wear of metals [19]. There is no doubt that results from wear and friction of metals under low pressure of oxygen are dissimilar to those in ambient air. The differences originate from reduction in number of oxygen molecules in atmospheric conditions of the tests. Under a vacuum of 10^{-9} torr and a load of more than 5N, pure metals with clean surfaces such as copper, nickel, titanium, and zirconium are characterized by very high coefficient of friction (COF) and wear in the form of adhesion [19]. In case of very clean surfaces, Bowden et al [20] observed a COF of 3 and even up to 20. Buckley [19] suggested that the area of metal-to-metal contact may be small and the required force for sliding two surfaces is generally equal to the shear strength of the surface film material. The friction force is determined by the shear strength of the metal junction and true area of contact in vacuum and with the clean surfaces [21]. The adhesion force between metals with clean conditions is attributed to the high elimination of oxygen.

In a clean condition, friction depends on mechanical properties such as strength and ductility of metals. The growth process of transfer particles (wear particles) can be suppressed in vacuum whereas it was enhanced by oxygen [19-23]. The existence of alloying elements in material affects strongly the adhesion force. However, in comparison with pure metals, fewer experiments have been reported on alloys (steels, titanium alloys, etc.) under the vacuum conditions. There are only a few reports on normalized AISI 1045 carbon steel (pin-on-ring in high vacuum), EN31 on SS41 mild still (ball-on-disk in medium and low vacuum), and titanium alloys (pin-on-disk in relatively high vacuum) [24, 25].

The literature survey presented in this chapter sets to address all significant aspects of the role of the presence and absence of oxygen during and after rubbing between the surfaces. The general idea of sliding wear and in particular oxidational wear, and its effectiveness on friction and wear of metals are described briefly in first two sections. Then, to highlight important mechanical and intrinsic properties of contact surfaces in absence of oxygen, the microstructure, strength and hardness of surface and sub-surfaces shall be discussed. Section 4 deals with the influence of vacuum on various properties of pure metals and alloys. Conducting experiments in low atmospheric pressure need some special equipment. Therefore, the fifth section emphasizes the experimental set-ups that have been used in the laboratories for this purpose. In last section, we focus on titanium alloys (Ti-6Al-4V), as one of the essential alloys in modern light weight alloy technology in aerospace application where vacuum tribological properties are important. At the end of this literature survey, the objectives of the M. A. S. c thesis will be stated.

2.2. Dry Sliding Wear

2.2.1 Modes of Wear

Material removal in the form of surface damage, fracture, and oxidation occurs if abrasive wear, rolling contact wear, fretting wear, erosion wear, or sliding wear take place [26]. Abrasive wear, rolling contact wear, and fretting wear occur during the contact between two solid bodies. In case of abrasive wear, the third solid body trapped between the two others may be responsible for the abrasion of surfaces [8, 26]. Erosive wear occurs in the presence of a flowing liquid. Damage caused on the sliding surfaces in air without a lubricant is called dry sliding wear. Hutchings [8] stated three main factors that control wear of sliding surfaces. These are mechanical stresses, temperature, and oxidation phenomena. They may be influenced by normal load and sliding velocity. Archard wear equation [8] is the most frequently referenced "law" of sliding wear:

$$Q = \frac{KW}{H} \qquad \textbf{(2-1)}$$

where Q is the volumetric wear rate. The main variables that influence sliding are W, the normal load and H, the indentation hardness of the softer surface. Severity of wear is described by means of the wear coefficient, K.

2.2.2 Mild and Severe Wear

Sliding wear can be divided into two types [8, 27]. These are: i) the mild wear, ii)the severe wear. The terms of mild wear and severe wear are used to describe conditions on the either side of transition. Mild wear usually is associated with low wear rate, smooth surface, a steady friction trace. Mild wear usually occurs at low loads and velocities. This process is isothermal [8]. This type of wear is characterized by the formation of finely divided wear particle (debris) as well. The size of debris is typically from 0.01 to 1 μm. Mechanical damage, which is accompanied by high load and velocity, and therefore high contact surface temperatures lead to severe wear. The wear debris caused by severe wear are metallic with typical size of 20 to 200 μm [8, 28]. A practical way to distinguish between the mild wear and the severe wear is to observe the change in magnitude of the wear rates with load, sliding velocity, and/or sliding distance. In sliding between α/β brass pin and a hard stellite ring, at low loads, the wear rates were formed to increase with the normal load. In a load range of 5 to 10 N, a sharp increase in wear rate occurred. The roughness of the worn brass surface also changed from 0.5 μm to about 25 μm above the transition. Mild wear is the regime of wear at low loads, below the transition while term of severe wear refers to the wear rate above transition [29]. A third transition was observed while the normal load exceeded 10 N. Archard's equation was valid in all ranges of wear, thus, there were three distinct coefficients of wear. **Fig 2.1** illustrates the wear rate for this pin-on-ring system.

2.2.3 Sliding Wear Mechanisms

In sliding wear, delamination, and oxidative wear mechanisms cause damage to the surfaces. Lim and Ashby [28] considered four broad classes of mechanism in sliding wear: (1) seizure, (2) melt wear, (3) oxidational-dominated wear, and (4) plasticity-dominated wear. Plasticity-dominated wear is caused by adhesion and/or delamination

[28]. Seizure occurs mostly because of plastic indentation, large-scale mass flow, and metallic transfer following a period of severe wear or immediately upon contact under high load [28]. The temperature increase caused by high relative velocity between the sliding surfaces may reach to the melting point of one or both sliding surfaces. If melting of surfaces occurs, it causes a decrease in the coefficient of friction and an increase in wear rate as the strength of metal drops rapidly [8, 28].

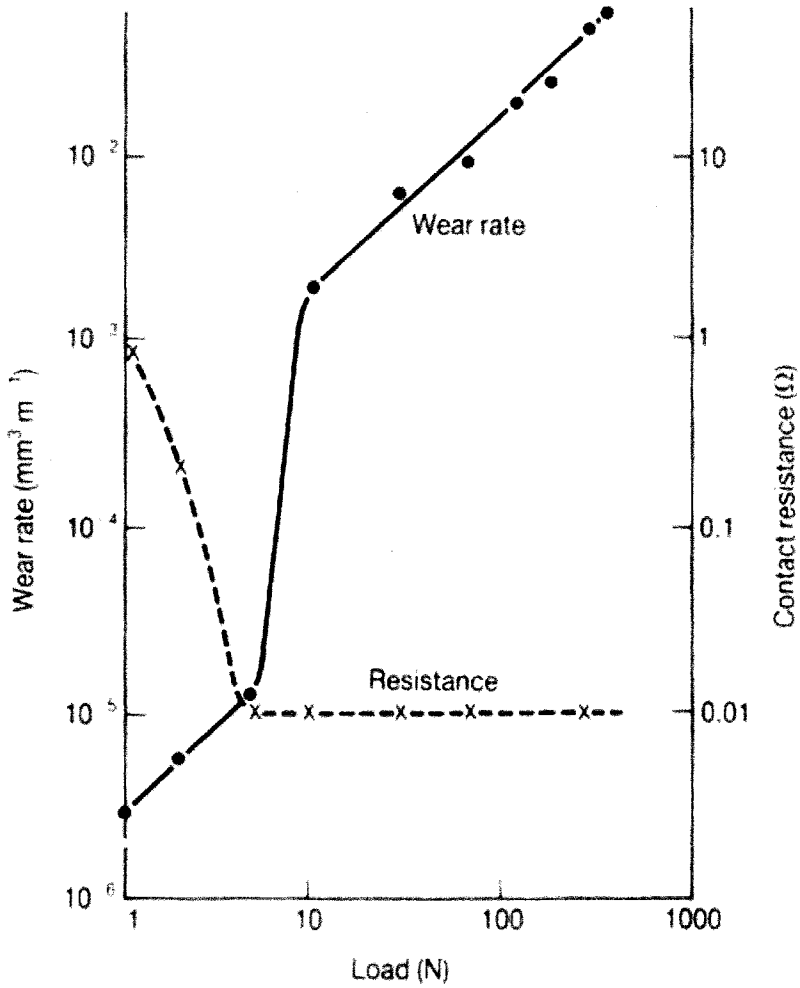

Figure 2.1 The wear rates of α/β brass versus applied load [29].

Wear in sliding between surfaces can also be caused by oxidational wear mechanism as well as by mechanical wear. In sliding of a AISI M2 Steel (pin) on low carbon steel coatings deposited on 319 Al alloy substrates (disk) in day air, severe wear was observed because of mechanical wear and the oxidational wear. At low velocity (less than 1 m /s) and high load (less than 20 N) the mechanical wear was the main cause for severe wear. The XRD of wear debris showed presence of higher percentage of ferrite in comparison with the percentage of Fe_2O_3, Fe_3O_4 and FeO. The SEM [26] has confirmed fracture and fragmentation of steel splats at contact surfaces. In case of an actual engine test severe wear showed up as scuffing on the surfaces coated with HVOF 1020-2.5%Al type of low carbon steel thermal spray coating [30]. Under the laboratory testing conditions, at high sliding velocity and high loads, severe oxidational wear was observed. The XRD showed higher amounts of Fe_2O_3, Fe_3O_4 and FeO, and lower amounts of Fe compared to the tests at low velocity. Severe deformation of steel splats still was observed but thick oxide rich layers covered nearly 70% of contact surfaces [31]. In summary, the both types of wear mechanisms may occur in severe and mild wear.

2.2.4 Delamination Theory

This theory is based on the sub-surface crack and void formation. Subsequently cracks join by shear deformation and reach the surface [32]. The sub-surface layer adjacent to the worn surface may accommodate large plastic deformation without fracture [32]. The four mechanisms, which cause the ultimate failure of the surface due to the wear, are [33]: ***i***) Plastic deformation of the surface layer. ***ii***) Subsurface void and crack formation due to the plastic deformation. ***iii***) Subsequent crack propagation and void growth, which eventually link up with neighbouring cracks and void to form long subsurface cracks along a direction nearly parallel to the surface. ***iv***) Formation of loose wear sheet when the subsurface cracks shear to the surface. Under dry sliding wear conditions using a block-on-ring type wear machine, Zhang et al. [34] showed that thin flake-shaped debris of A356 aluminium-silicon were generated by the same mechanism. In their investigation near the surface, void and micro-crack nucleation, and subsurface crack growth were detected by SEM. **Fig 2.2** illustrates the subsurface crack propagation in A356 alloy.

2.2.5 Work Hardening of Worn Surfaces in Dry Sliding Wear:

Work hardening of surface layers of metals takes place under friction during the sliding between metallic surfaces. The structure of the surface layers is changed by the friction process, therefore by increasing the dislocation density, layers become hardened [35]. By means of the Hall-Petch equation, Garbar [35] established a correlation between the work hardening and the types of wear in metals. He found that the same relations could be used for the fragmented structures [35-36]. The term "fragmented structure" includes all the microstructures formed under large plastic deformation such as sub-grains and cells. According to the Hall-Petch equation, σ_s which is the flow stress (yield stress) of metals is increased as d_c, the size of cell (or grain size) decreased.

$$\sigma_s = \sigma_0 + kd_c^{-n} \qquad \textbf{(2-2)}$$

where σ_0 is the internal friction stress during dislocation motion, k is the "locking parameter," which measures the relative hardening contribution of the grain boundaries [37]. Garbar [35-36] proposed that if the wall of fragments become 'opaque' to dislocations and restrict dislocation transfer, the fragment size can determine the level of work hardening, and can be used instead of grain size in the classical Hall-Petch relation. Work hardening will be maximum if the size of fragments reaches the minimum while the mutual misorientation between the neighbouring fragments is maximum. The copper (99.95 %) and low carbon steel (0.08 % C), which were tested with a reciprocating friction machine, showed good correlation with the Hall-Petch theory. Electron diffraction pattern showed that the relative intensities of lines, (110) for α-Fe, and (111) for Cu, changed significantly with a change in load [36]. Increasing in load during friction helps to clarify more lines particularly for copper sample in X-ray diffraction system [36]. As the load increased, the wear rates of copper and steel are increased. The increase in the wear rate and frictional force indicate a reduction in average dimension of fragments in low carbon steel from 0.6 to 0.2 μm and in copper from 0.09 to 0.05 μm. As expected, changing the size (fragmentation) leads to hardening of metals because of the barrier effect of the fragment walls. The value of disorientation between neighbouring in these cases may be as high as several degrees. Thus, the boundaries of the fragments

present about the same major obstacle for dislocation movement as the grain boundaries [36].

As illustrated in **Fig 2.3**, for both low carbon steel and copper, within the range of mild wear, the size of the surface layer fragments decreases as the wear rate increases. Therefore, according Hall-Petch equation if d is minimized, the flow stress is maximized. In another words, the plastic deformation rate ($\dot{\varepsilon}_d = \dot{\rho} b V(\sigma_e)$) will be greater than the rate of relaxation processes ($\dot{\varepsilon}_r = \dot{\rho}(\sigma_i) b \lambda$), and that is because the free path length for dislocations, λ, decreases and dislocation speed and external stress increase indeed [35]. Here, b is Burger vector, V is the dislocation velocity, $\dot{\rho}$ is the rate of new dislocation generation (ρ is total length of dislocation per unit volume), σ_e and σ_i is external and internal stress respectively.

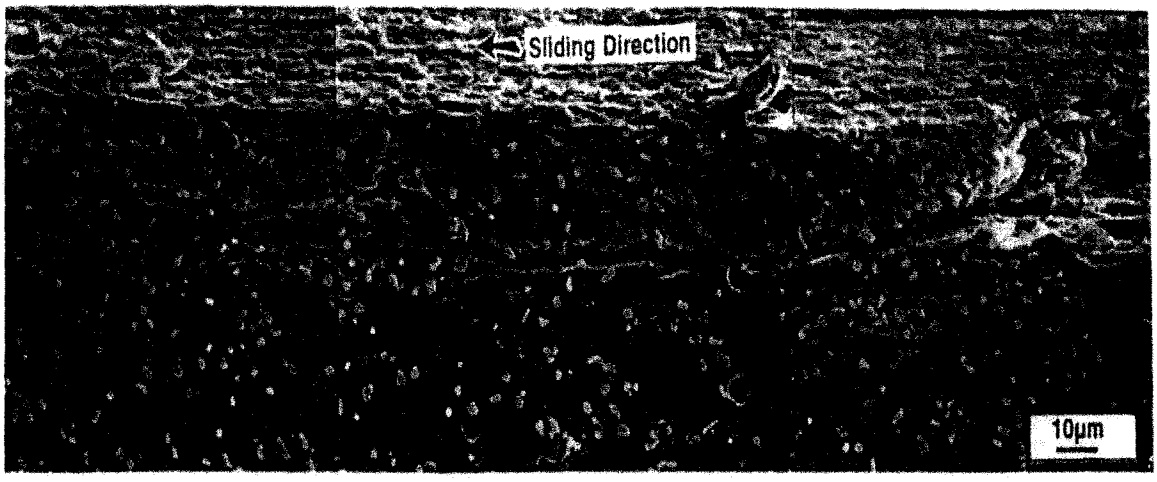

Figure 2.2 Subsurface crack propagation in A356 alloy [34].

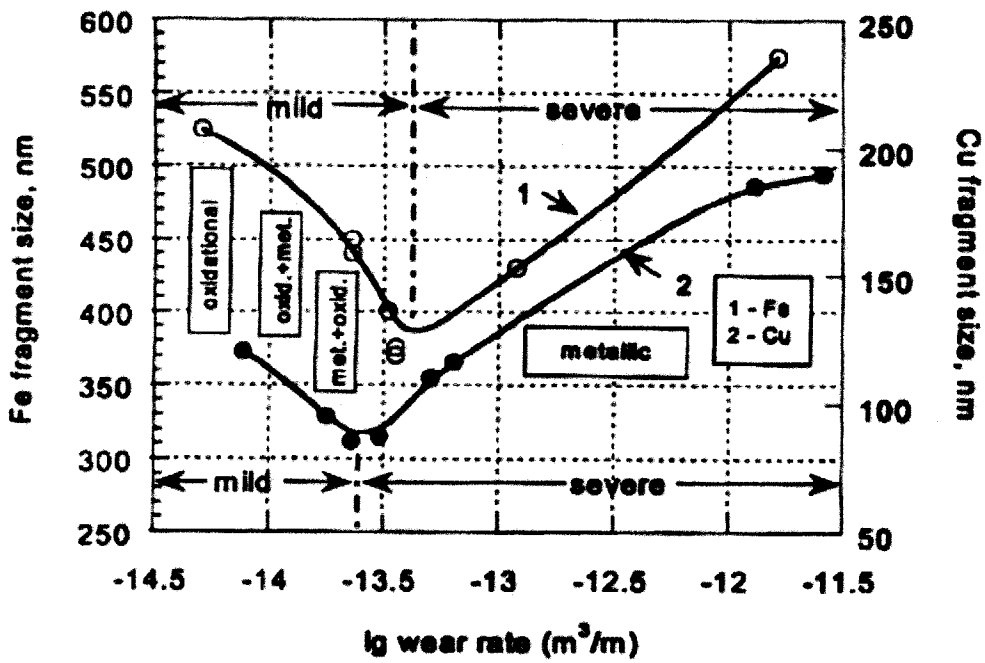

Figure 2.3 Significant change in size of Fe fragment (nm) and Cu fragment (nm) demonstrated during the transition from mild to severe wear. The graph obeys the Hall-Petch until fragments reach the critical minimum size and rate of plastic deformation is larger than rate of relaxation process [1].

Harsher friction and the lack of an effective metal strengthening mechanism lead to an increase of wear in this region. It should be pointed out that wear particles formed during sliding in mild region are oxidized (mostly Fe_2O_3) while those had been found in severe region are mostly metallic. Under low pressure the most intensive lines of electron diffraction pattern are belong to the oxides, and therefore, the oxidational wear mechanism is prominent during the mild wear [1].

2.2.6 Formation of Wear Particles in Dry Sliding Wear

The morphology of debris particles depends upon the applied load, sliding velocity and the environment [38-39]. Sasada et al [38]. proposed two models for formation of wear particles. When the frictional motion shears a metal-metal junction formed between the intimate surfaces, a small fragment of either surface portion will be sheared off and adhered onto the mating surface. This transfer element creates a new asperity on the opposite surface and may form a new junction in the course of further sliding. With accumulation of at least two transfer elements a transfer particle is formed. Through the repetition for accumulation of these articles, the debris size gradually grows and it is suddenly removed from the surface by a mechanical impulse from the opposite surface (producing wear particle) (**Fig 2.4**). If the material properties do not change during sliding, particles between mating surfaces must be depressed until the contact pressure becomes equal to the flow pressure of the material to support the total load. The particle is not only depressed normally by the contact load but also extended longitudinally by the shearing action. The flattened shape of the transfer particle becomes adhered to both surfaces. Accumulation and piling up of these "press-slide-flattened" particles are followed by their removal from the tribo-system in the form of plate like loose part. (**Fig 2.4**) [10, 38].

2.2.7 Microstructure of Sub-Surface Layers in Dry Sliding

Moore et al. [41] examined the relationship between the microstructure and strength of worn metal surfaces. The surface strain can be very high as material continues to work-harden [41]. The degree of work hardening is due to the increased density of the dislocations in material during plastic deformation, obstacles, such as grain and twin

boundaries, precipitates prior to deformation. The flow stress of surface and subsurface is proportional to one-third of hardness of surface [44]. Based on earlier discussion (section 2.2.5), it is clear that the hardness of sliding surfaces is much higher than the initial hardness of the material. There is no deformation in grains of the metals beyond certain depth under the worn surface, usually below 50-100 μm [44, 42]. However, near the surface of pure metals Hiratsuka [42] categorized the types of hardness in three groups: ***i***) The pin subsurface, ***ii***) The transfer particle and/or wear debris, and ***iii***) The disk subsurface. When these three groups have the same hardness, there will be no transfer between the sliding surfaces. This happens when the tribo-system is under steady state wear. Therefore, particle transfer and wear debris formation are directly related to the hardness tribo-system. Impurities like oxygen and other species generated by the chemisorption's activities of metals can affect the hardness of surface and subsurface down to very thin depth (few nm) [42-43].

By investigating the worn surface morphology generated during dry sliding test of a block (copper)-on-ring (AISI 440C), Heilmann et al. [44] divided the plastically deformed material for the copper surface into three layers. The farthest layer away from the interface covers about 80% of the total deformed region. A pure rotation of lattice occurs about an axis normal to the sliding direction and parallel to the wear interface. Approaching

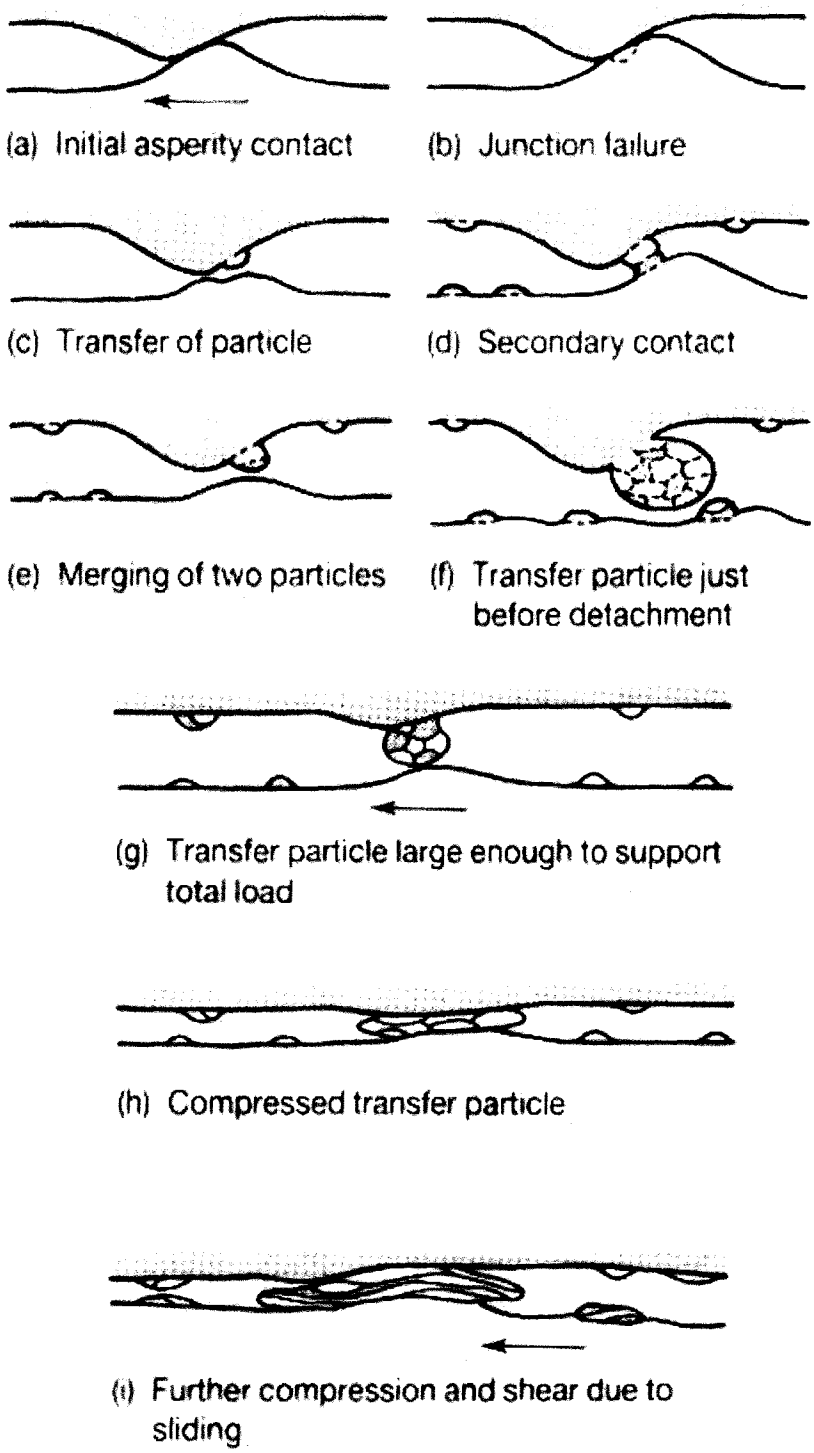

Figure 2.4 The wear particle may be equiaxed (***a to f***) or under additional plastic deformation be flattened (***g to i***). It is based on Sadata hypothesis [38].

to surface leads to increasing exponentially in the magnitude of this rotation. In the more highly strained region, the dislocations form wide cell walls with regions of lower dislocation density [45]. As the misorientation angles across the boundaries grow, walls parallel to the sliding direction are generated more frequently, thus limiting the increasing misfit across a single cell wall. Therefore, the flattened cells can be observed where the strains are highest [45]. The second region, which recorded a rotation is around 5 to 10°, is similar to the first region. The exception is the presence of narrow bands of cells separated by higher angle boundaries. These bands arise from different parent grains, which have been sheared such large amounts of the surface. They tend to overlay each other as indicated in **Fig 2.5.** The third layer is called the transfer layer and consists of ultra-fine crystalline particles [45].

Both linear and nonlinear hardening may take place near the worn surface. The Voce constitutive equation and its modified form have been used to explain the work hardening the subsurfaces [34, 46]. According to the Voce equation:

$$\sigma_f = \sigma_s - (\sigma_s - \sigma_o)\exp\left(-\frac{\varepsilon}{\varepsilon_c}\right) \qquad \textbf{(2-3)}$$

where σ_f is the flow stress at strain ε, σ_0 is the bulk flow strength, σ_s is the saturation stress (the stress at which the work hardening rate becomes zero), and ε_c is a constant. Zhang et al. [44] applied this equation for block (356 Al)-on-ring (steel) to obtain the result of the work hardening rate against flow stress. The results show the close correlation between experimental data and modeling (**Fig 2.6**).

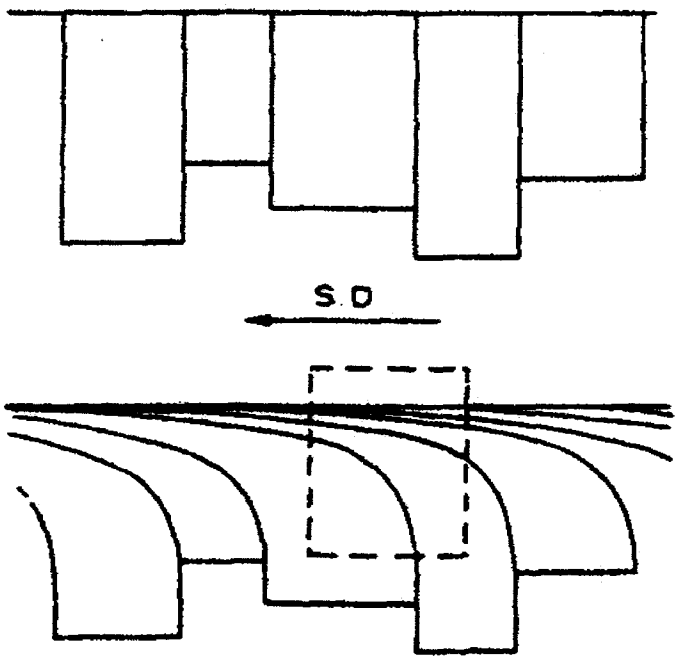

Figure 2.5 Simple model to indicate how sliding can create surface layers of material derived from different grains [45].

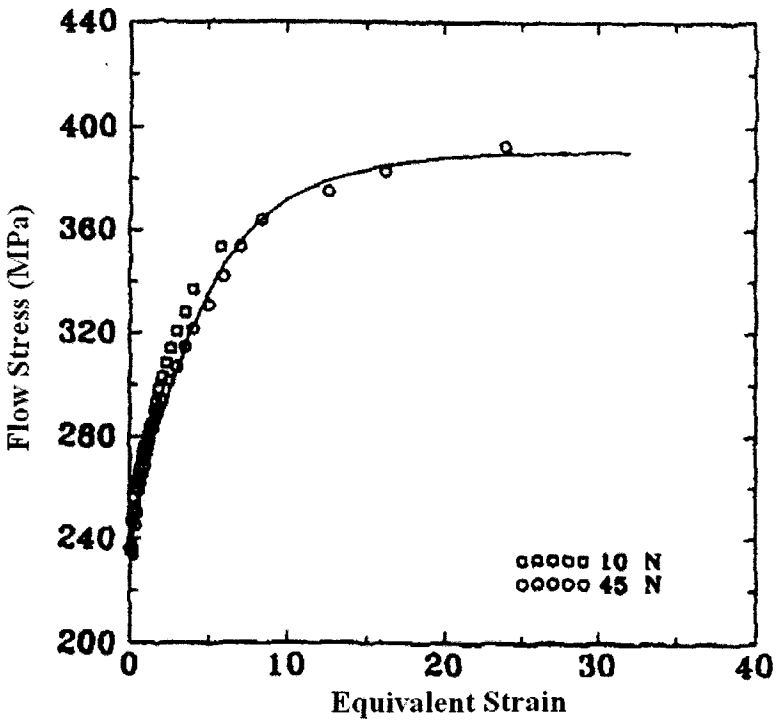

Figure 2.6 Cumulative flow stress versus plastic strain curve for 356 Al below the contact surfaces. The solid line represents the Voce function computed from the experimental data [44].

2.3. Oxidational Wear Mechanism

Presence of 20% of oxygen at 1 atm of air pressure, in ambient air provides a suitable condition for metallic surfaces react with oxygen. This accompany the tendency of valance electrons to stay in lower level of energy in metals create oxides [47]. Thus, it is expected to see a very thin layer of metal oxide on their surfaces. Oxidation becomes more predominant during the friction because of high contact temperatures. Spalling off a thin film of oxide between the rubbing surfaces leads to debris formation. At high speed unidirectional sliding, where frictional heat can lead to surface temperatures that are sufficiently high, relatively thick oxides are formed on the contact surfaces [2]. This oxide layer may prevent severe wear in such a way that the tribo-system does not approach to seizure [2, 8, 28]. Yet, it does not mean that it necessary decreases the wear of the metals [48]. Oxygen solubility and diffusivity in material (alloy), growth rates of the various oxides, surfaces condition, microstructure and mechanical properties (oxygen pressure and temperature) are among the effective factors that favour formation of oxide layers [2, 48].

In this section, surface temperature will be introduced as a main factor of surface oxidation (2.3.1). Then, a quick review of the concept of mild and severe oxidative wear surface will be explained in 2.3.2. Notice that the notations of mild and severe refer to the extent of oxidation at the sliding surfaces; there are not a reflection of the rates of wear. Tribology of oxide layers will be explained. Finally, mild and severe oxidative wear that result mild and severe wear will be discussed.

2.3.1 Initiation and Growth of Oxide layer

The oxidative wear theory [3, 8] states the temperature at the tip of the asperities, which is higher than average temperature of the surface, has a significant effect for building the oxide layer. The average temperature of the contact surface is called the bulk temperature. Oxide layer forms as soon as frictional heating at the contacting asperities takes place [8, 28, 49].Variation and magnitude of "hot spots" are directly associated with the application of normal load, velocity, and combination of them [1, 3, 7, 9, 27, 28, 49]. The details of bulk and flash temperatures are presented in appendix.A.

The surface-temperature maps for different combination of sliding materials such as bronze on low-carbon steel, low carbon steel on itself, and magnesium oxide on steel indicate that in high load, bulk and flash temperature show the same result. On the other hand, there is a drastic deviation between bulk and flash temperature in low load and velocity [7, 28]. This is illustrated in **Fig 2.7**. As surfaces begin to oxide, the impact of oxidational wear comes to attention. A relationship exists between the temperature of real contact area (flash temperature, T_f), the size of individual contact area, and thickness of oxide layer [3, 6, 9, 50]. Parabolic, logarithmic, or linear growth of oxide films has been reported during sliding [3, 8]. The Arrhenius equation is used to determine the oxide wear rates W [3, 28]: (**see Fig 2.8**)

$$W = \frac{A_P \exp\left(\frac{-Q_o}{RT_C}\right)}{\rho^2 Z_c^{\,2} f_o^2 V} A \qquad \textbf{(2-4)}$$

where Q_o is activation energy for oxidation, R is molar gas constant, A_p is the Arrhenius constant. V is the velocity, Z_C is the critical oxide film thickness, ρ is density of oxide, f_o is fraction of oxygen in the oxide film, and A is real area of contact. For oxidation of steels in sliding contacts and at temperature lower than 450 °C the magnitude of this constant is 10^{16} $kg^2m^{-2}s^{-1}$ while at the temperature higher than 600 °C its value reduced to 10^8 $kg^2m^{-2}s^{-1}$. In comparison to the Arrhenius constant, in static oxidation, these values are much higher. It indicates that oxidation under sliding condition is much more rapid than static oxidation.

Lim and Ashby [28] explained that there are many variables involved in equation (2.4). However, they showed that the data plot of this model suggested that data from different sources, using specimens of various shapes and sizes could be best correlated by using a normalized wear rate, $\tilde{W}$ force and sliding velocity, defined by [28]:

$$\tilde{W} = \frac{W}{A_n}, \tilde{F} = \frac{F}{A_n H_o}, \tilde{v} = \frac{v r_o}{a} \qquad \textbf{(2-5)}$$

Where A_n, is the nominal (apparent) contact area of sliding surface, H_o is its room temperature hardness, a is the thermal diffusivity and r_o is the radius of the circular nominal contact area [26]. Therefore, following equation may be applied as well:

$$\tilde{W} = \left(\frac{C^2 A_p r_o}{Z_c a} \right) \exp\left[-\frac{Q_o}{RT_c} \right] \frac{\tilde{F}}{\tilde{v}} \qquad \textbf{(2-6)}$$

where in Normalized wear rate equation, C is constant used in the model for mild oxidational wear, Q_o is the activation energy for oxidation, R is the molar gas constant, a is the thermal conductivity of metal, T_C is temperature of real contact area, r_o is radius of pin, $\tilde{F}$ and $\tilde{v}$ are designated for normalized force and velocity.

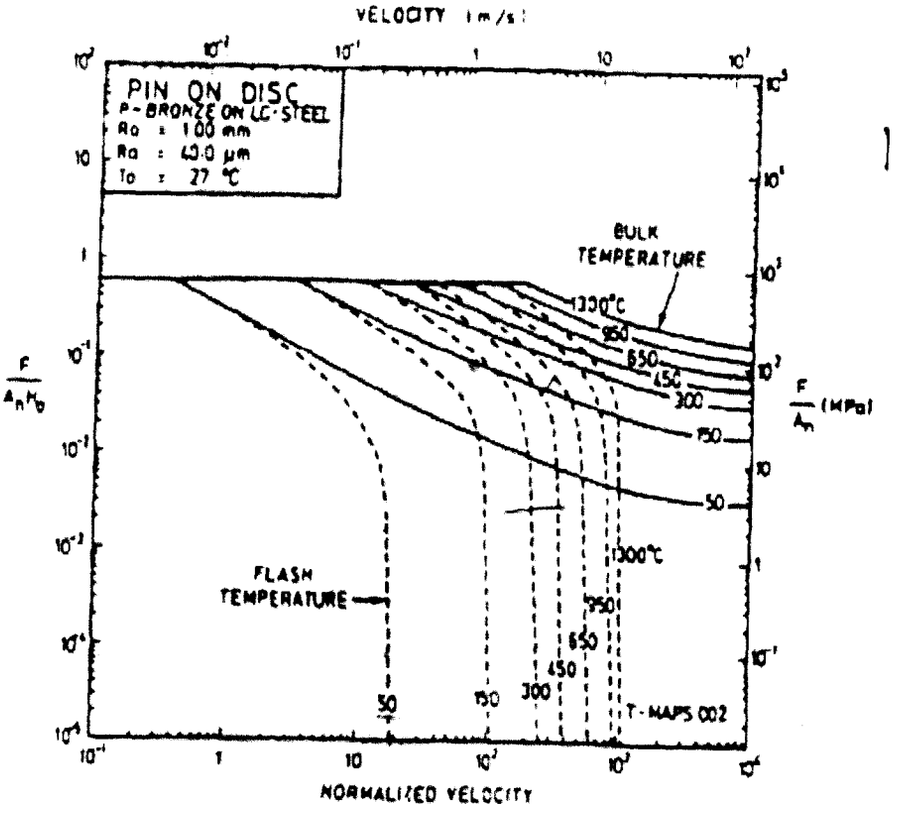

Figure 2.7 A temperature map for phosphor bronze sliding on low-carbon steel [7].

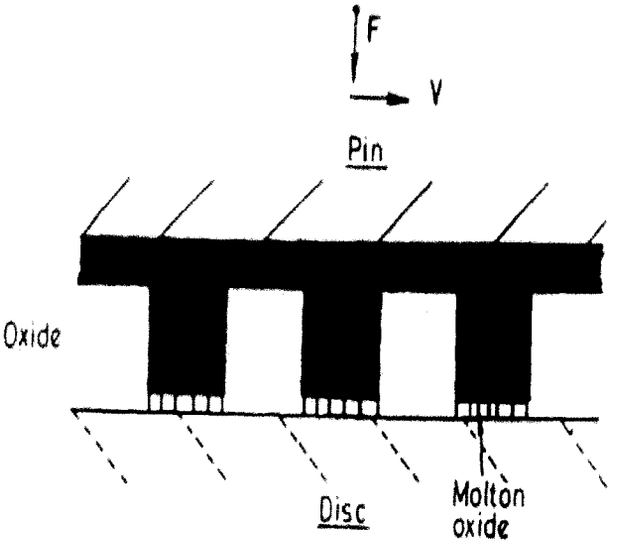

Figure 2.8 Schematic representation of idealized severe-oxidational wear model [28].

2.3.2 Characterization of Oxide Surface:

Two surface oxidations have been introduced in dry sliding surfaces [3, 8, 26]:

1. Mild surface oxidation
2. Severe surface oxidation

The distinction between these two surface oxidations lies in the sliding velocity, normal load, area of covered surfaces, thickness, and strength of the layers. In a pin-on-disk system, mild type of surface oxidation is encountered while the sliding speed exceeds 1m/s with a light load, or in case of lower speed with higher loads [28]. The mild surface oxidation characterized by thin, brittle and patchy oxide film. In contrast, High sliding speed (more than 10 m/s for steel), thick oxide film, and surface totally covered by oxide film represent severe surface oxidation [28]. Heavily frictional heating at the tips of asperity causes oxide surface. At this moment, completely oxidized and thin layers of molten oxide are formed at the asperity contacts (**Fig 2.8**) [28]. **Fig 2.9a** and **2.9b** show that a thin oxide film forms at the asperity contacts. Then, the thickness of film reaches to critical magnitude. Up to this level, thin film plays as a protective layer between metallic surfaces [28].

2.3.3 Tribological Functions of Oxide Layer:

The oxide layer that formed during sliding surfaces has at least two useful tribological functions: ***i***) Oxide films prevent the metallic contact between sliding surfaces. ***ii***) Oxide films serve as a supplementary and effective lubricant [1, 11]. Hirst and Lancaster [11] explained this property in a tribo-system contains copper in form of pin-on-flat surfaces. The coefficient of friction at the onset of sliding is determined around 0.5. Due to the extensive welding and tearing of two sliding surfaces, this value increased to 1.2. Low coefficient of friction is attributed to sliding of the copper oxide on each other. This phenomenon has been seen in the other metals such as nickel, and cadmium, and lead [11]. If hardness of oxide layer is very low, the layer is not strong enough to protect the sliding surfaces, and it breaks out from the surfaces [51]. Thus, the contact occurs between metallic surfaces. If lubrication of the oxide film dominated the wear rate, the wear rate should have been lower at high temperatures because of higher oxidation rate [52].

In low load and velocity, two more trends may lead to oxidational wear mechanism rather than temperature on the surfaces or at the tip of asperities. Sometimes the surfaces are already totally or partially oxidized, and during the sliding not all the oxide removed. As sliding continues, the layer gets thicken with time. This can give protection against further wear, as severe oxidational surface [2]. The other trend is the oxidation of metallic debris. If metallic debris is broken up and reduced in size by sliding action, thereby exposing fresh area of clean metal for further oxidation, the debris will be oxidized. During sliding, the oxidational wear process is promoted by the heat of deformation and the increased energy of the particles due to the increased defect density and surface energy. In addition to these factors, if the heat of oxidation released is taken into account, fine metallic particles may be oxidized spontaneously and completely under some conditions. The resulting oxide debris can develop into a wear-protective layer [2].

2.3.4 Mild and Severe Oxidational Wear:

Mild oxidational wear occurs when the sliding speed exceeds 0.5 m/s in steel. At this velocity, frictional heating at the contacting asperities become considerably (as it mentioned section 2.3.1) leading to higher rate of oxidation. This oxidational surface, yet, can be brittle and thick. The effective separation of the sliding surfaces by the oxide layer results in mild wear [49]. If load becomes higher, the asperities may penetrate to the brittle oxide layers generated by increased frictional heat. Then direct metal-to-metal contacts will happen [49]. In **Fig 2.9c**, the broken oxide layer turns into wear debris, and this causes mild wear which is in form of mild oxidational wear. With the small range of sliding condition, severe wear occurs and this leaves behind a damaged sliding surface. With further increases in load and speed, a hard surfaces layer can formed because of the higher flash temperature, followed by rapid quenching as the heat is conducted quickly into the underlying bulk material [49]. High temperature means higher oxidational rate, therefore, a thicker and more distributed layer of oxide may be formed. This layer is on the already harder substrate, and able to prevent further direct metallic contacts. Consequently Mild wear occurs and significant reduction in wear rate is the result [8, 28, 48]. Hiratsuka [53] (2005) pointed out that easy oxidation of small particles does not

cause mild wear if those particle are removed from the wear track and do not remain attached to the surfaces.

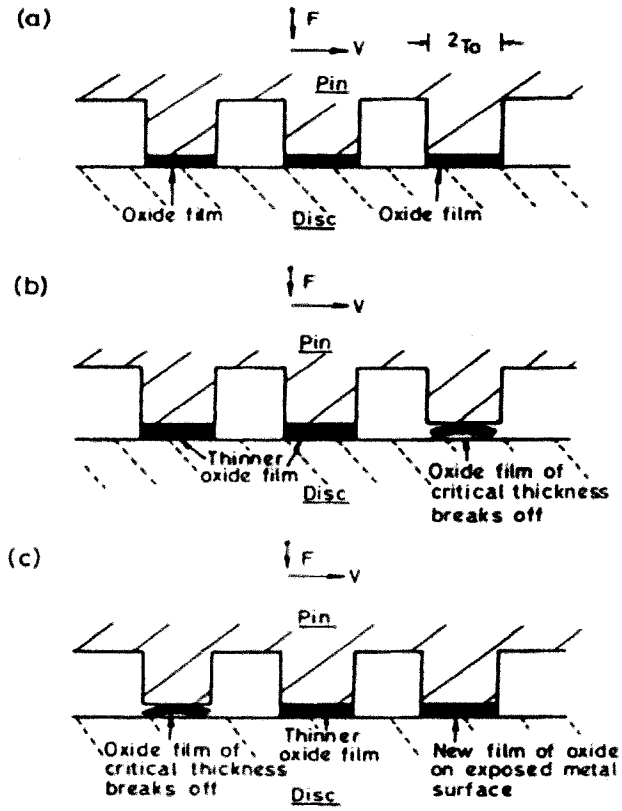

Figure 2.9 Schematic representation of idealized mild-oxidational wear model [28].

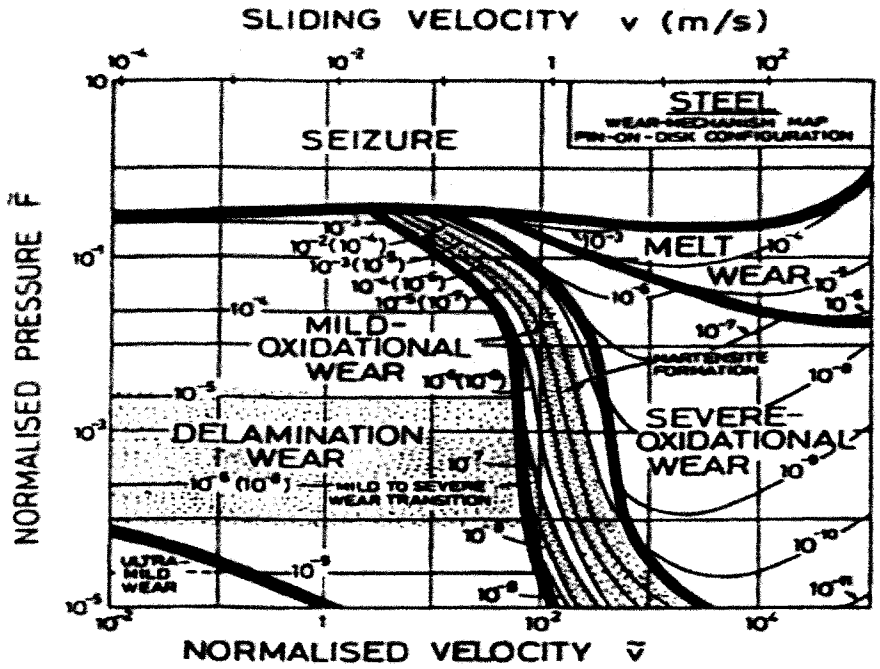

Figure 2.10 The wear-mechanism map for a steel [28].

At a certain threshold of velocity, the amount of oxide formed on the surfaces has been found to increase from the isolated patches on the sliding surfaces to plastically deformed continuous film of oxide covering the entire sliding surface [28, 49]. In comparison to the more brittle nature of the colder and thinner oxide, this layer of oxide is thicker, hotter and more plastic [49]. At this situation, wear rate can be higher or lower. If this layer melts because of high temperature, severe wear occurs [28, 49].

The empirical wear-mechanism map for steel can demonstrate a range of normalized velocity and normalized pressure (normal load) accompanied with sliding velocity. There are certain regions that mild-oxidational wear can occur, so can the severe-oxidational wear [28]. **Fig 2.10** shows the region in wear-mechanism map occupied by oxidational wear. The electron diffraction patterns, EDS, and XRD of the relatively fine fractured material (debris) and smooth surfaces during mild wear indicates oxidized elements in mild wear regime [8, 36, 53]. Wilson [54] constructed a load versus velocity map for dry sliding wear of PVD TiN-coated high speed steel (HSS) disks against (HSS) pin over a range of contact loads and speeds. EDS analysis of transferred wear debris shows large amount of Ti and Fe are oxidized in region I, II, and less in region III. As it illustrated in **Fig 2.11**, in region II, mild wear of TiN is accompanied with oxidised HSS transfer. At very low load and velocity, oxidational wear is predominant (region I).

2.4. Tribotesters to Study of Wear in Vacuum

The use of vacuum system assists in the isolation of environmental effects [55]. To do so, research groups have to design and assemble particular test equipments and instruments to undertake research under the low atmospheric pressure. In this section, some of the tribo-testers used for vacuum tests shall be introduced.

2.4.1 Different Types of Tribo-testers

Friction and wear tests were carried out using a pin-on-disk [21, 55-59], disk-on-disk [56] ball-on-disk [56, 60, 61] configuration. These test rigs are mounted inside a vacuum chamber. Strain gauge assembly or load cells are used to determine frictional

forces. A normal load generally is applied by dead weight system or lever loading system [21, 57]. Then, dry nitrogen or inert gases are purged and pumped out of the chamber. In case of polycrystalline specimen of cobalt, beryllium, copper, etc..., the sample is heated up before mounting in chamber in order to remove residual stresses [21, 43]. To become familier to tribo-testers under vacuum (TUV) condition, the following are introduced:

Buckley [19] developed a relatively sophisticated system for his vacuum tests. A flat disk mounted in a vacuum chamber. It was driven through a magnetic drive coupling. The drive magnet placed outside the vacuum system was coupled to a hydraulic motor for low speed experiments. The second magnet was mounted on one end of the shaft within the chamber (**Fig 2.12**). The rider specimen was supported in the specimen chamber by an arm that was mounted by gimbals and bellows to the chamber. A linkage at the end of the retaining arm, away from the rider specimen, was connected to a strain-gauge assembly that was used to measure frictional force load applied by dead-weight loading system. An ionized pump (500 l/sec) and a sorption pump evacuated the chamber, and a cold cathode ionization gauge measured the pressure. The range of vacuum pressure was maintained between 10^{-6} to 10^{-8} Pa. In this configuration, an electron gun to heat up the pure metallic samples. The tests conducted on polycrystalline or single crystal specimens, and influence of crystalline orientation, and planar spacing might be examined. Thus sufficient energy could be obtained with the electron bombardment to evaporate the surface of the metals [19]

Kong, et al. [25] used a different system. A vacuum chamber made of stainless steel was used. A mechanical pump and a diffusion pump connected to each other evacuated the chamber. A thermal conductivity vacuum gauge and a penning gauge (down to 10^{-4} Pa) measured the pressure in side the chamber. A ball-on-disk rig was fixed inside the chamber. An AC servo-motor connected to a magnetic coupling drove the disk. Normal load was applied to the ball, and for linear motion of the loading device under vacuum, a linear bearing and a stainless bellows assembly were incorporated. Ambient temperature in the chamber was monitored by a thermocouple. A strain gauge

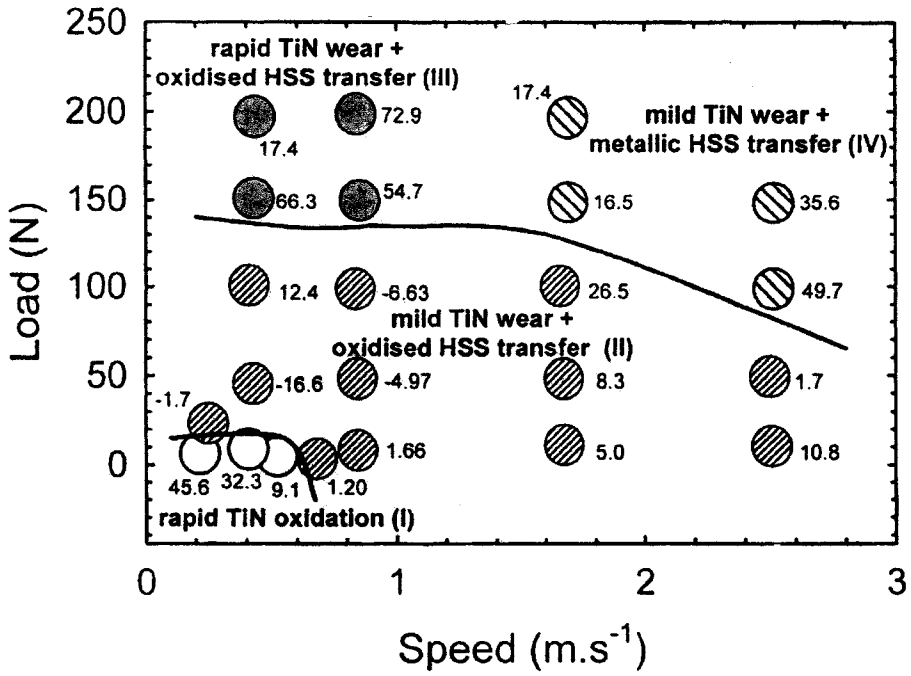

Figure 2.11 Wear map of TiN wear against HSS [54]

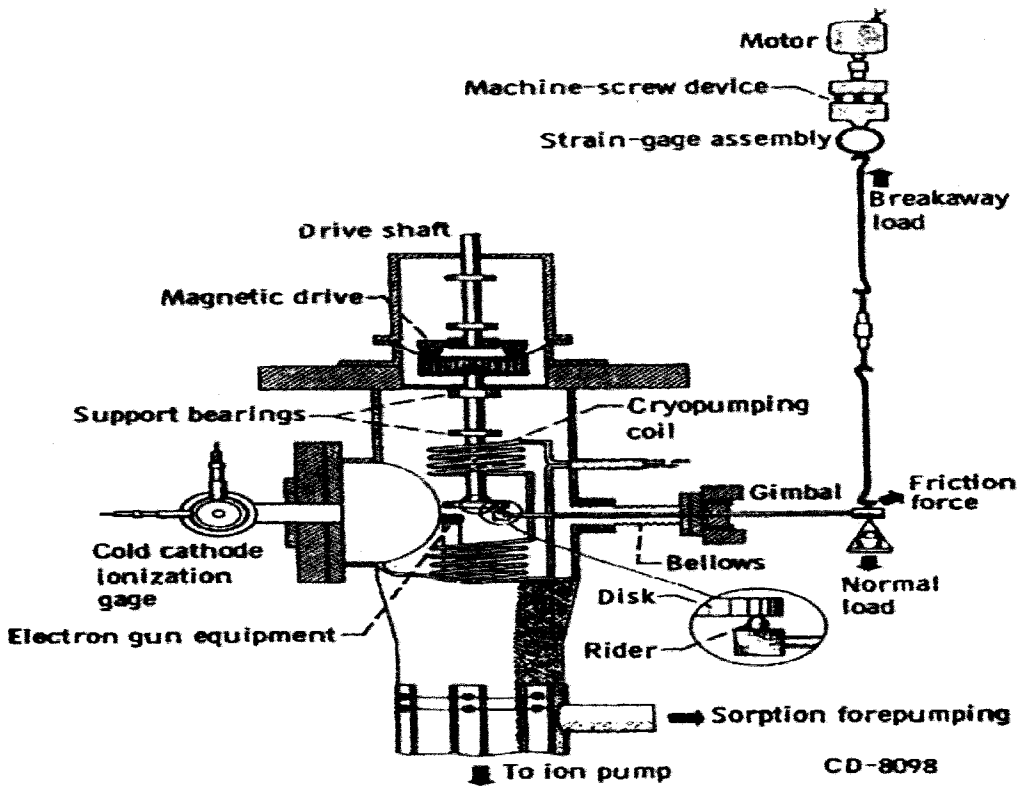

Figure 2.12 Vacuum friction apparatus used by Buckley [19].

load cell recorded the friction force between the ball and disk specimens. **Fig 2.13** demonstrates a sectional view of the wear rig.

Another wear rig, which was designed to work under vacuum was constructed by Cong, et al. [60]. **Fig 2.14** is the schematic diagram of their experimental apparatus. A ball-on-disk tribo-tester was installed into a chamber, which was connected to an X-ray photoelectron spectroscopy (XPS) analysis chamber. Gas could be introduced into the vacuum chamber through a variable leak valve. The Applied load and frictional force were measured with two couples of strain gauges. The ball was fixed and the disk was rotated.

To study the friction behaviour of materials in vacuum under low temperature (down to -196 °C) Udovenko et al [56] designed a testing machine UTI with a low temperature vacuum tribo-tester. This machine enabled one to perform tribological studied at low pressure (10^{-5} Pa) and low temperature (down to 77K). The test rig consisted of a low temperature vacuum tribo-tester located inside a high-vacuum chamber, an exterior electric drive with a multi-step reduction gear and the measuring equipment. The vacuum chamber was a cylindrical vessel with a nitrogen screen and a high vacuum cryogenic condensation pump. The nitrogen screen formed a kind of cooled inner casing of the chamber protecting the condensation pump and the working volume from heat flows coming from external walls [56]. Pre-evacuation was released by means of a backing and a diffusion pump with the nitrogen trap and anti-migration device. The friction pair pin/ball-on-disk (or disk-on-disk) was placed inside the condensation pump that prevented it from over condensation of various gases and oil decomposition produced from the warm walls on to the samples cooled to nitrogen temperature. The lower part was a vertical drive shaft with vacuum seals driven by a belt transmission from electric derive unit. The upper part of this tribo-tester was a vacuum-tight manipulator (plunger), which was mounted at the upper cap of the chamber (**Fig 2.15**), serves for transmission the normal load to the friction pair, fixing and driving the sample and measuring the moment of friction by the method of "involvement". The maximum

normal load and maximum sliding velocity for UTI-TV-100 were 100 N and 5 m/s, respectively.

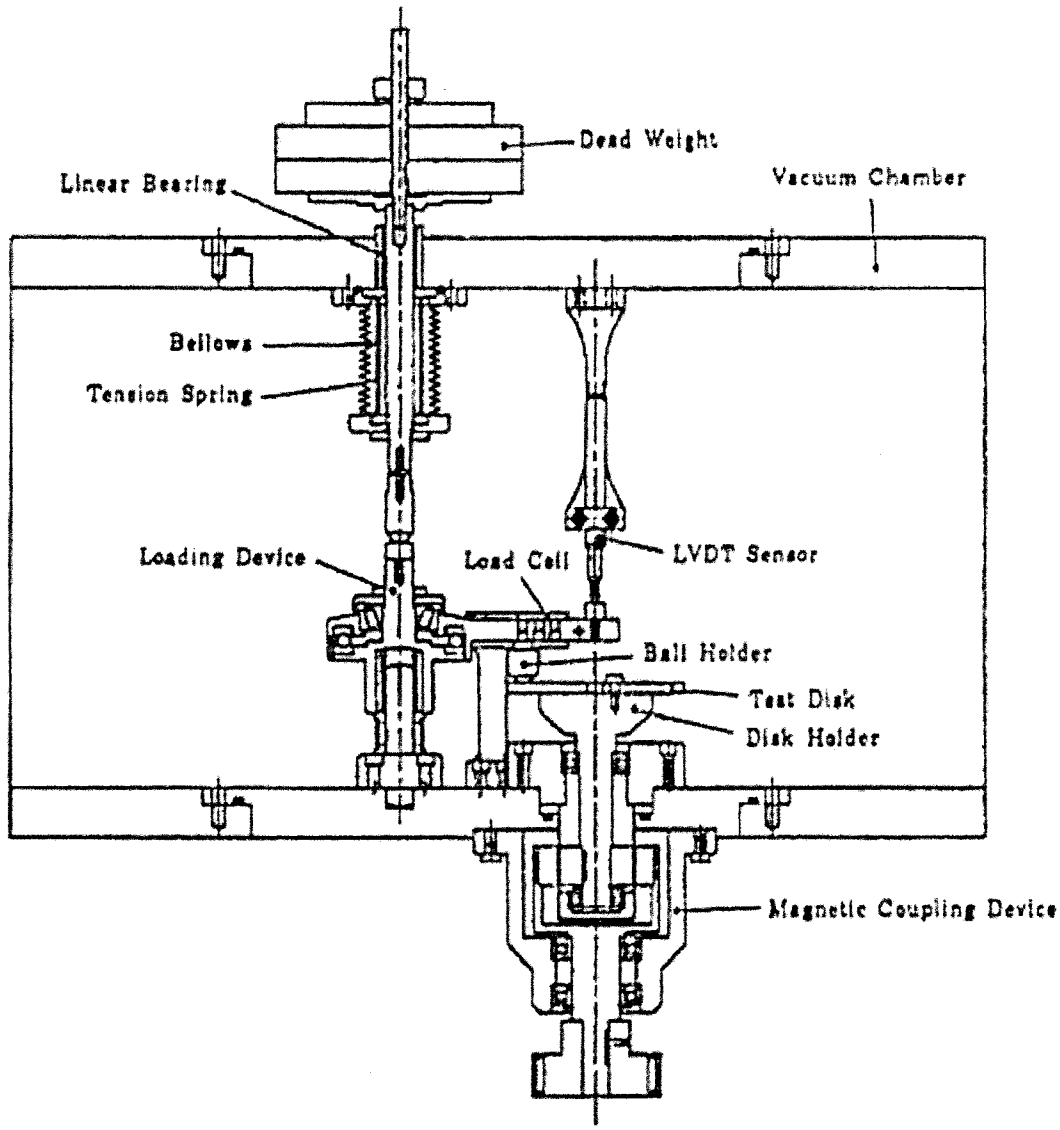

Figure 2.13 A sectional view of the vacuum wear rig used by Kong, et al. inside the vacuum chamber [25]

2.5. Friction and Wear of Pure Metals in Vacuum

Metals and alloys show different coefficients of friction, wear rates, and wear mechanisms in various atmospheric pressures. A review of variations in the tribological properties of pure metals and steel under different atmospheric conditions are given in this section.

2.5.1 Wear Behaviour of Pure Non-Ferrous Metals in Vacuum

2.5.1.1 Iron, Copper, and Nickel

The affinity of metal surfaces to gas chemisorptions is one of the factors that influences the adhesive wear [41]. Sasada et al. [43] carried out a series of experiments on pure metals of Fe, Ni, and Cu. With the same metal combination, total wear showed reduction with decreasing the atmospheric pressure [43]. The wear of Fe- disk, in 101.3 KPa and after roughly 400 m of sliding distance, was measured to be around 200 mg. The amount of wear for pin of Fe at the same pressure and sliding distance was about 30 mg. At a low atmospheric pressure of 133×10^{-6} Pa, the wear of Fe(disk) was reduced drastically to 30 mg while this reduction for Fe(pin) was almost zero [43]. This reduction was also significant for Ni (from 80 mg to 25 mg) when tested at 101.3KPa and 133×10^{-3} Pa . However, Cu and Fe combination showed different wear rates. Although, the total wear increased, the magnitude of wear for Cu (pin) decreases as vacuum increased [43]. The wear of Fe (disk) increased with decreasing the atmospheric pressure. **Fig 2.16** illustrates wear of Fe, and Cu at different atmospheric pressures. The amount of Fe transfer to Cu pin was less than the amount of Cu transfer on Fe disk in ambient atmosphere. On the other hand, in high vacuum of 133×10^{-6} Pa, the greater amount of Fe was transferred to Cu pin. In this atmospheric condition, the amount of transferred Cu to Fe disk was less than that in ambient atmosphere [43]. In contrary, both the wear of Cu and Ni in 0.133 Pa were less than at 101.3 KPa. In ambient atmosphere, the wear of Cu is more than that of Ni. This was vice versa at 0.133 Pa. As for Cu/Fe, there is less of amount of transferred Cu to Ni disk in lower pressure. There were two explanations for the fact that there was more transfer material in lower pressure from harder materials.

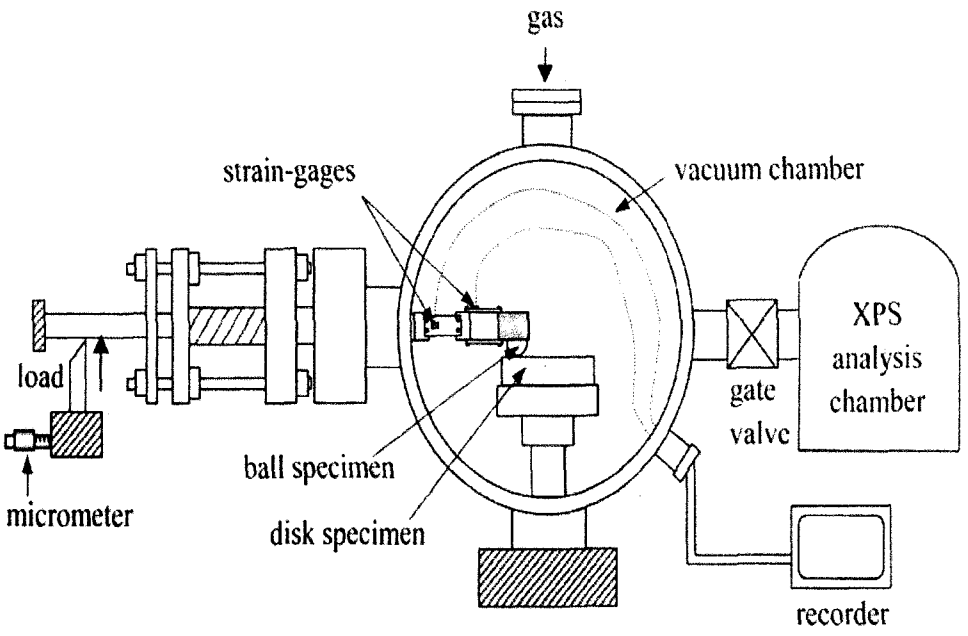

Figure 2.14 Schematic diagram of the vacuum experimental apparatus used by Cong, et al. [60].

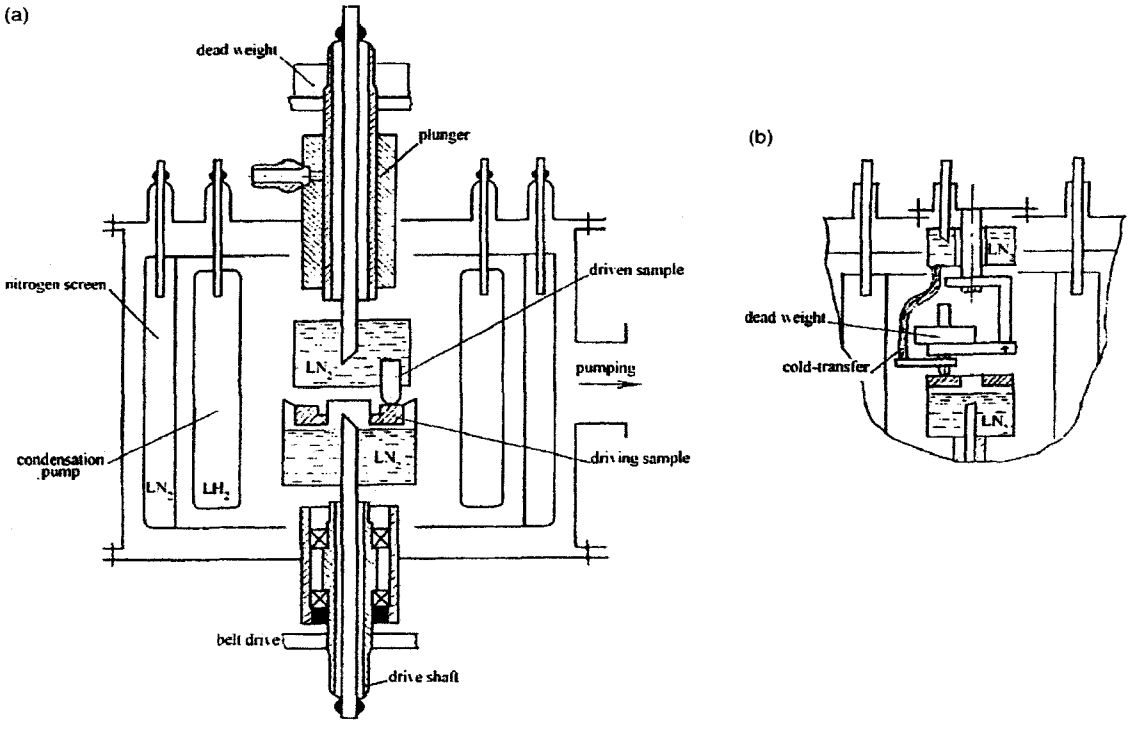

Figure 2.15 Test Device UTI with low temperature vacuum tribometers used by Ostrovskaya et al. [56]: (a) UTI TV-100; (b) Small-load modification UTI.

The first was attributed to the fact that Fe has 6 electrons in the 3d orbital, and Ni has a slightly lower d-character than Fe. At 133×10^{-6} Pa, there is still sufficient gas to destroy the surface activity of Fe and then Ni. The activity of gas chemisorptions for copper is lower than those for nickel and iron. Thus, there is almost no activity for Cu surface in vacuum of 133×10^{-6} Pa [43]. The other explanation was attributed to the hardness of metals. The shearing fracture, which causes production of the small transferred fragments, occurs mainly in the softer of the metal surfaces in contact. The fresh surface of harder metal losses its surface energy because of the affinity for gas chemisorptions on harder metals. Therefore, fragments do not adhere to the harder surface, but to each other [43]. It is found that for the FCC structures the wear rate decrease as the adhesion energy increases, while in BCC structure metals, both wear rate and adhesion energy increase simultaneously (in atmospheric pressure of 133×10^{-9} Pa to 133×10^{-7} Pa) [57]. According to Chen and Rigney [62] the energy required per unit area to break an interface into two free surfaces is called the adhesion energy.

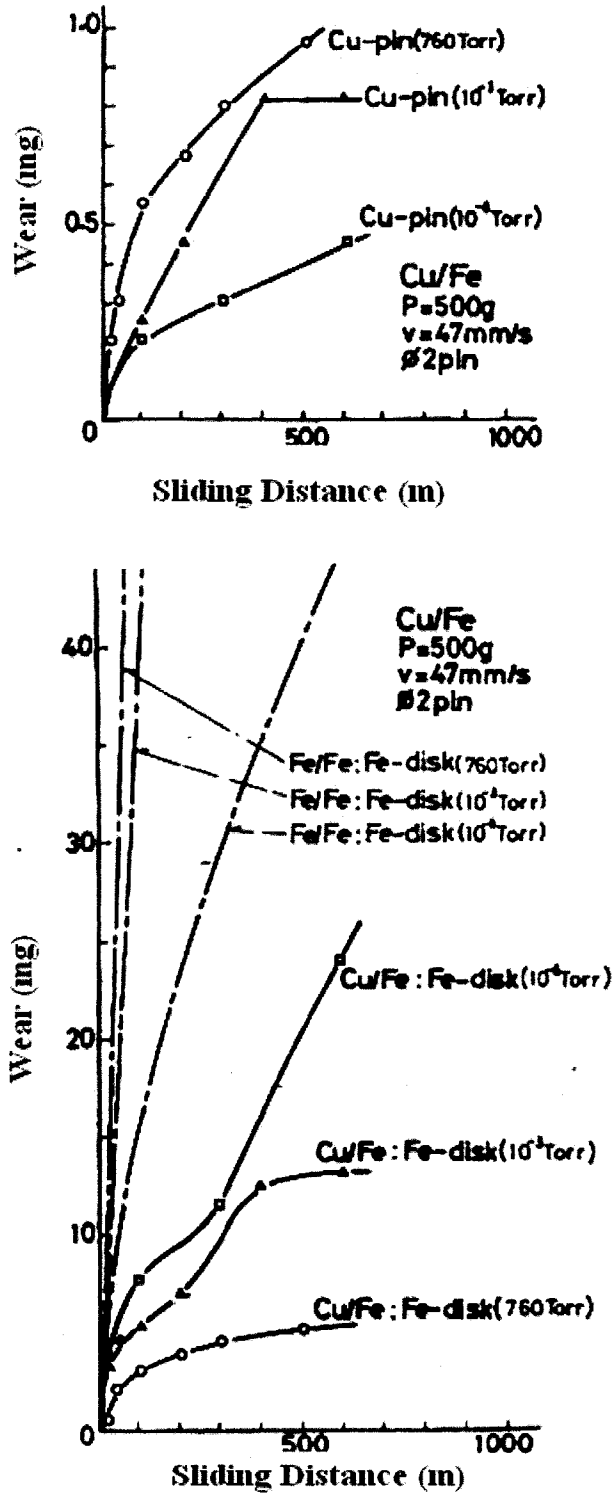

Figure 2.16 Wear in different metal combination in different atmospheric pressure: (A) wear of Cu pin rubbed against Fe disk, and (B) wear of Fe disk rubbed against Cu pin [43].

2.5.1.2 Aluminum and Simple Aluminum Alloys

One of the elements that have been investigated in vacuum is aluminum. The value of stacking fault energy (SFE) for aluminum and simple aluminum based alloys is high. It is known that higher SFE is accompanied by the higher dynamic recovery. Al is ductile and its mechanical properties are known to be substantially temperature dependent. Huo and Rigney [63] conducted several experiments on high purity aluminum pin (HP), and commercial purity 1100 aluminum (CP) in vacuum at a pressure of 3×10^{-3} Pa. The disk was M2 tool steel with the hardness of 63 HRC. The microstructures of these two materials found to be almost dislocation free. After test, the hardness of HP remained constant with depth and even near sliding interface (50-60 Knoop hardness (HK)). The CP showed considerable work hardening near the surface. It was 130 HK at the depth of 12 μm while the magnitude for the depth of 50 mm was 70 HK. SEM indicated the extruded material on the pins. The extruded material was flake like, and flake like debris was produced as a result. Friction traces featured large periodic fluctuations because of mostly lamellar shape of extruded material [63]. At the velocity of 0.0008 m/s, the TEM micrograph showed a longitudinal and elongated substructure while at the velocity of 0.02 m /s, dislocation structures consist of more and less equiaxied sub-grains. Kuo et al. [63] claimed that higher temperature generated during high velocity tests caused dynamic recovery process. In case of CP, the sliding sub-surface consisted entirely of sub-grains elongated in the sliding direction. At a much larger distance from the interface (30 μm), more equiaxed dislocation cells were detected. CP was reported to have elongated grain structure along the bar axis in other report [64]. The temperature is a factor for the sliding velocity of 0.02 m/s and load of 10 N. Therefore, recrystalization might occur at higher velocities [63]. In comparison to the tests performed in vacuum, test on CP showed the higher coefficient of friction in air in a tribo-system of ball (52100 steel)-on-disk (CP) [62-63]. The wear tracks on the CP disk tested in vacuum were smooth and shallow. However, wear track after tests in air was tough. The debris particles from CP were plate like and sometimes as large as 1mm in length. The hardness of track in air higher that the track in vacuum (171.1 VH in air and 112.8 VH in vacuum). The presence of alumina was confirmed by observation of local patches of mixed material containing oxygen on specimens tested in vacuum. According

to experiment conducted by Hiratsuka et al. [42], in comparison to air, the wear rate of aluminium was decreased in vacuum pressure of 1.6×10^{-4} Pa. This experiment was implemented by means of pin (Al)-on-disk (Al). The magnitude of coefficient of wear in 101.3 KPa and in steady state was 5.7×10^{-5} (mm^3/N.m) while it was decreased to 7.4×10^{-8} (mm^3/N.m) under vacuum. Vickers' hardness test indicated that the hardness of aluminum surface, transfer particles and debris produced in air were much higher that those in vacuum. Therefore, there was no correlation between hardness and amount of wear in this tribo-system.

2.5.1.3 Wear and Friction of Steel:

According to Kong et al. [25], Wear rates in vacuum were less than severe wear rates in air. Debris consisted of α-Fe, despite the fact that some Fe_3O_4 was reported. Although the result have been taken at medium vacuum (0.133 Pa), yet, the oxide debris was detectable. It means that even in low vacuum, a thin film of oxide may be formed on the surfaces and that causes significant reduction in friction [24,25]. The COF of SS41 mild steel in high vacuum of 5×10^{-3} Pa was higher than that in medium vacuum of 1.3 Pa [52]. It was observed that in the steady state, COF of mild steel in ambient air is higher than the one in medium vacuum (**Fig 2.17**). It was caused by formation of thin layer of Fe_3O_4 steel oxides on the surface under a medium vacuum, at which surface oxidation is fast promoted by a high surface temperature (range of 400-650 °C) [24]. It was pointed out that in presence of Fe_3O_4 the COF for the mild steel is less than Fe_2O_3. **Fig 2.18** shows the wear rate and microhardness of the pin (1045 carbon steel) in vacuum under the 50 N load and 2×10^{-5} Pa vacuum pressure. Higher sliding velocity causes higher temperature at the sliding contact and as a result the frictional heating in local areas of the material rise to the austenitizing temperature [56]. The sharp cooling of these areas after the friction contact provides the conditions for friction hardening in local volumes with formation of extremely hard martensite-type secondary structures and leads to substantial hardening of the friction surface [56]. Typical wear particles size at room temperature were around 480 μm and typical wear particles microhardness were reported to be 12 GPa. During friction in vacuum, the particles separated from the bulk material take part continuously in the friction process because of considerable adhesion [56].

2.6. Tribology of Ti Based Alloys

High specific strength, excellent corrosion resistance [65] make titanium and titanium alloys an outstanding choice in aerospace, space, medical device, and recently for automotive industries [66]. Titanium and its alloys are among the most appropriate materials for biomedical applications, due to their well-established corrosion resistance and biocompatibility. They owe their excellent corrosion resistance to passive oxide film formation at room temperature [4]. Because of the extensive nature of their applications, several studies were conducted on the wear and friction of these materials.

2.6.1 Titanium, Titanium Alloys and Their Properties

Pure titanium has a low-density of 4.5 g/cm^3. The titanium has good resistance to oxidation up to 593 °C. Ti is a reactive metal that can pick up and dissolve (interstitially) the elements oxygen, nitrogen, and hydrogen [65]. It has very high melting temperature (1668 °C). The allotropic transformation from the HCP lower-temperature form to the BCC higher-temperature form limits its application temperature to 882 °C [65]. Titanium has an intermediate modulus of elasticity (103 GPa). It has a good ductility, and can be hot formed in variety of shapes. Titanium undergoes an allotropic transformation from HCP (alpha phase) to BCC (beta phase) at about 882 °C. Some elements promote higher transformation temperatures (alpha stabilizers) and others promote lower temperature (beta stabilizers) [65].

Titanium alloys divide into three major classes: these are α, α -β and β. Additional phases are possible. The β-phase can transform to a martensitic α-phase upon cooling. In addition, secondary phases can be precipitated or formed by deliberate alloy additions. Phases such as omega, α-two (Ti_3Al), interface phase and gamma (TiAl) play a role in determining the properties of titanium alloys [65]. Acicular and equiaxed forms of microstructures can be seen in titanium alloys. Aluminium, oxygen, nitrogen and hydrogen stabilize the α-phase, whereas vanadium is good for the β-phase [65, 67]. Stabilizing α-phase rises temperature of the α-β transformation. α-β alloys have higher strength and respond to heat treatment but are less formable than α-alloys. This class of

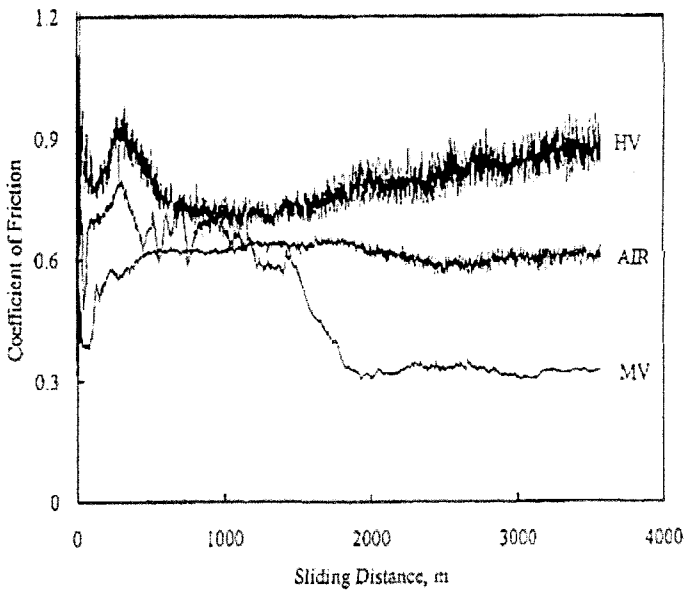

Figure 2.17 Friction under various conditions of air pressure (high vacuum, 5×10^{-3} Pa; medium, 1.3 Pa) [25].

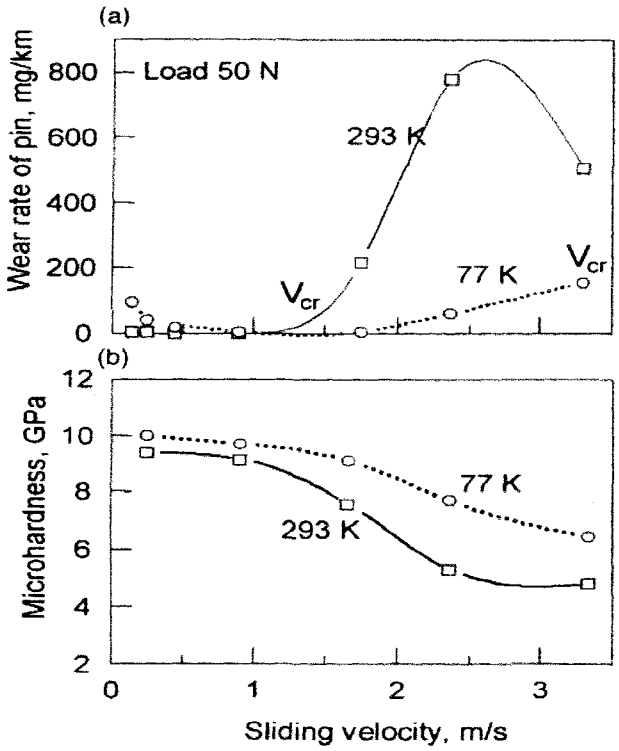

Figure 2.18 Wear rate of a 1045 steel pin (a) and micro-hardness at the pin friction surface (b) vs sliding velocity in vacuum under 293K and 77K [56]

titanium alloys accounts for more than 70% of all titanium alloys. Ti-6Al-4V has excellent strength and elevated temperature properties [65].

Ultimate strength, creep resistance, elastic modulus, and melting temperature are at 1100 MPa, 300 °C, 110GPa, and 1651 °C, respectively [55, 58, 59, 68] By alteration of the amounts of allotting elements and heat treatment, a variety of properties can be achieved in α+β alloys.

Most α+β alloys have high-strength and formability, and contain 4-6 wt% of β-stabilisers that allow substantial amounts of β to be retained on quenching from the β→α+β phase fields, *e.g.* Ti-6Al-4V. Reduction of density, stabilization and strengthening of α-phase are attained by presence of aluminum whereas β-phase is promoted by vanadium mostly for hot-working [69]. **Fig 2.19** depicts the schematic phase diagram of Ti-6Al-4V. Upon cooling from different high temperatures, various phases may form, e.g. α prime, acicular α, plate-like α etc. [67]. **Fig 2.20** illustrates typical microstructure of Ti-6Al-4V. Using a dislocation mechanics-based model plasticity model, Y. B. Guo et al. [70] drew a curve for stress-strain of Ti-6Al-4V at two different temperatures.

2.6.2 Role of Oxygen in Wear and Friction of Titanium Alloys

Poor wear resistance of Titanium alloys is attributed to low resistance to plastic shearing (frictional force), low work-hardening (**Fig 2.20** exhibits very low slope for stress-strain curve) and the low protection exerted by the surface oxide which forms as a consequence of the high flash temperatures induced by friction during dry sliding [51, 71]. Several tests had been done by using disk-on-disk (Ti-6Al-4V on Ti-6Al-4V or AISI M2 steel), pin-on-disk (Ti-6Al-4V on AISI 52100 steel), and pin-on-disk (Titanium-aluminum, Titanium-molybdenum, and titanium-lead on hard steel) configurations at room temperature [13, 14, 51, 58, 71]. A correlation was observed between the wear rates of Ti-6Al-4V at different loads and velocities using disk-on-disk configuration tested against itself and Ti- 6Al-4V on AISI 52100 steel. In the latter case by increasing sliding velocity and at different loads, the wear volume decreased to the certain level, and then it

was increased. As the load increased, the transition point occurred faster. For instance, at a load of 50 N the transition occurred around a sliding velocity of 0.6 m/s while the transition at the load of 200N the transition was about 0.4 m/s [14, 71].

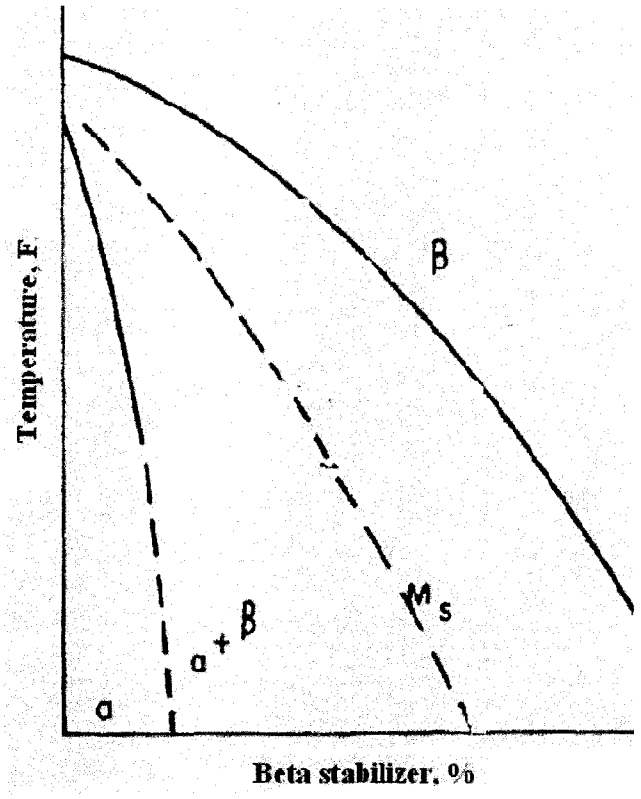

Figure 2.19 Phase diagram of Ti-6Al-4V. Quenching the β phase leads to the formation of h.c.p. α' martensite (α prime). This is not particularly hard and there are increasing quantities of retained-β in the microstructure as the solute concentration increases and the M_S temperature decreases [67].

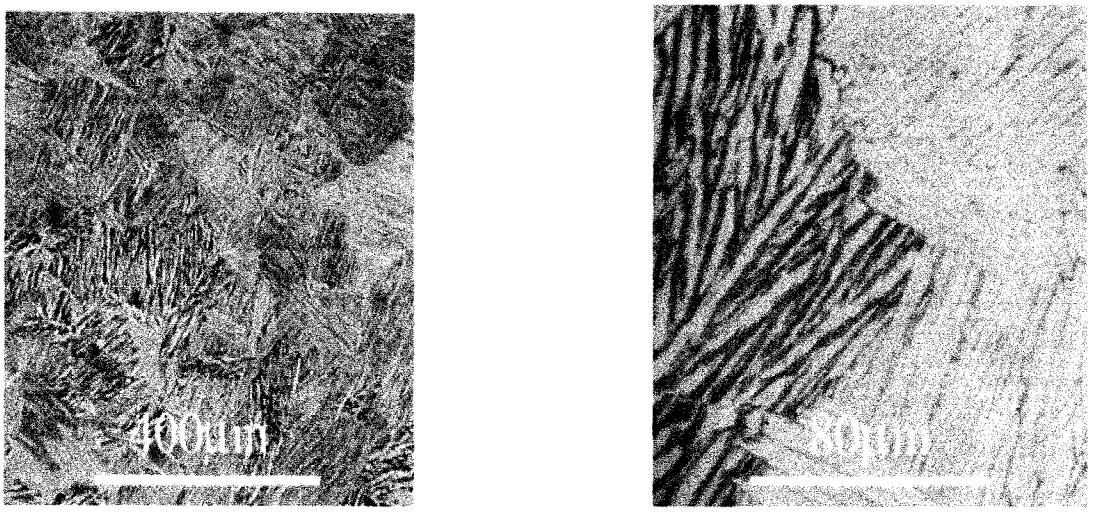

Figure 2.20 Typical microstructure of Ti-6Al-4V cooled from alpha phase and field to produce Widmanstätten β structure [69].

However, no transition was demonstrated in Ti-6Al-4V with a hardness of 350 HV_{10} tested against AISI M2 steel with a hardness of 65 HRc [14]. Although there was not a minimum point in the case of the Ti-6Al-4V alloy sliding against the AISI M2 steel, a transition was observed since wear become more and more controlled by metallic wear as the sliding velocity is increased [13]. **Fig 2.21** illustrates the results of the volumetric wear versus sliding speed tested at various loads for both configurations. The wear volume increased with the applied load at any sliding speed in all cases [13, 14, 58, 71]. At very low speed, the XRD spectra of debris depicted that titanium oxide prevailed, although alpha titanium existed as well [13, 14, 51, 58, 71]. This observation demonstrated the occurrence of a strong interaction with the environment, favoured by the high reactivity of Ti alloys with oxygen [65]. At the lower sliding velocity, wear debris were very loose and fine, and some of the debris can be in plate-like shape [13, 58, 71]. It reminds the characteristics of the oxidative wear. Borgioli et al. [18] confirmed this fact. The analysis of the wear debris showed that they consisted of titanium plates and small TiO (F.C.C.) oxide particles at the sliding velocities of 0.4 and 0.8 m/s. The volume fraction of oxide decreased as the sliding velocity increased. At 1.6 m/s, no traces of oxide were detected. The observation suggested that the wear was due to oxidation and delamination phenomena and that a transition from oxidation wear to delamination dominated wear occurred as sliding velocity increased [18]. The amount of oxide was always the higher in case of sliding the Ti-6Al-4V against relatively harder materials [13, 58, 71]. The morphology of debris at low velocity tests showed typical delamination features [13, 58, 59, 65]. The worn surface of Ti-6Al-4V at low speed showed the presence of smooth compacted layers aligned in the direction of sliding and damaged by brittle fracture [13, 58]. On the other hand, when surface oxidation predominates, plastic shearing of the subsurface layers occurred [13, 58, 59]. During sliding of Ti-6Al-4V against itself and hard steels at a low speed, wear track exhibited a micro-fragmentation process [13, 58, 59, 65]. Higher wear rate of Ti-6Al-4V tested against a harder surface (and at a higher velocity) was attributed to the abrasive action of the hard carbides on the counterface (AISI M2 steel) [13]. Plastic shearing of the subsurface was influenced by the applied load whereas the oxidation mechanisms and is directly associated with the sliding velocity and of course surface temperature [58, 71].

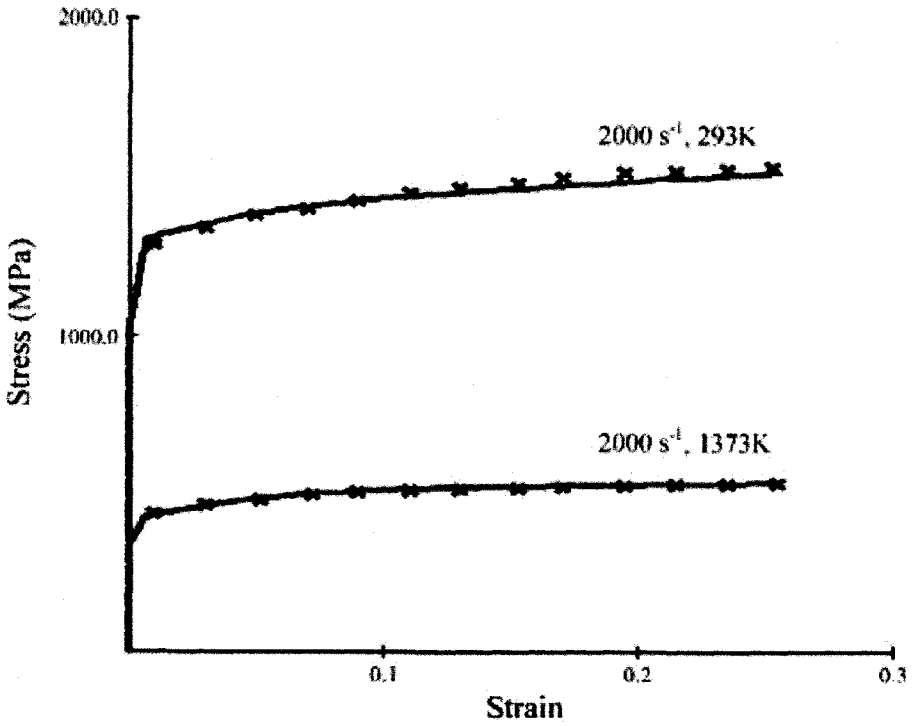

Figure 2.21 Stress-strain curve of Ti-6Al-4V alloy at room and elevated temperatures [70].

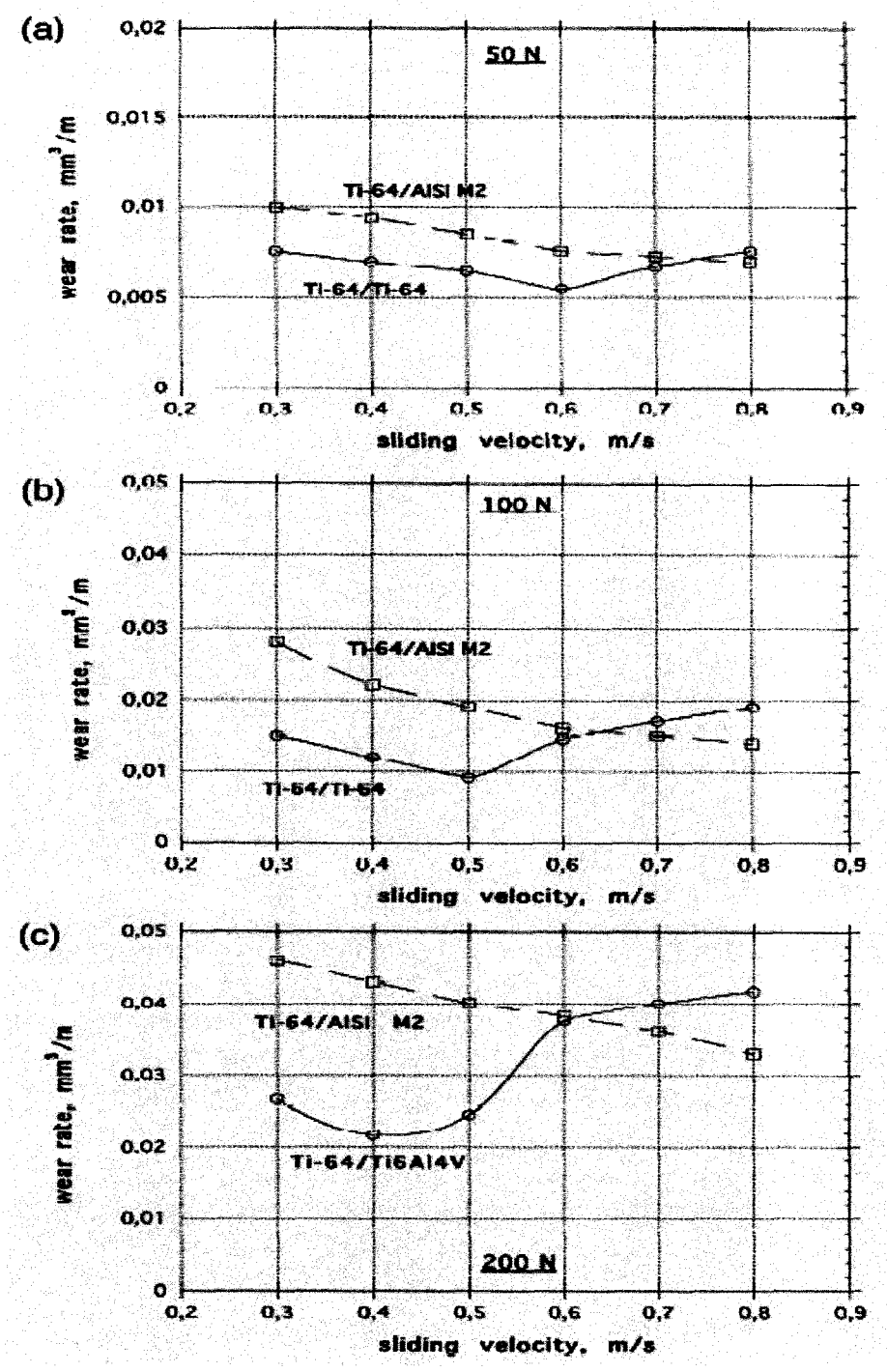

Figure 2.22 Wear rate of the rotating specimen of Ti-6Al-4V on itself and on AISI M2 steel as a function of sliding velocity investigated at the applied load of 50 (a), 100 (b) and 200 N (c) [13].

The frictional behaviour of Ti-6Al-4V was investigated by several investigators [59, 65, 68]. The pin-on-flat surface type tests were conducted using 75 and 250 N normal load. The pin made of Ti-6Al-4V was put reciprocating action against the maraging steel surface [68]. The COF versus the number of cycles (in log scale) continuously increased until a steady-state (about 0.5) was reached. Qu et al [65] conducted experiments using 440C type stainless steel, silicon nitride, alumina (as ball) on a disk of Ti-6Al-4V. A normal load of 10 N was applied while two sliding velocities of 0.3 m/s and 1.0 m/s were used. The steady state COF was about 0.5. This COF was confirmed by the other reports [59, 68]. However, in the case of 440C stainless steel (**Fig 2.23**), the COF initially started from a high magnitude and after 20 sliding cycles it dropped. From this point COF began to increase and reached to a steady point. By increasing the sliding velocity, a lower COF was detected. On the surface of stainless steel ball, EDS analysis showed the presence of aluminium and titanium. Qu et al. [65] explained that the impact may introduce failure, such as cracking and crushing of the contact surfaces, leading to faster material removal and the production of sharp debris fragments that can cause abrasion of titanium alloys [65].

2.6.3 Friction, Wear and Wear Mechanisms of Ti-6Al-4V in Vacuum

In vacuum (10^{-5} Pa) the wear rate of Ti-6Al-4V pin with hardness of HRV 345 tested on a AISI 52100 steel with the hardness of HRC 62 was much lower than that wear rate in ambient atmosphere [14, 58]. At load of 50 N and sliding velocity of 0.6 m/s, the wear rate in air was around 30 mg/km whereas in vacuum (10^{-5} Pa) the ware rate was 7 mg/km. Generally increased the sliding velocity increases the wear rate as depicted in **Fig 2.24**. The XRD did not revealed any trace of titanium oxide in the debris produced in vacuum [58]. The abrasion and adhesion processes both happened in air while the adhesion was the only mechanism that controlled wear in vacuum [51, 58]. The original grain size of sample was reported as 100μm. At 40 μm from the surface a high density of dislocations and a ultra-fine grain size of 50-100nm formed in the subsurface of Ti-6Al-4V pin sliding on a steel disk in vacuum [14]. The large stresses could be the result of adhesion on the sliding surface, which add to the shear stresses between the sliding surfaces, and is an addition to the normal load. The SEM micrographs in **Fig 2.25** depict

the cross-sectional microstructure of the Ti-6Al-4V pin before and after wear testing at 10^{-5} Pa. The acicular form of the microstructure before the test can be seen (**Fig 2.25**). Large wear debris in the form of plates was observed under different vacuum pressures [58-79]. SEM micrographs for wear test under 0.6 m/s and at 70 N showed that the size of debris in vacuum is three times larger that it in air pressure [58].

In vacuum, for the unlubricated Ti-6Al-4V (pin) in contact with the bare high-nickel-content super-alloy (disk), under a load of 4 N and at low speeds (0.0005, 0.0009, 0.008, and 0.036 m/s), the COF was initially 0.31[59]. The presence of oxides and contaminants on the surfaces of the bare Ti-6Al-4V pin and this super-alloy contributed to the low initial COF. A "Stick-slip" behaviour became dominant after a few sliding passes. Then, the COF rapidly increased and reached the equilibrium at 1.1 for a long sliding passes [59].

In conclusion, it has been observed that the wear rates and COF of Ti-6Al-4V are different in different test atmospheres. These properties are also affected by velocity and magnitude of normal load. The wear rate of Ti-6Al-4V alloy in air was higher that that in vacuum. At low velocity tests in air, oxidational wear mechanisms become dominant. As the velocity increases, the delamination and abrasive wear mechanisms take over. The COF in vacuum was observed to be much higher than that in air. However, in both case COF reached a steady state after a short time.

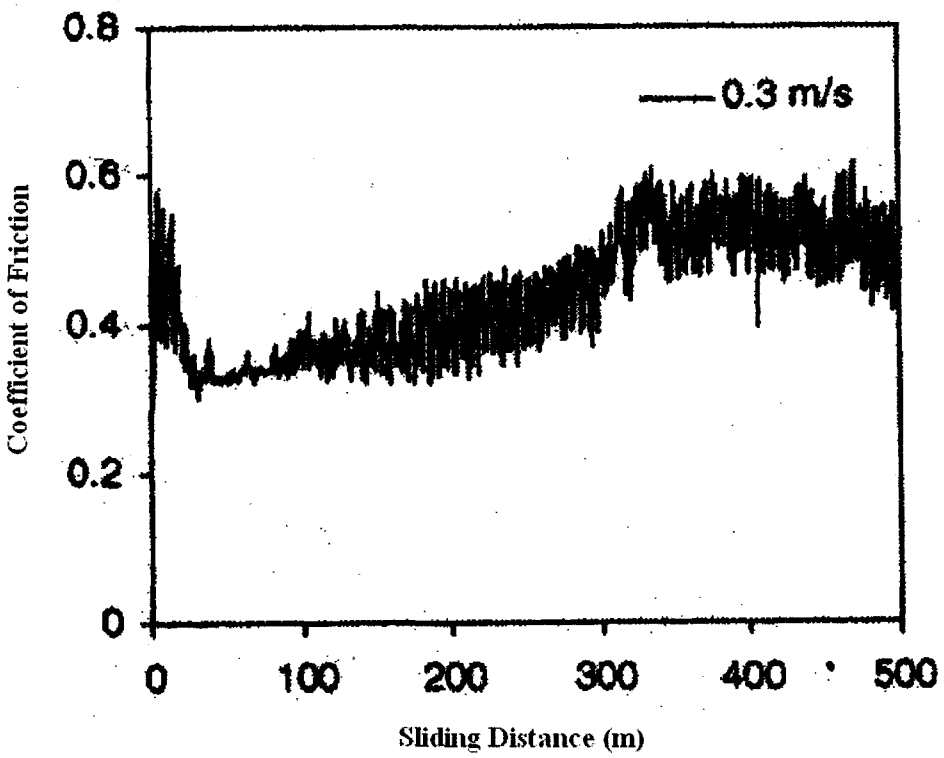

Figure 2.23 Coefficient of friction versus sliding distance for sliding the ball of 440C stainless steel on the disk of Ti-6Al-4V under normal load of 10 N [68].

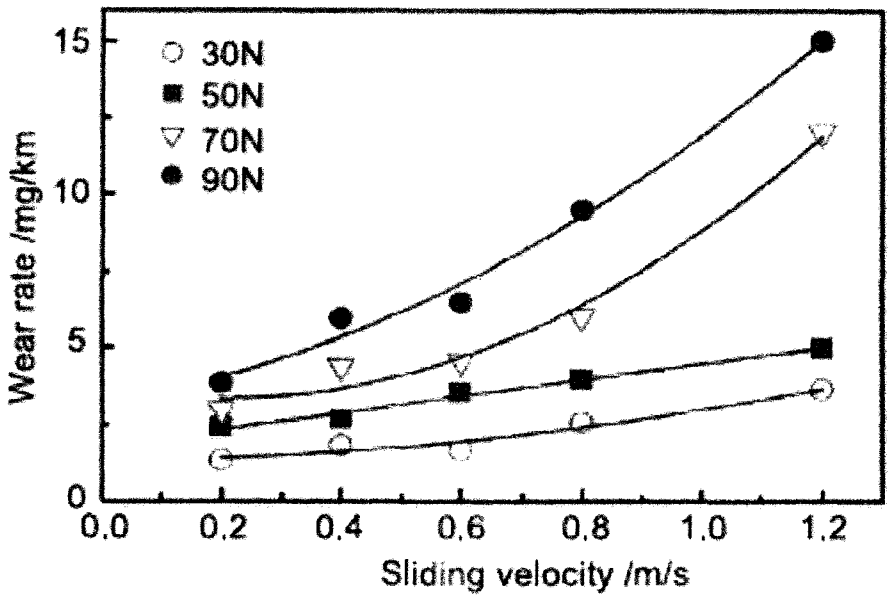

Figure 2.24 Wear rate of Ti-9Al-4V alloy as a function of sliding velocity for different applied loads in vacuum (10^{-5}) [14].

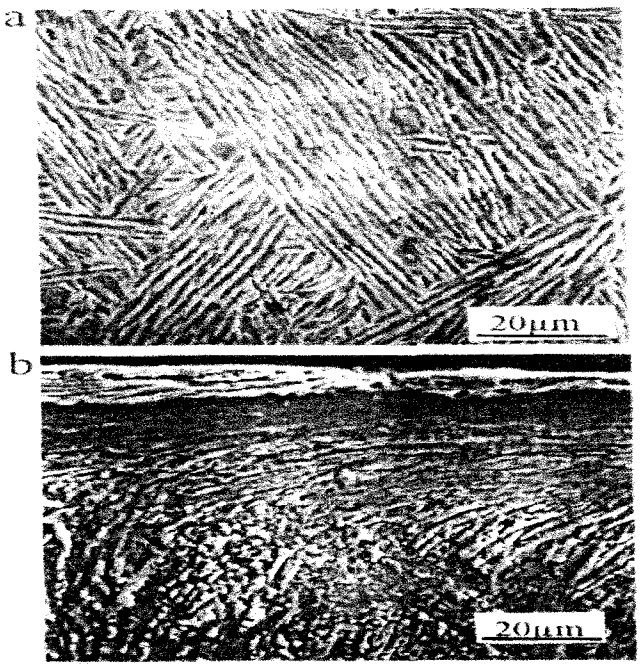

Figure 2.25 SEM micrographs showing (a) microstructure prior to wear test and (b0 cross-sectional laminar microstructure of the Ti-6Al-4V alloy (pin) sample after wear at a velocity of 0.6 m/s in vacuum (10^{-5} Pa) [14].

2.7. Application of Thermal Oxidation Method to Improving Tribological Properties of Ti-6Al-4V Alloy

It has been suggested that the poor tribological properties of titanium and its alloys may be improved through a surface engineering solution [4-5, 15-18, 72]. In the last five years, a variety of coatings have been used on the titanium and its alloys, particularly on Ti-6Al-4V alloy surfaces [4-5, 15-18, 72]. Among all the surface engineering processes, the most effective one has been called the oxygen diffusion hardening (ODH) or thermal oxidation (TO) process. This method has been successfully used for the surface treatment of titanium components for off-shore and racing car engine industry [15]. Oxidation, particularly at temperatures above 200 C, promotes the development of a crystalline oxide film [4]. To understand effect of the thermal oxidation process in enhancement the tribological properties of Ti-6Al-4V, wear tests were performed in different environmental conditions. The following sections summarize the details and the main results of the experiments.

2.7.1 Environmental Conditions and Surface Characterization

The oxidizing treatments were carried out in ambient atmosphere at 600, 650, and 900 °C between 12 ands 65 h [4-5, 15-18, 74]. Investigations of surface layers displayed presence of 3 main tribo-layers due to the thermal oxidation. On the TO-treated surfaces, thin layers rutile oxides with thickness of 1 to 4 μm are formed [4-5, 15-18, 74]. The middle layer, which is thicker (8-20 μm), is the area of oxygen diffusion zone [4-5, 15-18, 74]. The unaffected part of Ti-6Al-4V is the adjacent layer to the oxygen diffusion zone (**Fig 2.26**). Sliding surfaces were carried out with lubricant (Shell 20/20 W) [15], and without lubricant both in ambient air [17-18], and in a 0.9% NaCl solution at 37 °C and room temperature [4, 6, 74]. The average of surface roughness was increased up to 4.6 times with respect to untreated polished samples. A High hardness of 1300 HV_5 has been determined for TO-treated Ti-6Al-4V.

2.7.2 Wear of TO-treated Ti-6Al-4V

The tests under the lubricated conditions showed that the untreated Ti-alloys were characterised by a very high wear rate in comparison to thermally oxidized titanium

alloys [15]. This high mass loss of untreated titanium alloy was attributed partially to the abrasive action of transferred material. The pulled-out material was transferred and smeared onto the surface of the counterface [15]. The adhesive strength of the junctions that are formed is usually higher than the strength of Ti-6Al-4V, and such junction ruptures within the weaker titanium asperities, which accounts for the many craters on the worn surface of the untreated material [15]. The dramatic decrease in the mass loss of TO-treated sample and counterface reveals the replacement of the metal-to-metal contact by a TO-treated ceramic-to-metal contact. After the wheel-on-wheel test of hardened 709M40 steel on TO-treated Ti-6Al-4V (under 3N and 5N of normal load and at low sliding velocity), the SEM morphology illustrated 3 areas (**Fig 2.27**). Area 'A` represented the thermally oxidized surface with the fine spherical oxide features. The EDS of Area 'B` showed high peaks of Fe, thus it was the real contact region. EDS analysis of area 'C` revealed a much lower oxygen peak than in either of areas 'A` or 'B`, suggesting the flaking of the oxide has occurred in this area. It was concluded that during sliding only a small portion of the nominal contacting area was really in contact [15]. Dong, H. et al. [16] reported that the Young's modulus to hardness ratio of rutile in thermally oxidized Ti-6Al-4V is lower than the ration for untreated titanium alloy. Thus, it causes promotion elastic deformation and reduces adhesive wear.

In another attempt, wear tests were executed in ambient condition using a reciprocating wear tester (ball-on-disk) at a normal load of 1.5 N and a sliding speed of 0.02 m/s [17]. TO-treated Ti-6Al-4V was in the shape of a disk. Al_2O_3 Balls of 10mm diameter, which created a contact pressure of 31.5 kg/mm^2 on the surface, were used as counterfaces. On the untreated surface, formation of wide and deep wear track was accompanied by the creation of a large amount of wear debris. Profilometeric measurements could not identify any traces of wear track on the oxidized surface. On the oxidized surface, wear progressed by deformation and removal of the asperities, and apparently, local breakdown and flaking of the oxide layer. No wear track could be observed was detected on the oxidized surface. The experiment showed that thermal oxidation treatment suppressed the extensive wear of the Ti-6Al-4V [17].

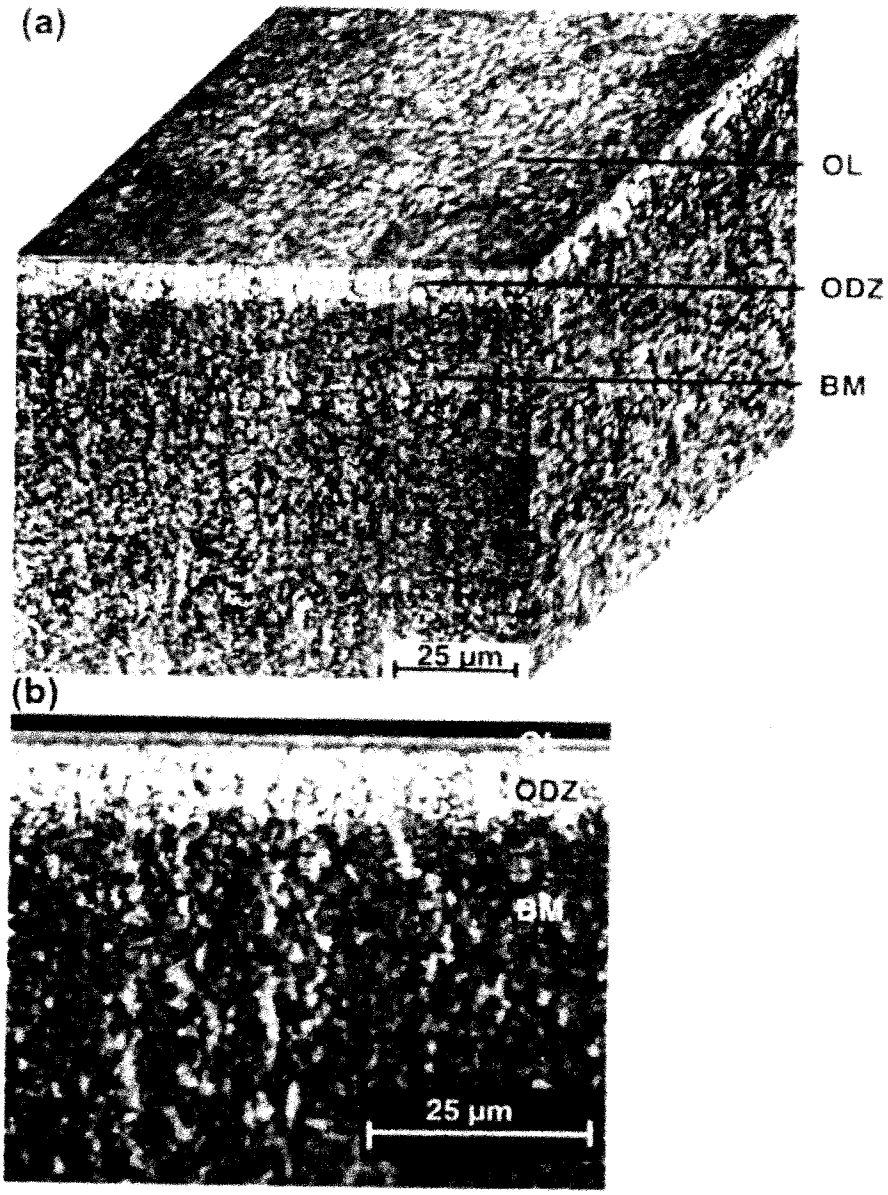

Figure 2.26 (a) 3-D and (b) 2-D cross section optical micrographs of sample oxidised for 60 H (OL; oxide layer, ODZ: oxygen diffusion zone, and BM: base metal) [17].

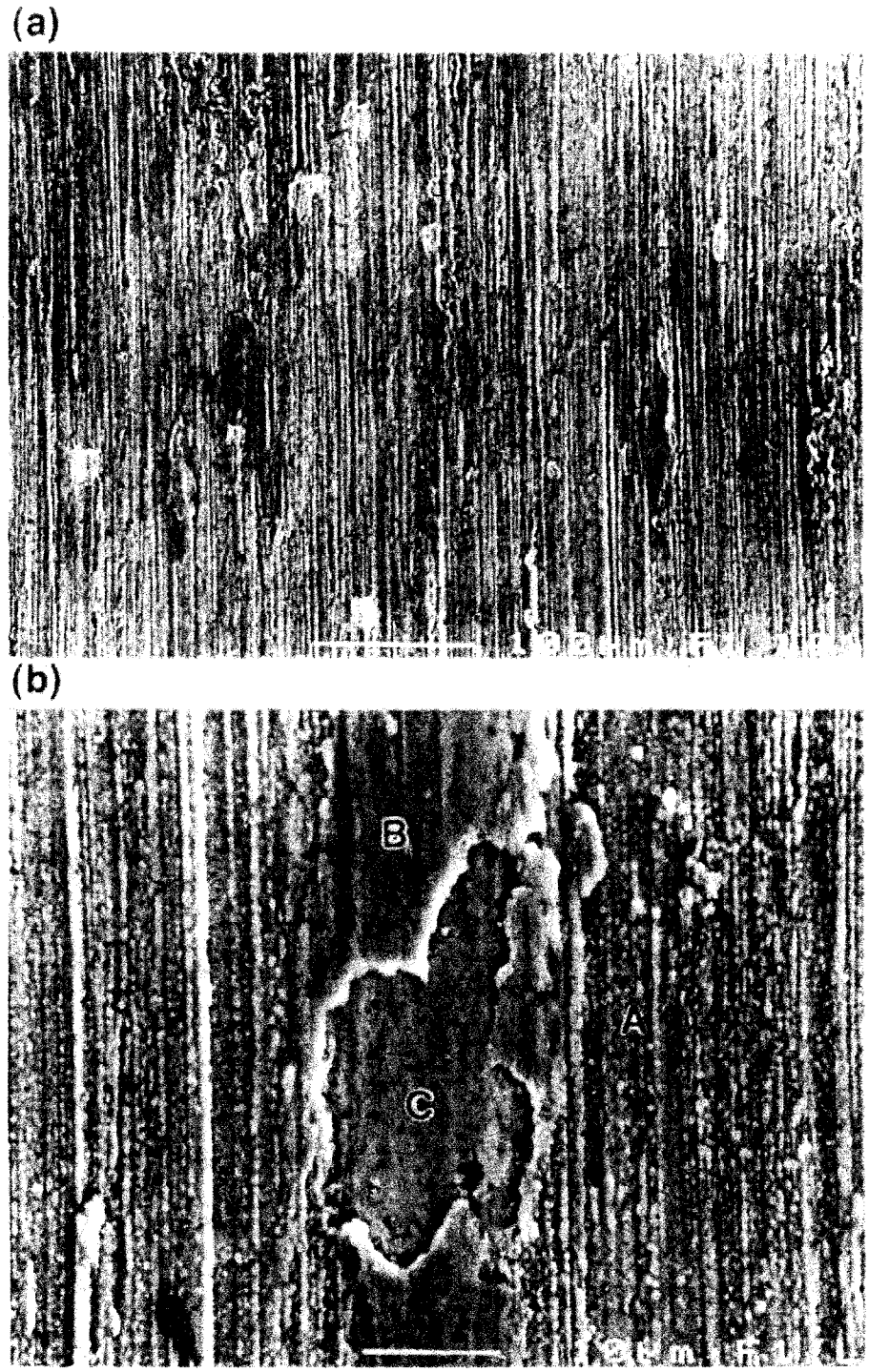

Figure 2.27 SEM micrographs of the worn surface of TO-treated Ti-6Al-4V specimen, showing (a) the general wear morphology, and (b) a typical wear feature. (the direction of sliding is from top to bottom) [15].

Evaluation of sliding wear behaviour of TO-treated Ti-6Al-4V alloy against the AISI O2 steel was a goal for other researchers [18]. Wear resistance was tested by means of a tribo-tester in block-on-ring configuration. A load of 50 N and a sliding velocity of 0.4-1.6 m/s were applied in ambient air. Wear debris showed titanium plates and small TiO particles. As the velocity increased, the plate like debris formed larger size but less amount of TiO particles have been observed. The thermal oxidation of Ti-6AL-4V alloy allows to shift the transition to delamination wear towards slightly higher sliding velocities and to substantially improve the wear resistance [18].

Guleryuz, H, et al [4] showed that more deeply hardened layers were achieved by varying time process and temperature (**Fig 2.28** and **Fig 2.29**). In corrosion-wear test of Ti-4Al-4V against an Al_2O_3 ball in an environment of isotonic serum containing 0.9% NaCl, they found that a shallower and narrower wear track was formed on the oxidized surfaces compared to the untreated ones. A report of the sequential abrasion and corrosion actions on the untreated and TO-treated surface conditions was considered [5]. It was assumed that sequence of the events was experienced by bio-implant materials made of Ti-alloys. In Comparison to an AIP-TiN coated and the untreated sample, the least amount damage was observed on TO-treated sample during the scratch test (applied load:5 N, sliding speed: 0.025 m/s). TO-treated sample was very stable in physiological saline (0.89 wt.% NaCl solution) [5].

Although the wear rate of TO-treated Ti-6Al-4V has been studied in some atmospheric conditions, there is no systematic consideration on COF of this material in literatures.

In summary, it is safe to state that the thermal oxidization method has led to an improvement in wear resistance of Ti-6Al-4V in ambient air and a corrosive environment. Higher hardness of the oxidized surface was considered to be the major contributor to the improvement in tribological properties.

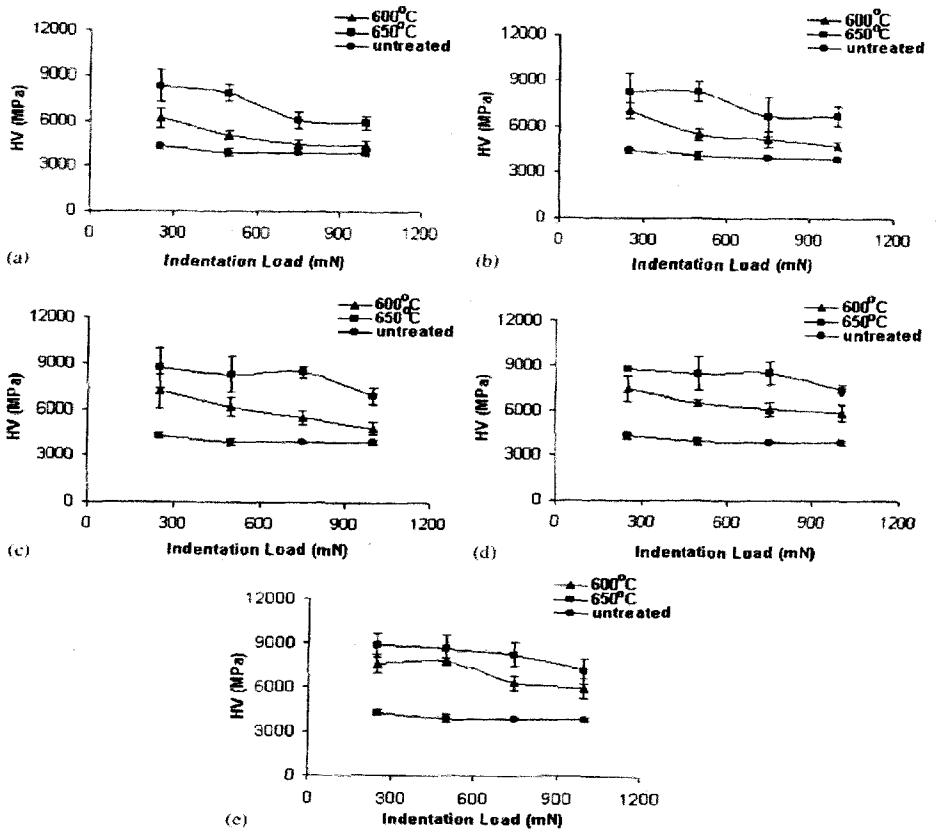

Figure 2.28 The effect of oxide temperature on the Vickers hardness (HV) values of the oxidized surfaces for oxidation times of (a) 12, (b) 24, (c) 36, (d) 48 and (e) 60 h [4].

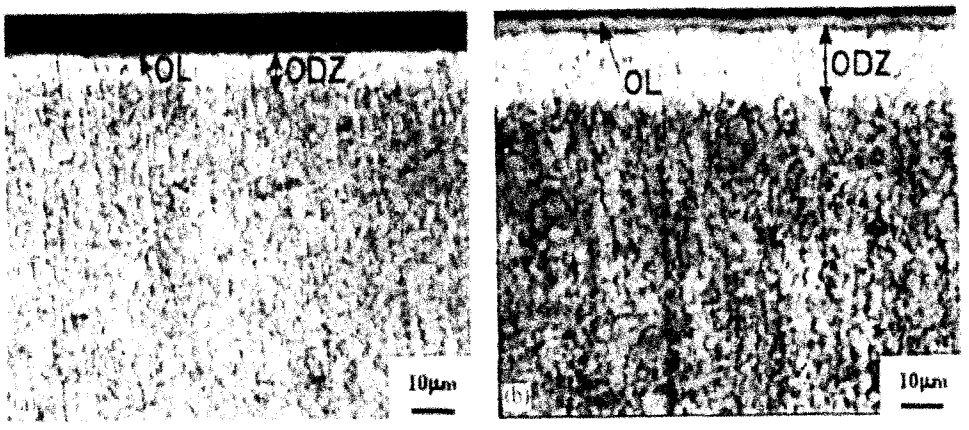

Figure 2.29 Cross-sectional optical micrographs of the thermal oxidized sample (a) at 600 °C for 60 h and (b) at 650 °C for 60 h (OL: Oxide layer, ODZ: Oxygen diffusion zone) [4].

2.8. Objectives of This Project

In the light of the literature survey on the wear of Ti-alloys it becomes clear that the performance of tribological layers formed during thermal oxidization of Ti-6Al-4V has not been addressed under low atmospheric pressures. On the other hand, so far, the experiments on Ti-6Al-4V alloys have been conducted using high normal loads and velocities. These loading conditions intrinsically promote oxidational wear mechanism. To have a set of tests with less restriction on the way, the objectives of the current work consists of two distinct parts:

1. Achievement of a higher wear resistance on the surface of Ti-6Al-4V alloy in vacuum
   by using a low cost surface treatment known as thermal oxidization method;
2. Uncoverng the optimum counterface to reach the lowest damage on its contact area during the sliding against thermal oxidization treated Ti-6Al-4V;
3. Construction a ball-on-disk tribo-tester in order to perform the wear tests in high vacuum.

Additionally, the wear mechanisms against different counterfaces of 52100 type steel, Ti-6Al-4V, and TO-treated Ti-6Al-4V were given special attention. For comparison, the wear mechanisms and friction of untreated Ti-6Al-4V alloys were examined.

CHAPTER III

CONSTRUCTION AND CALIBRATION of A NEW TRIBOTESTER OPERATING UNDER LOW ATMOSPHERIC PRESSURE

3.1. Introduction

In this work special tribo-tester was constructed to study vacuum tribological behaviour of Ti-6Al-4V and TO-treated Ti-6Al-4V. The tribotester was a pin (ball)-on-disk type tester. The tribotester to operate under the vacuum condition consisted of three major components: ***i***) the wear rig, ***ii***) pumps and piping, ***iii***) the electrical parts. The system included pumps and the piping system, an ion gauge, a pressure indicator, a mechanical feedthrough as well as a bell jar (chamber). These are mounted to the its main frame of the system. All electrical parts of the system were purchased from the different outside suppliers.

This chapter describes the design and construction of the tribo-system. In the last section the calibration and performance of the system will be considered.

3.2. Design and Construction of Tribotester

A wear-testing system was designed. **Table 3.1** lists the major parts of tribo-tester. **Figures C.1-C.4** show the major parts individually (Appendix C). The stationary part of the wear rig is the pin that holds the ball. The ball at the tip of the pin is 6 mm in diameter. However, the size of ball holder can be changed to accommodate counterfaces of various diameters. The applied normal load is exerted directly on sample by means of deadweight placed above the pin. The disk is mounted on an adaptor (disk holder). **Fig 3.1** is a photo that shows the pin-on-disk assembly. **Figure 3.2** is schematic picture of the tribo-tester that shows the individual components of the pin-on-disc assembly. A variable speed electric motor (Servomotor) is directly attached to external part of mechanical feedthrough provides rotation of disc. The Terminal (# 4 in **Fig 3.2**) is connected to strain gauge arm (# 4 in **Fig 3.2**), and eventually to the pivot part (# 2 in **Fig 3.2**)in such a way the arm can move up and down. Before applying the normal force on the sample, the arm

should be levelled. Thus, a counterbalance arm (# 1 in **Fig 3.2**) provided at the back of pivot part. In order to measure frictional force resulting from sliding the ball on the surface of disk, strain gauges are glued on the strain gauge arm. The function of strain gauges shall be explained in section 3.4. The frictional force is viewed on a monitor, and data recorded in computer. The preparation of the pin-in-disk mechanism for operation is described in Appendix.A.

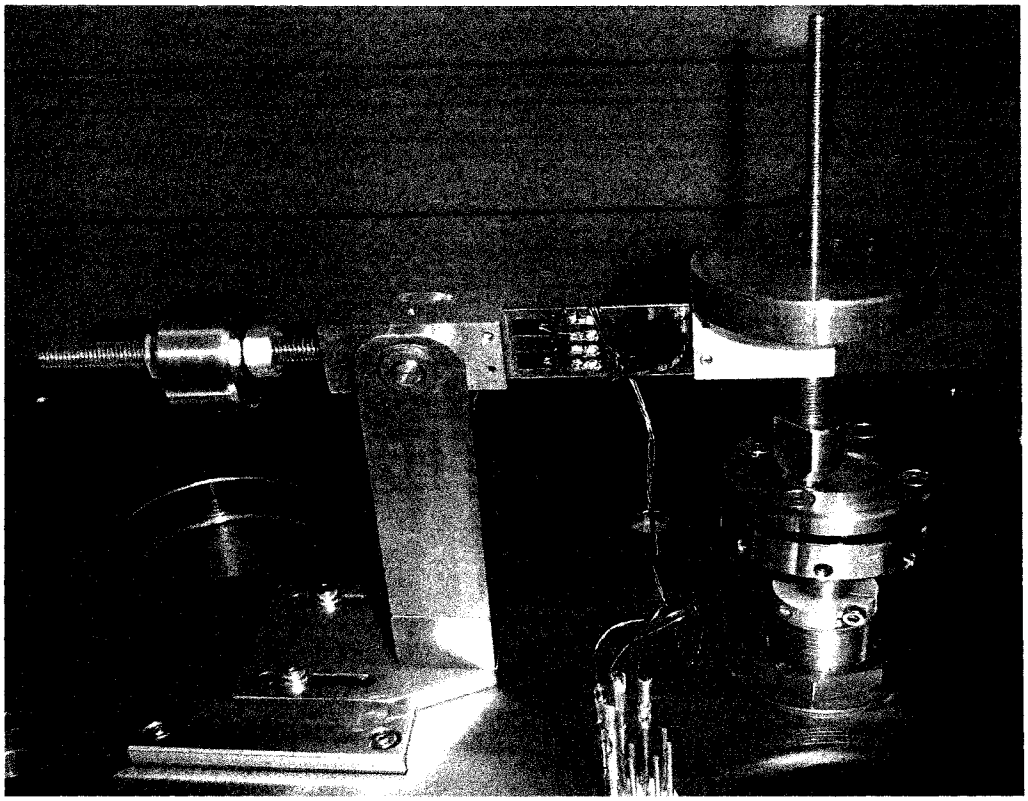

Figure 3.1 Whole tribo-system ready to function.

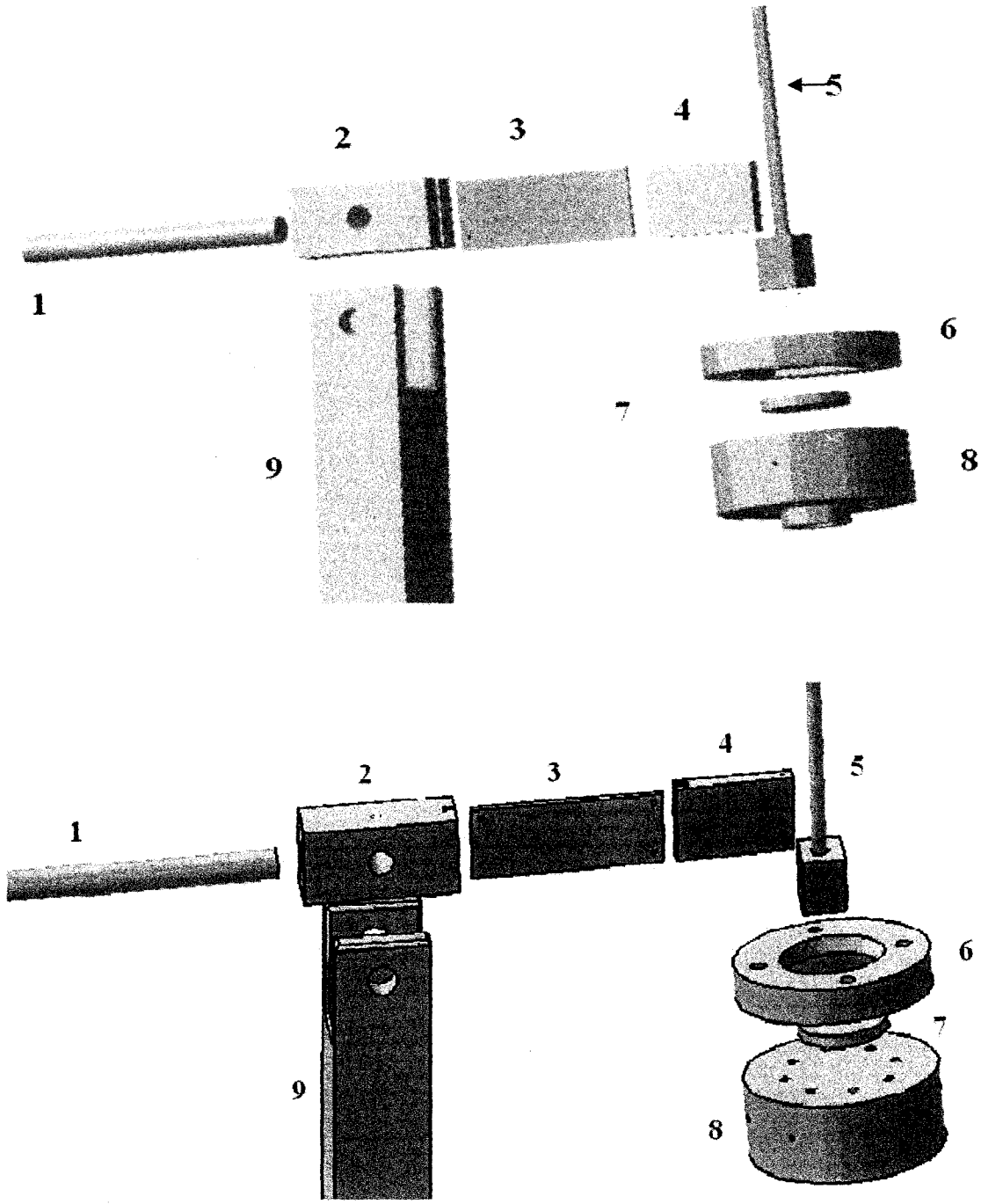

Figure 3.2 Two perspectives of the tribo-tester: 1. Counterbalance arm, 2. Pivot, 3. Strain gauge arm, 4. Terminal, 5. Counterface ball holder, 6. Upper shell of Disk holder, 7. Disk adjustment, 8. Sample (Disk) holder (2,3, and 4 known as Ball-holder arm), 9. Pivot holder. [The drawings were made using Catia V5-14]

Table 3.1 List of the parts used in the tribo-tester parts (all parts are made of 304 grade S.S. - number next to the part match the number on **Fig 3.2**).

Parts	Function
Terminal (4)	**Grips he ball holder. Transfer frictional force to SGA**
Strain Gauge Arm (SGA-3)	**Post for strain gauges, and Bridge between terminal and pivot**
Pivot (2)	**Connection between counterbalance and front part of the wear rig**
Counterbalance Arm (1)	**Levels the tribo-tester's arm**
Pivot Holder (9)	
Upper Shell of Disk Holder (6)	**Keeps the sample in place during the test**
Disk Holder (8)	**Seat for disk**
Ball Holder (5)	**Holds the ball in place, Transfers the normal load directly on the sample**

3.3. Assembly of Mechanical Components

In order to reduce the partial pressure of oxygen in side the chamber, a set of the pumps, valves, and piping are necessary. The vacuum system was designed to provide the low vacuum pressure of 7×10^{-6} torr (9.33×10^{-4} Pa) was provided. **Table 3.2** specifies details of the mechanical components. The mechanical pump reduces the atmospheric pressure of 760 torr to about 10^{-3} torr. Then the diffusion pump becomes operational for further reduction of pressure. The mechanical and diffusion pumps are shown in **Fig 3.3.** Details of the valves are given in **Fig 3.4.**

The steps used to reach the low atmospheric pressure are presented in Appendix B. Lack of a baffle and a cold trap were compensated by purging argon inside the vacuum chamber at the different stages of evacuation. Argon molecules are supposed to

hit and release the trapped air molecules. Therefore, by using flexible hose, a cylinder of argon (99.99%) was connected to a *Needle* valve (V4) (see **Fig 3.4**).

Table 3.2 Specifications of vacuum pumps (all parts are purchased from BOC Edwards).

Parts	Ultimate Vacuum	Model	Function
Diffusion Pump	**10^{-10} torr**	**EO-2**	**Reduces pressure from 10^{-3} to 10^{-6} torr**
Rotary (Mechanical) Vacuum Pump	**75×10^{-5} torr**	**E2M-12**	**Reduces pressure from 760 to 10^{-3} torr**
Foreline Valve	**N/A**	**N/A**	**Passes air flow from diffusion to mechanical pump**
Roughing Valve	**N/A**	**N/A**	**Passes air flow from chamber to mechanical Pump**
High vacuum Valve	**N/A**	**N/A**	**Passes air flow from the chamber to diffusion pump**
Vent (Relief) Valve	**N/A**	**N/A**	**Allows the air flow to the chamber**

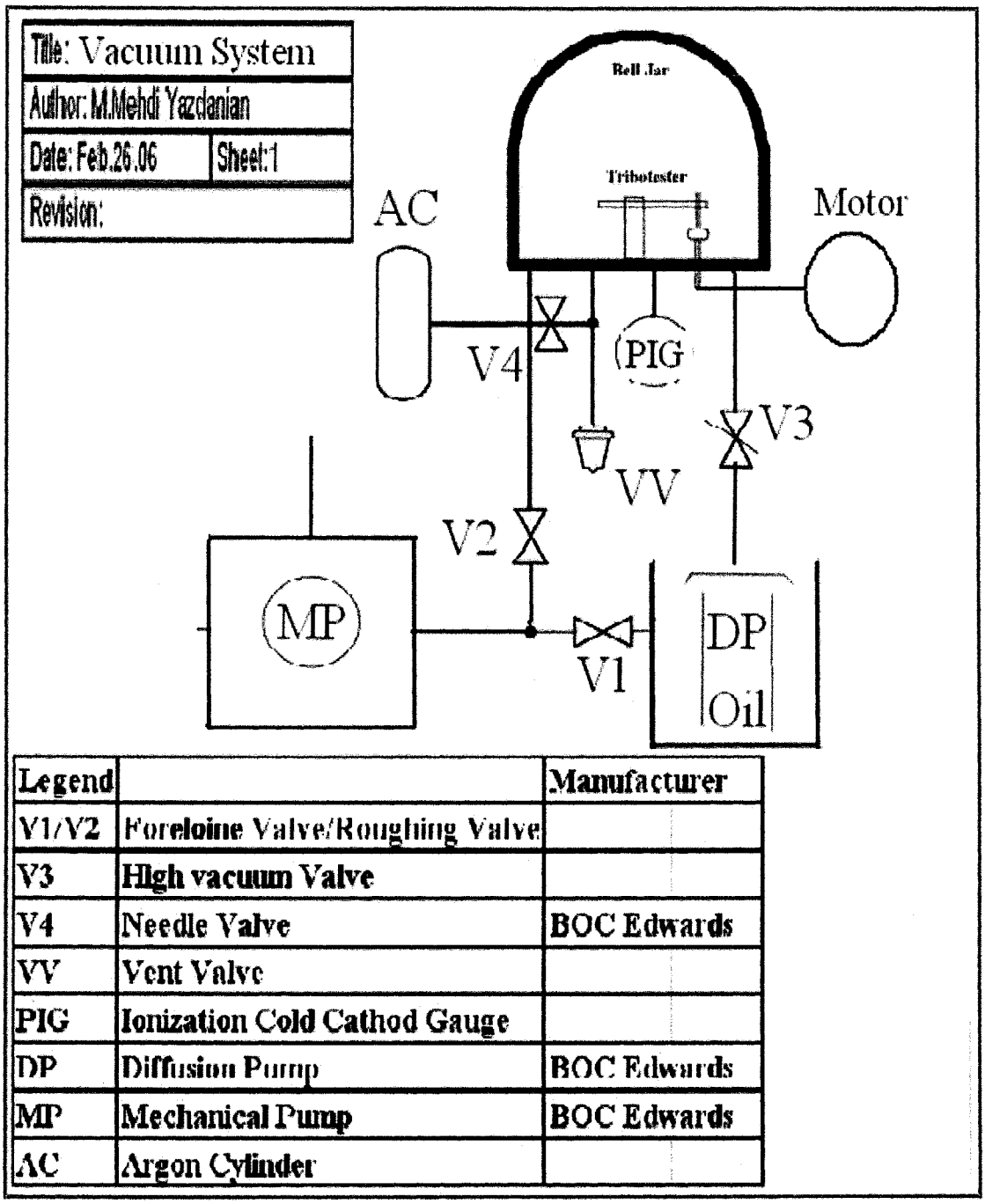

Legend		Manufacturer
V1/V2	Foreloine Valve/Roughing Valve	
V3	High vacuum Valve	
V4	Needle Valve	BOC Edwards
VV	Vent Valve	
PIG	Ionization Cold Cathod Gauge	
DP	Diffusion Pump	BOC Edwards
MP	Mechanical Pump	BOC Edwards
AC	Argon Cylinder	

Figure 3.3 Schematic picture of evacuation system using piping and instrument standard diagram.

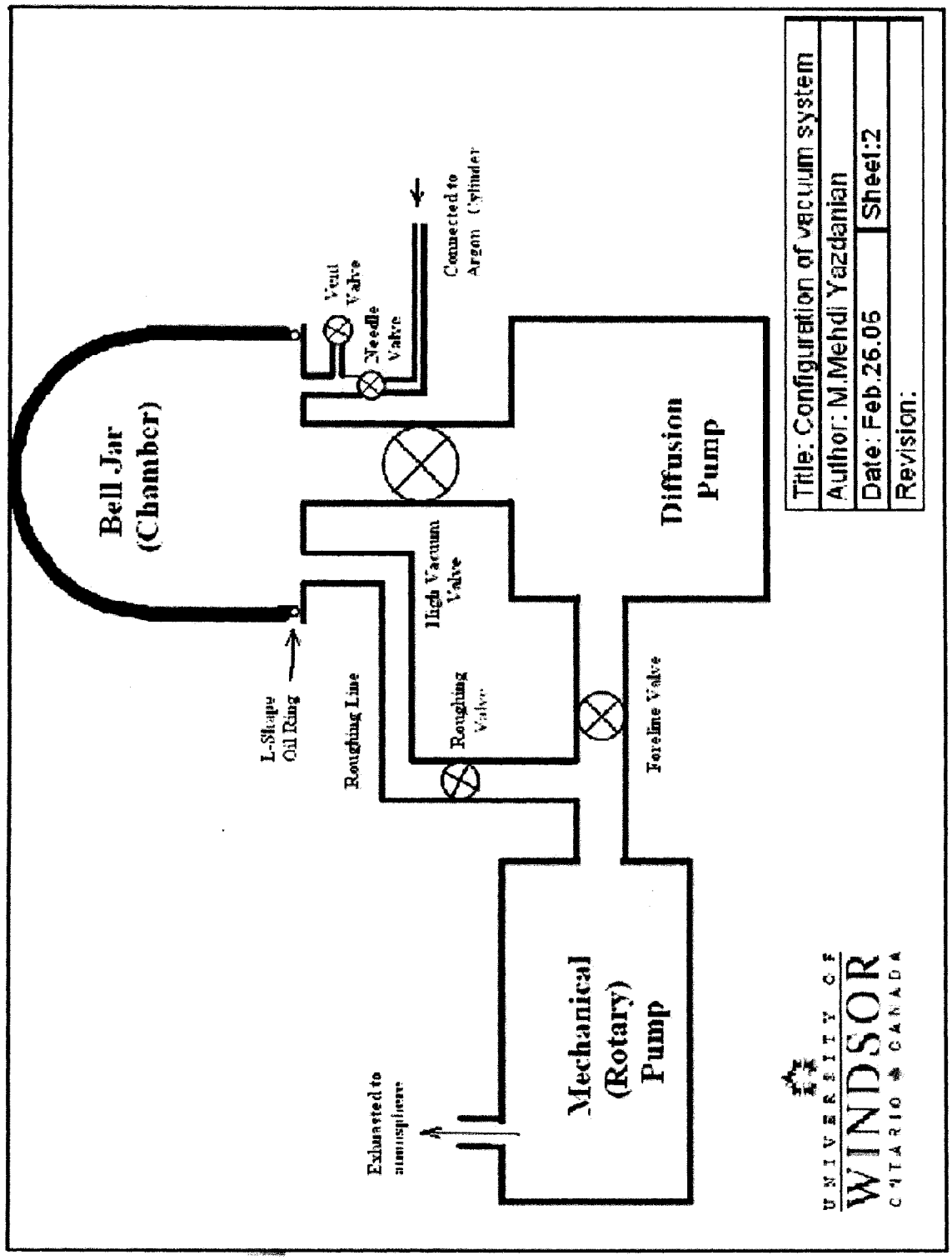

Figure 3.4 Schematic picture of vacuum system.

3.4. Electrical Instrumentations

3.4.1 The Servomotor

A servomotor has been fixed to the rotary shaft by means of a mechanical feedthrough. The servomotor has been selected based on its high torque and power rating. Considering that of total 20 N normal load is applied to the disk. The rotation speed of rotary shaft feedthrough was determined as 0.031 N.m. The weight of this mechanical feedthrough is supported by a blanking plug and flange mounted to the base of the vacuum chamber (**Fig 3.5**). A maximum sliding velocity of 0.5 m/s was considered for disk holder (sample stage). The time for the servomotor to reach this velocity should not exceed one second. The following calculations have been done to determine the torque of motor:

$$\tau_1 = \tau_{motor} - \tau_2 - \tau_3 \qquad \textbf{(3-1)}$$

where τ_1 is the net torque of the rotational disk, and τ_2 is the torque applied as a result of normal force on the disk, which comes from dead weight, and τ_3 is initial torque for rotary shaft feedthrough. The net torque of the rotational disk is determined by following equation:

$$\tau_1 = \frac{1}{2} m R^2 \frac{\Delta \omega}{\Delta t} \qquad \textbf{(3-2)}$$

where m is the mass of the disk holder, R is radius of the disk, ω is angular velocity of disk and t is the time that servomotor and therefore disk reach to the specific sliding velocity. The following relationship gives the necessary torque to the applied due to normal force on the disk:

$$\tau_2 = \mu F R \qquad \textbf{(3-3)}$$

where F is normal load applied on the disk, R is radius of disk, and μ is coefficient of friction between ball and disk. With all mentioned, the torque for motor is:

$$\tau_{motor} = (1/2 \times .25kg \times 0.025m^2 \times \frac{0.5}{0.01} s^{-1} \times \frac{1}{1} s^{-1}) + (2 \times 20N \times 0.01m) + 0.031N.m$$

$$\tau_{motor} = 0.435N.m$$

With a safety factor of 2, the final torque was 0.87 N.m. **Table 3.3** illustrates the specification of servomotor and all the electrical parts used. Signals from the strain gauge

were transferred to the data acquisition system, and then to a computer to record and convert the frictional force to the coefficient of friction.

Table 3.3 Electrical parts.

Electrical instrument	Model	Manufacturer
Servomotor	AKM23D-AnCNC-00	Danaher Motion (kollmorgen)
Electrical Feedthrough	10 pin power NPT (high vacuum)	MPF products Inc.
Strain Gauge (for Steel)	SG-3E350- LY47	Omega
Adhesive Kit (glue for Strain Gauge)	M-Bond 43B-1	INTERTchnology Inc.
Data Acquisition Card	DT 9800 Series	Data Translation
Brushless Servo Drive	S200 Series	Danaher Motion (kollmorgen)

3.4.2 Recording Frictional Force

The strain gauge should measure extremely small changes in resistance with high accuracy. Such demanding precision calls for a bridge measurement circuit. In the current mechanism, four active strain gauge elements are used. This system is highly sensitive to bending strain, e. g. bending strain gauge arm, and it rejects axial strain. The general relationship for calculation of output voltage is:

$$V_{out} = V_{in}\left[\frac{R_3}{R_3 + R_4} - \frac{R_2}{R_1 + R_2}\right] \quad \textbf{(3-4)}$$

where all the resistances (R_n) represent the strain gauges (negative or positive) glued on the strain gauge arm. **Figure 3.6** displays the electrical circuit of tribo-tester.

3.5. Calibration of Tribo-tester

3.5.1 Calibration of Frictional Force at Room Temperature

By means of a program purchased from Data Translation Co. (Scope), the received signals by Data Acquisition System were converted to frictional force.

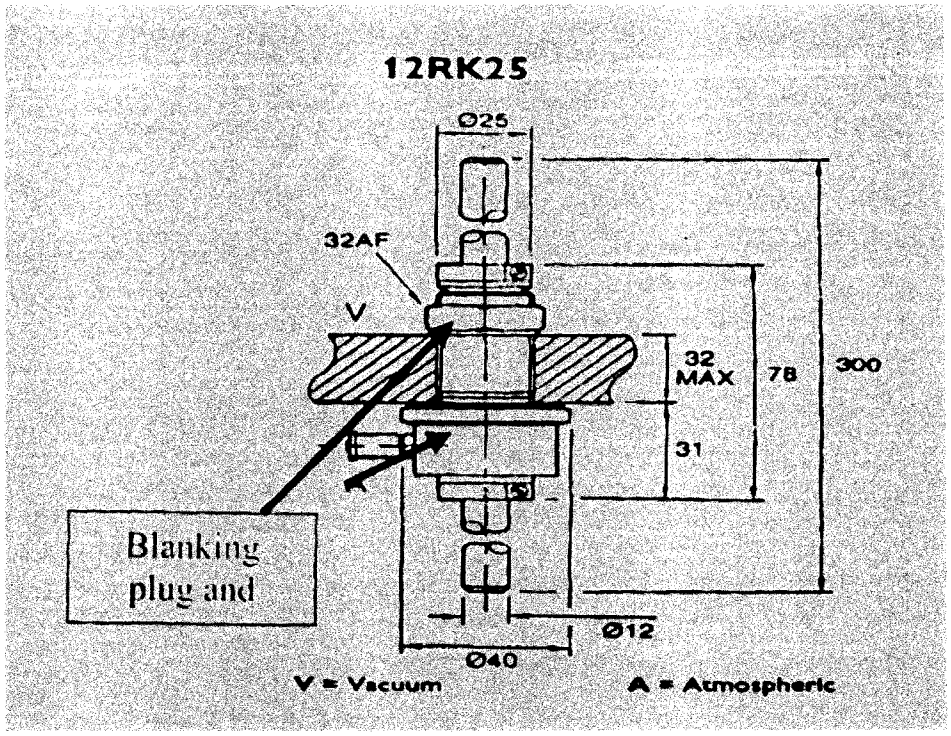

Figure 3.5 The schematic of rotary shaft (feedthrough). The blanking plug helps sealing the mechanisms while shaft rotates.

Then, this force is divided by the normal force to determine the coefficient of friction (COF). To be certain about the magnitude of frictional force, the results were compared to the data obtained from a high temperature tribo-tester, which is a system made by CSM Instruments Co.

Samples of commercial purity Al 1100, and as received (annealed) Ti-6Al-4V were selected as samples in a shape of a disk with diameter of 2.45 cm. The Al 1100 sample was wet ground using 240, 600 and 1200 grit SiC emery papers successively. After this stage, samples were polished using 3 μm and 1 μm diamond suspensions successively. The preparation of Ti-alloy samples will be mentioned in the next chapter. The 52100 steel balls were used as counterfaces for all the tests. All balls and disks were immersed in Acetone for 5 min and washed in the ultrasonic bath of ethanol for 30~45 seconds. The tests were conducted at a normal load of 2 N and sliding velocity of 0.05 m/s in ambient air. The COF diagrams showing the variation of COF with the time for 52100 Steel on Al 1100 and 52100 Steel on Ti-6Al-4V alloy roughly indicate the same trends (**Fig 3.7** and **3.8**). The results were in agreement with those obtained from commercial CSM system.

3.5.2 Coefficient of Friction in Low Atmospheric Pressures

The COF versus sliding distance in vacuum i.e. at 5×10^{-5} torr for the tribo couple consisting of a 52100 steel ball with diameter of 64 mm run against a disk of Al 1100 was studied by Lepper, K. et al. [65]. The normal loads between 8 and 10 N and the sliding velocities of 0.015~0.03 m/s were applied during the tests. However, the test performed here were different. The same atmospheric condition with a lower normal load of 4 N and higher sliding velocity of 0.05 m/s were considered. As for Lepper's result, the COF began around 0.8 and dropped drastically to around 0.3. After 100 meters of sliding, the COF came to the steady condition (**Fig 3.9**). The steady state for higher normal load was about 0.2, and in our case this value was around 0.3. Still the same trend encountered for both tests. So it was concluded that the vacuum tribo-tester's measurement system was satisfactory.

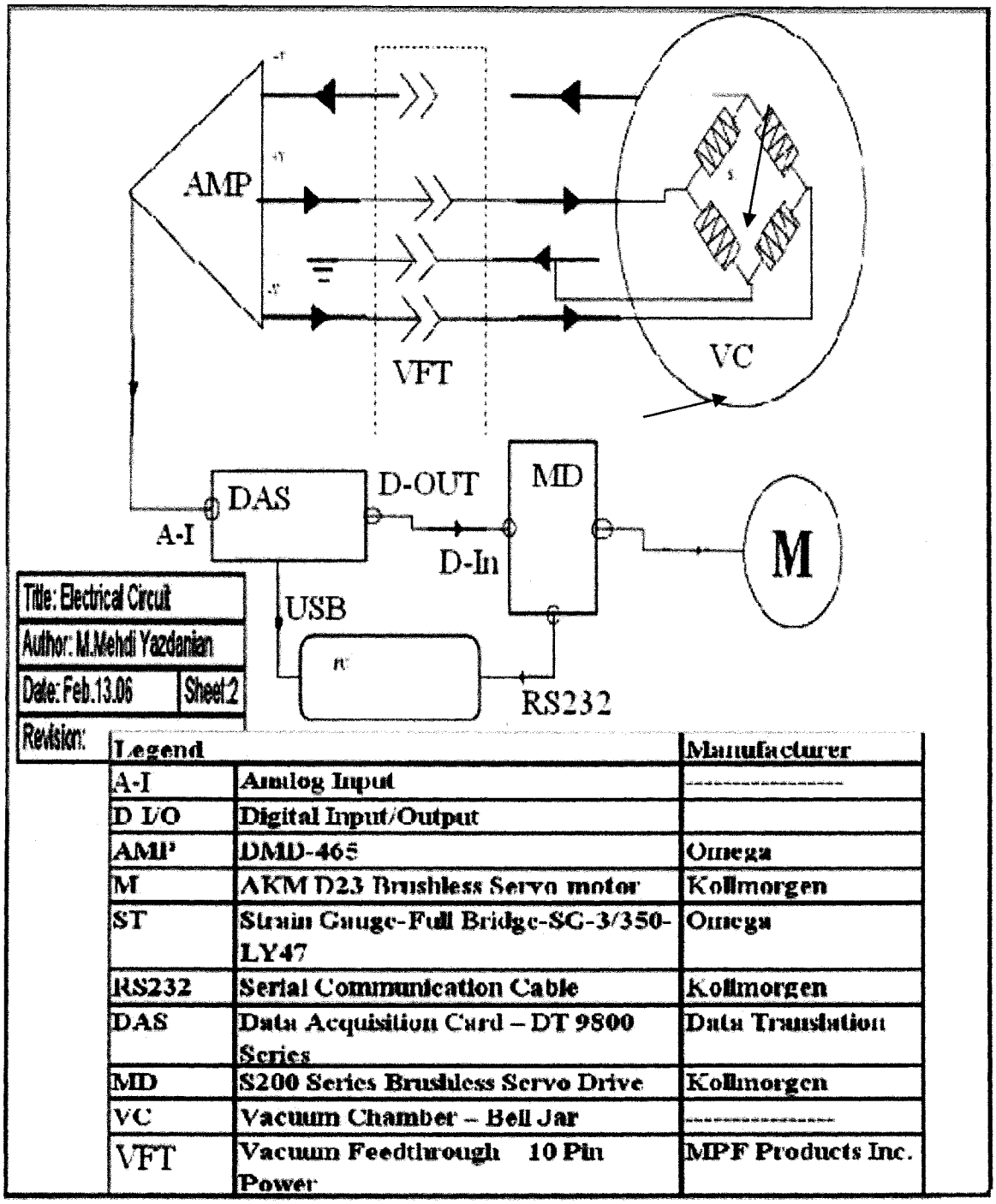

Legend		Manufacturer
A-I	Analog Input	----------
D I/O	Digital Input/Output	
AMP	DMD-465	Omega
M	AKM D23 Brushless Servo motor	Kollmorgen
ST	Strain Gauge-Full Bridge-SG-3/350-LY47	Omega
RS232	Serial Communication Cable	Kollmorgen
DAS	Data Acquisition Card – DT 9800 Series	Data Translation
MD	S200 Series Brushless Servo Drive	Kollmorgen
VC	Vacuum Chamber – Bell Jar	----------
VFT	Vacuum Feedthrough 10 Pin Power	MPF Products Inc.

Figure 3.6 Electrical circuit of tribo-tester.

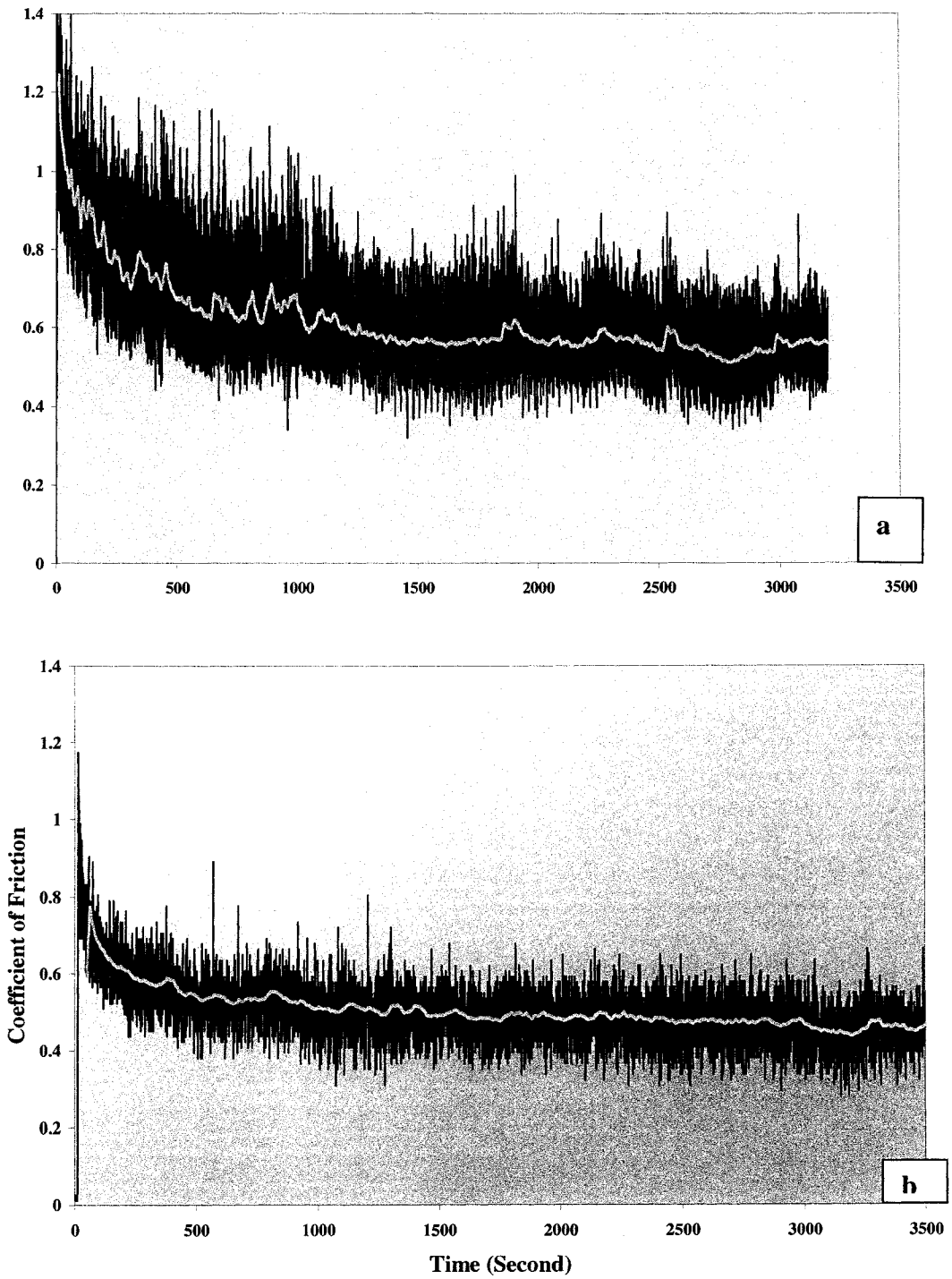

Figure 3.7 (a) Coefficient of friction obtained from a commercial pin/ball (52100 steel)-on-disk (Ti-6Al-4V alloy) system, (b) Coefficient of friction obtained from a tribo-tester of pin/ball (52100 steel)-on-disk (Ti-6Al-4V alloy) designed and built in-house (in ambient air).

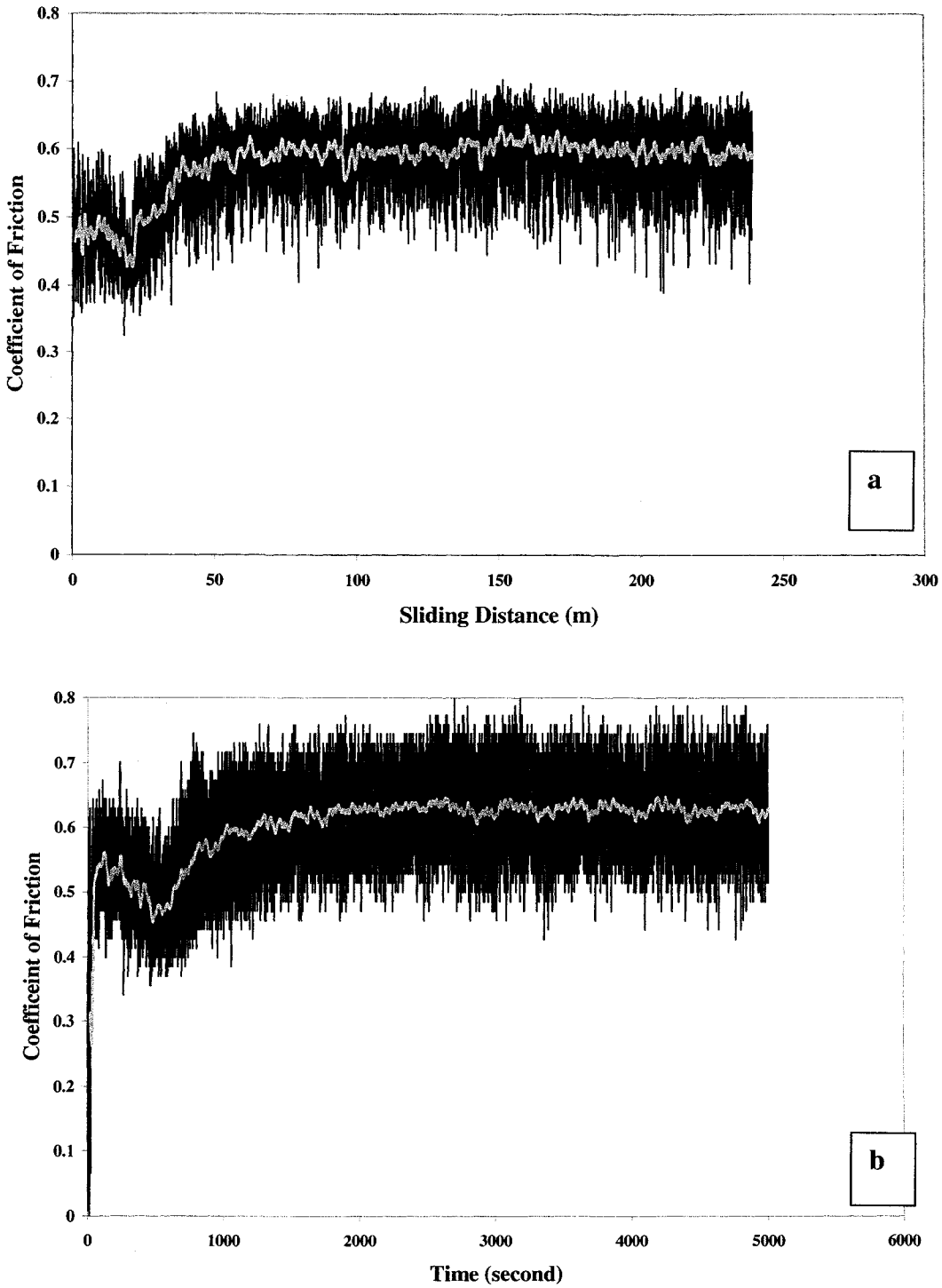

Figure 3.8 (a) Coefficient of friction obtained from a commercial pin/ball (52100 steel)-on-disk (Ti-6Al-4V alloy) system, (b) coefficient of friction obtained from tribo-tester of pin/ball (52100 steel)-on-disk (Ti-6Al-4V alloy) designed and built in-house (in ambient air).

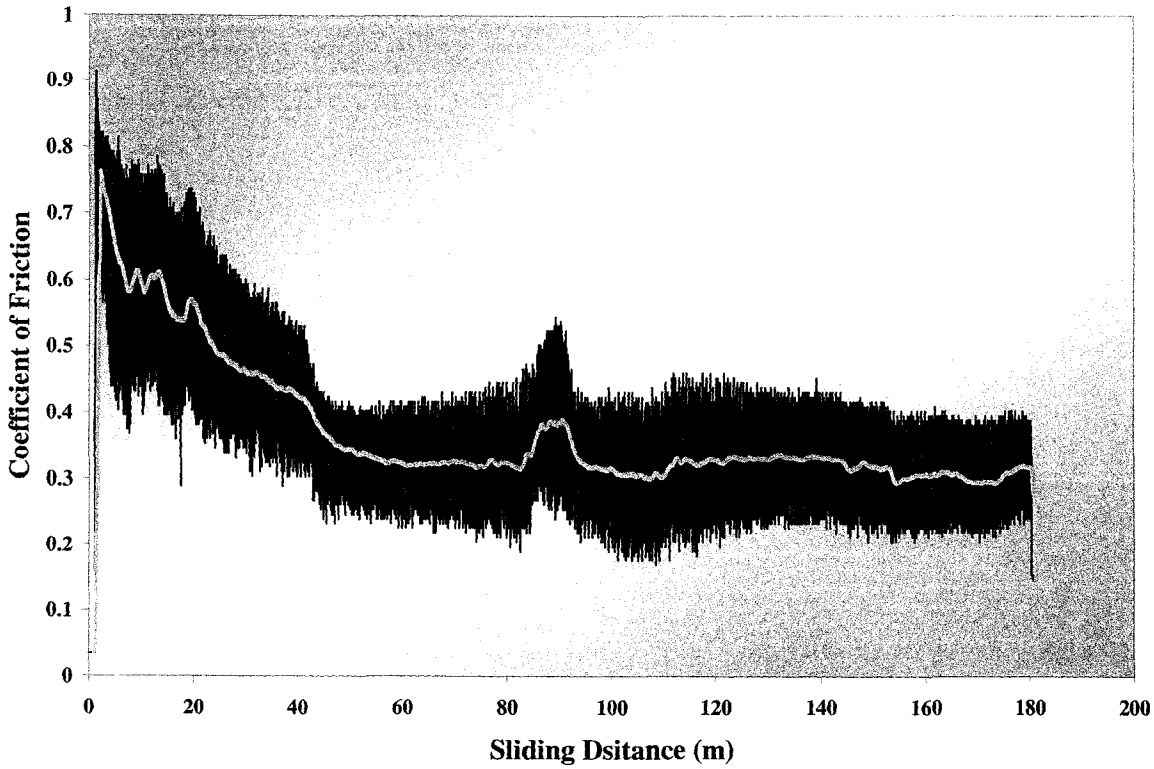

Figure 3.9 The performance of new tribo-tester in form of ball (52100 steel)-on-disk (Al 1100) in vacuum condition: COF obtained from the tribo-tester designed and built in-house.

CHAPTER IV

MATERIALS AND EXPERIMENTAL PROCEDURES

4.1. Material Used

An annealed Ti-6Al-4V alloy in the shape of a rod with diameter of 25 mm and length of 200 mm, and of Ti-6Al-4V alloy balls of 6 mm diameter were purchased from the supplier Goodfellow. The rod was cut into 5 mm thick pieces. The pieces were used in the experiments. The counterfaces were 52100 steel balls and annealed Ti-6Al-4V alloy balls of 6 mm diameter.

4.2. Microstructures of the Ti-6Al-4V alloy

For microstructural examinations, the samples (disks) were wet ground using 240, 400, 600, 1200, and 2400 grit SiC emery papers successively. After the grinding, samples were polished using 6 μm and 1 μm diamond suspensions in a row. The etching was performed by immersing the sample into a solution that consisted of 6 ml HNO_3, 2 ml HF, and 62 ml H_2O, for 15 to 20 seconds. The optical microscopy images from the etched surfaces show two main phases of this type of Ti-alloy. The α-phase is the phase in the brighter area, while roughly 30% of the alloy consisted of the β-phase (**Fig 4.1**).

4.3. Sample Preparation

The same method of grinding and polishing as explained in section 4.2 was applied for disks. Before each wear test, counterface balls and disks shaped samples were cleansed about 5 minutes by Acetone, and washed in an ultrasonic bath of Ethanol for 30~45 seconds.

4.4. Thermal Oxidization of Ti-6Al-4V Alloy

The samples, which are needed to be thermally oxidized before the sliding tests, and after polishing and cleansing, were thermally oxidized inside a muffle furnace at 600°C for 60 hours. These samples are referred as TO-treated Ti-6Al-4V in this thesis.

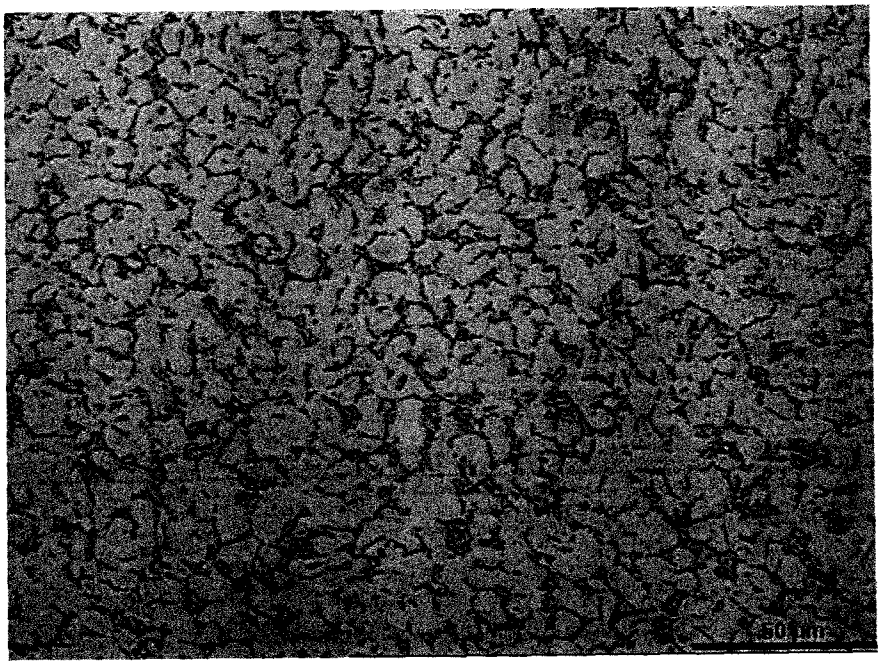

Figure 4.1 An optical micrograph of the microstructure of as received (annealed) Ti-6Al-4V alloy. The darker areas illustrate the β-phase of titanium and the brighter regions are the α-phase.

4.5. Experimental Procedures

The surface roughnesses of samples were measured using a optical surface profilometer before and after wear test. Micro-hardness tests determined the harnesses of the unexposed surfaces of samples. A WYKO 1100 optical surface profilometer was used to obtain the surface roughness of the wear tracks. Wear tests were performed using a ball-on-disk tribo-tester built in-house as explained in Chapter.3. The atmospheric condition during the wear tests were either the ambient air or a high vacuum of 7×10^{-6} torr. The normal force, sliding velocity, and sliding distance were 2 N, 0.05 m/s, and 250 m respectively. These parameters kept constant for all tests. In order to characterize microstructures and morphologies of the worn surfaces and debris a scanning electron microscope (SEM-Jeol 5400 LV), an X-ray diffraction system (XRD) and Energy Dispersive X-ray Spectroscopy (EDS) were used. The EDS was performed inside an environmental scanning electronic microscopy (ESEM-FES 200).

4.6. Measurements of Wear Rate and Mass Loss from the Samples

4.6.1 Wear Rate Measurements

All the balls and disks were weighted using an analytical scale with an accuracy of 0.1 mg before and after the wear tests. For the untreated samples, the mass loss (M) was divided by the density (ρ) of Ti-6Al-4V (4.5 g/cm^3). In case of thermally oxidized samples, the weight losses were divided by the density of titanium dioxide (TiO_2), which is 4.26 g/cm^3. To attain the wear rate, the volumetric wear loss values results were divided by the sliding distance (250 m).

Alternative way of measuring the wear rates is to apply the volume wear loss equation [1]. The volumetric wear loss (V) can be determined according to the ASTM Standard G99:

$$V = 2\pi R_d \left[r^2 \sin^{-1}\left(\frac{w}{2r}\right) - \left(\frac{w}{4}\right)\sqrt{4r^2 - w^2} \right] \qquad \textbf{(4-1)}$$

where R_d and w are the radius and the width of the wear track, and r is the radius of the ball. Then the volume losses were divided by the sliding distance to obtain the wear rate. The volumetric wear loss in this thesis called as volumetric wear damage.

4.6.2 Mass Loss Measurements of the Counterfaces

The counterface balls showed very little mass loss or gain. This mass loss or gain was determined using the analytic balance before and after the wear tests.

4.7. X-ray Diffraction Results from Untreated and TO-treated Ti-6Al-4V

To detect the phases formed on the surface of thermally oxidized samples X-ray diffractometry (XRD) was performed. The comparison of the results from TO-treated samples and untreated samples exhibit presence of titanium dioxide in form of rutile and anatase in addition to the α and β-phases in the untreated Ti-6Al-4V alloy (**Fig 4.2 & 4.3**). The thickness of oxidized layer on the from thermally oxidized samples was 3.5-4 μm (**Fig 4.4**).

4.8. Surface Roughness of Untreated and TO-treated Ti-6Al-4V Alloy

Polished samples had a sooth surfaces prior to the tests. However, oxidization increased the roughness of the surfaces. 3D-WYKO images from the untreated and oxidized Ti-alloy displayed the roughness of samples (**Fig 4.5**). **Table 4.1** shows the surface roughness of samples (disks) before the wear tests.

4.9. Hardness of Untreated and TO-treated Ti-4Al-4V Samples

Knoop hardness test was conducted on polished and treated samples. The results are illustrated on **Fig 4.6** and **Fig 4.7**. The increase of the hardness of the TO-treated sample is due to formation of a hard layer of TiO_2 on the surface. The SEM micrograph images showed dark and light regions on the TO-treated samples. The hardness of the darker area is much higher than the rest. This high hardness is because of more defused oxygen on the surface and higher thickness of oxide layer (**Fig 4.8**).

Table 4.1 Description of surface roughness of samples prior to wear tests using different counterfaces and under different atmospheric conditions.

Sample (disk)	Counterface (Ball)	Atmospheric Condition	Surface Roughness (μm)
Ti-6Al-4V	52100 Steel	Ambient Air	0.024
Ti-6Al-4V	52100 Steel	Vacuum (7×10^{-6} torr)	0.058
TO-treated Ti-6Al-4V	52100 Steel	Ambient Air	0.156
TO-treated Ti-6Al-4V	52100 Steel	Vacuum (7×10^{-6} torr)	0.161
Ti-6Al-4V	Ti-6Al-4V	Ambient Air	0.039
Ti-6Al-4V	Ti-6Al-4V	Vacuum of (7×10^{-6} torr)	0.026
TO-treated Ti-6Al-4V	TO-treated Ti-6Al-4V	Ambient Air	0.103
TO-treated Ti-6Al-4V	TO-treated Ti-6Al-4V	Vacuum (7×10^{-6} torr)	0.161

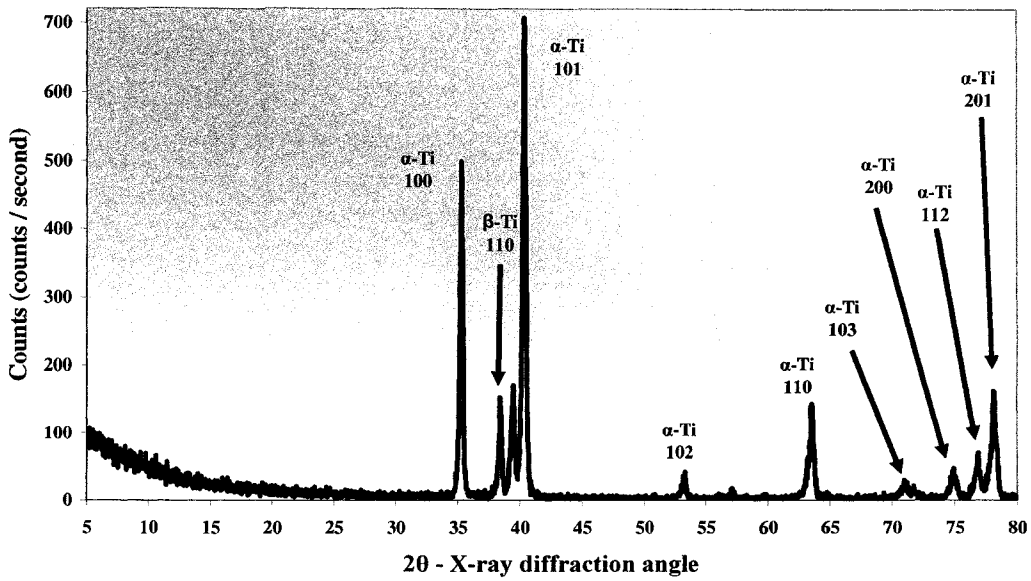

Figure 4.2 The XRD spectra of surface of untreated Ti-6Al-4V sample. The figure demonstrates the peaks for α-Ti and a few small peaks of β-Ti.

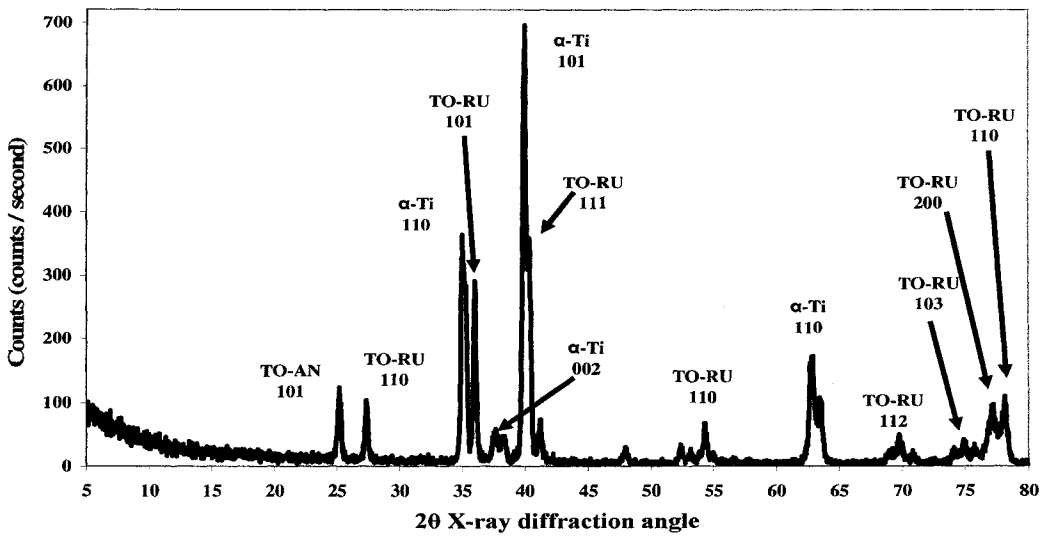

Figure 4.3 The XRD spectra of surface of TO-treated Ti-6Al-4V sample at 600 °C and for 60 hours. The figure demonstrates the peaks for Rutile (Ru) and α-Ti and a few small peaks of Anatase (An).

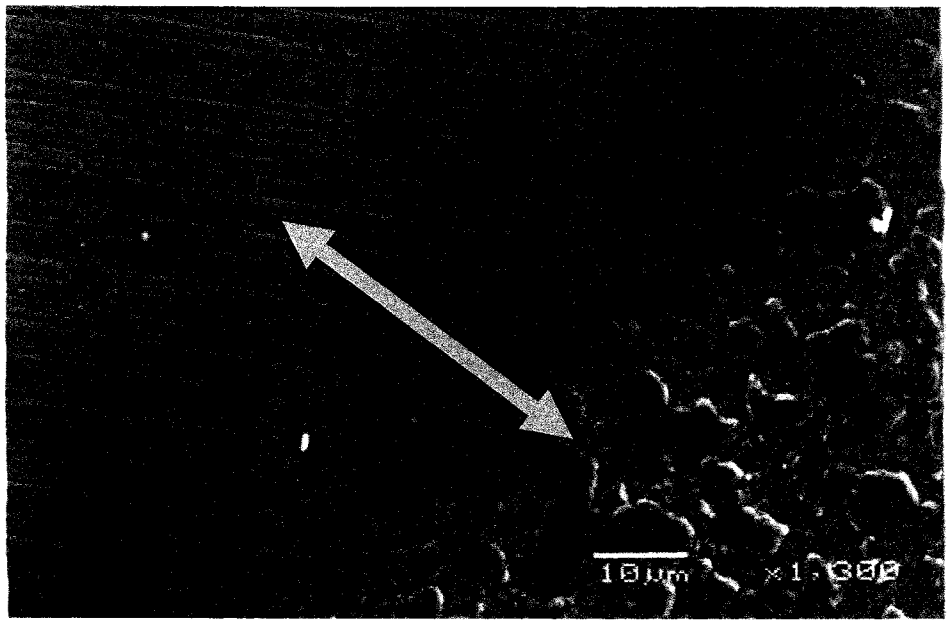

Figure 4.4 SEM micrographs of the thickness of oxidized layer (roughly shown by arrow) of TO-treated Ti-6Al-4V alloy after baking the sample inside the furnace at 600 °C for 60 hr.

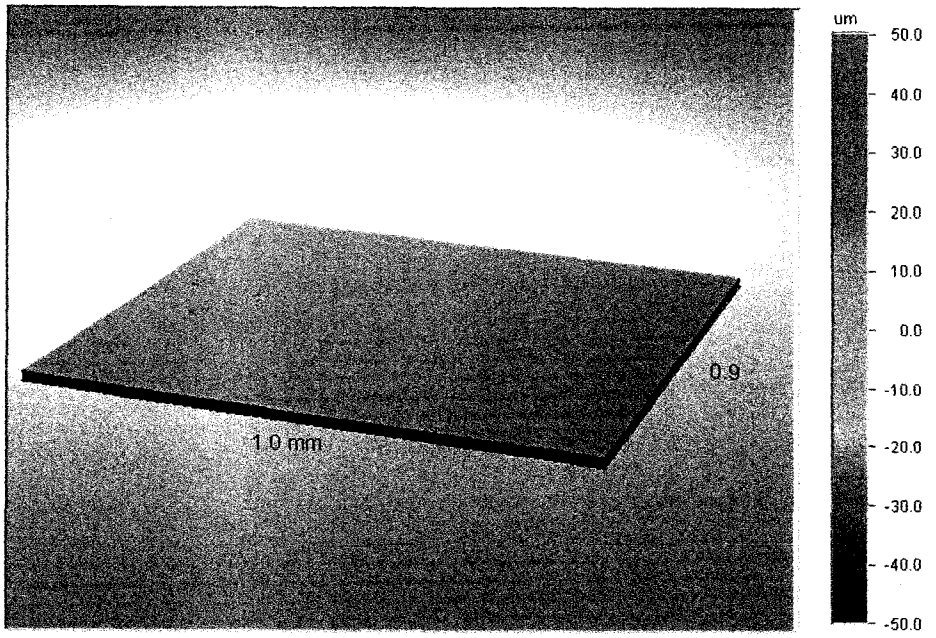

(a)

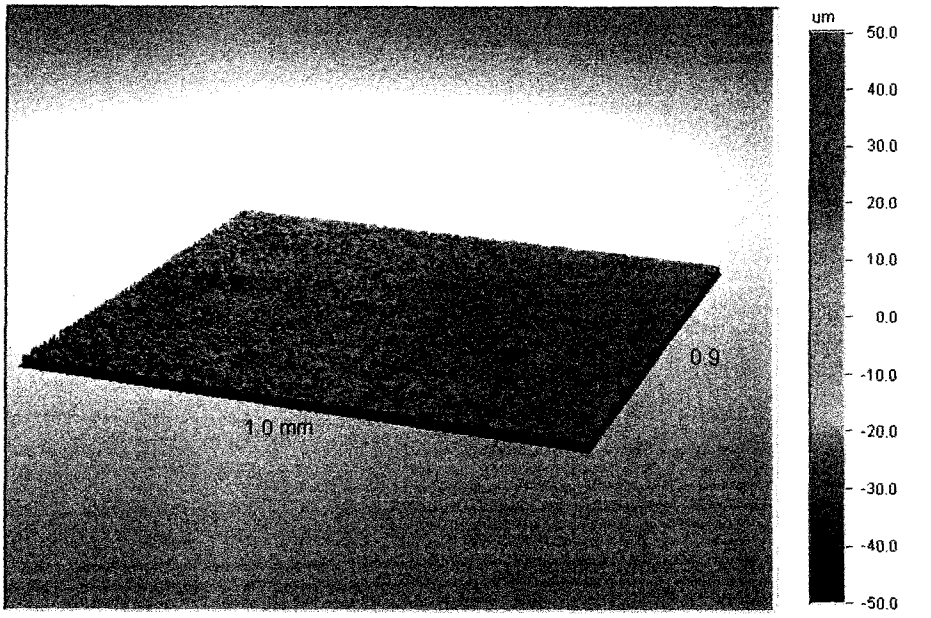

(b)

Figure 4.5 (a) WYKO image from the unworn surface of untreated Ti-6Al-4V alloy before test in vacuum, (b) WYKO image of TO-treated Ti-6Al-4V sample before test in vacuum.

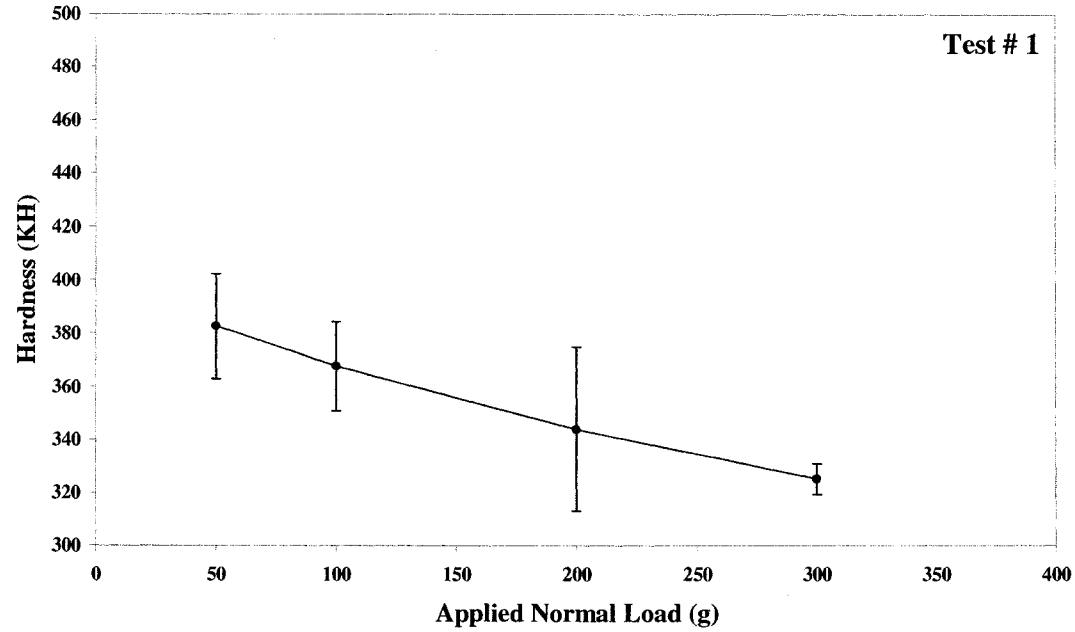

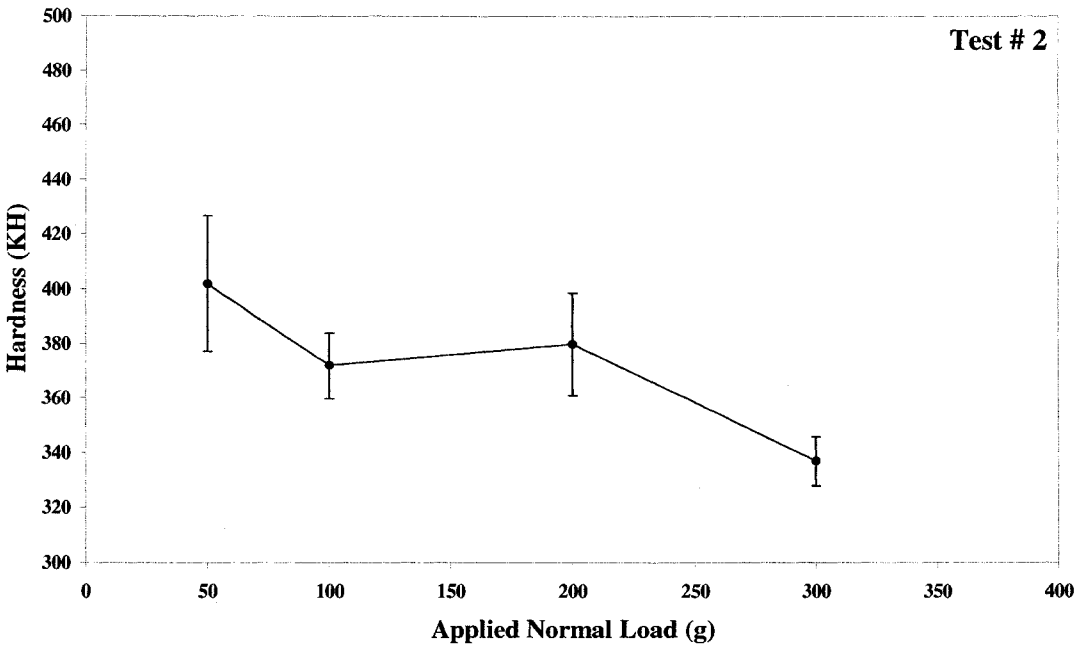

Figure 4.6 Knoop hardness test result on two polished samples - 10 tests were performed at each indentation load.

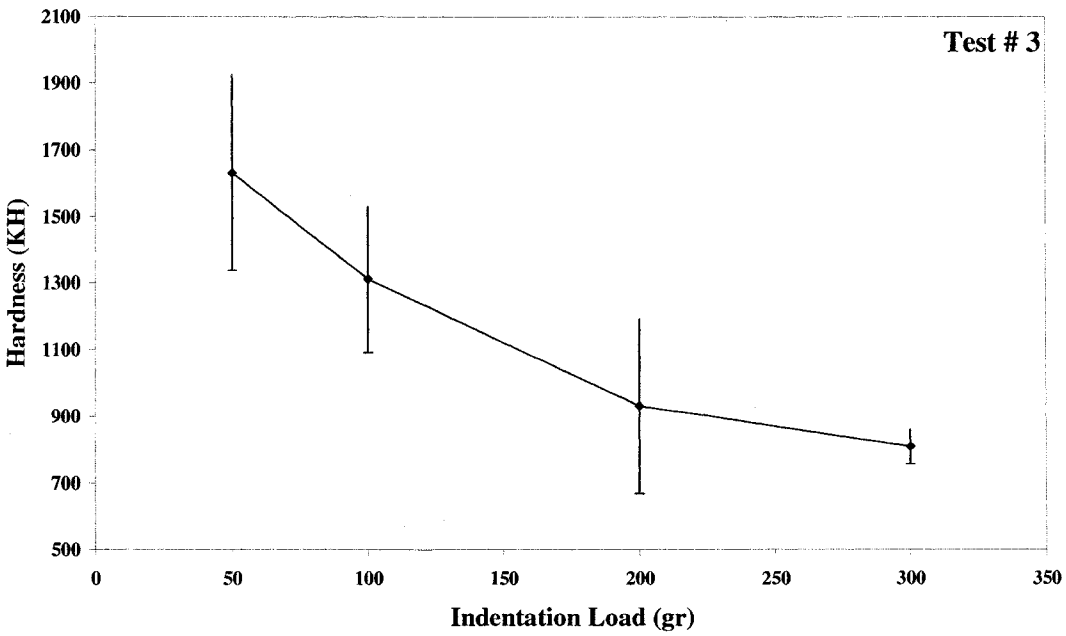

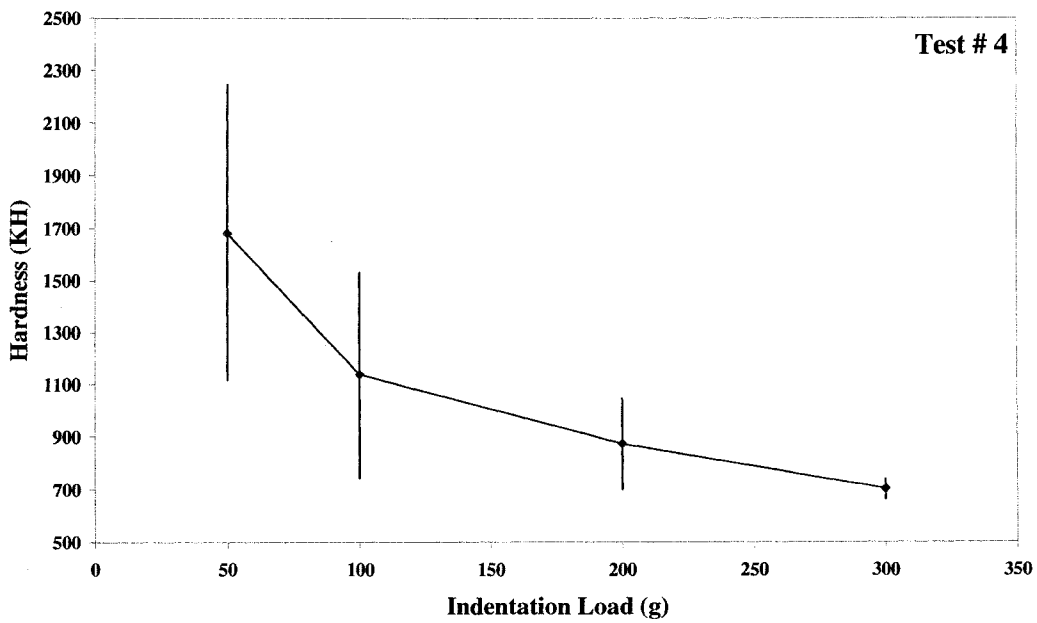

Figure 4.7 The result of Knoop hardness test on two TO-treated Ti-6Al-4V alloys at 600 °C for 60 hr - 10 tests were performed at each indentation load.

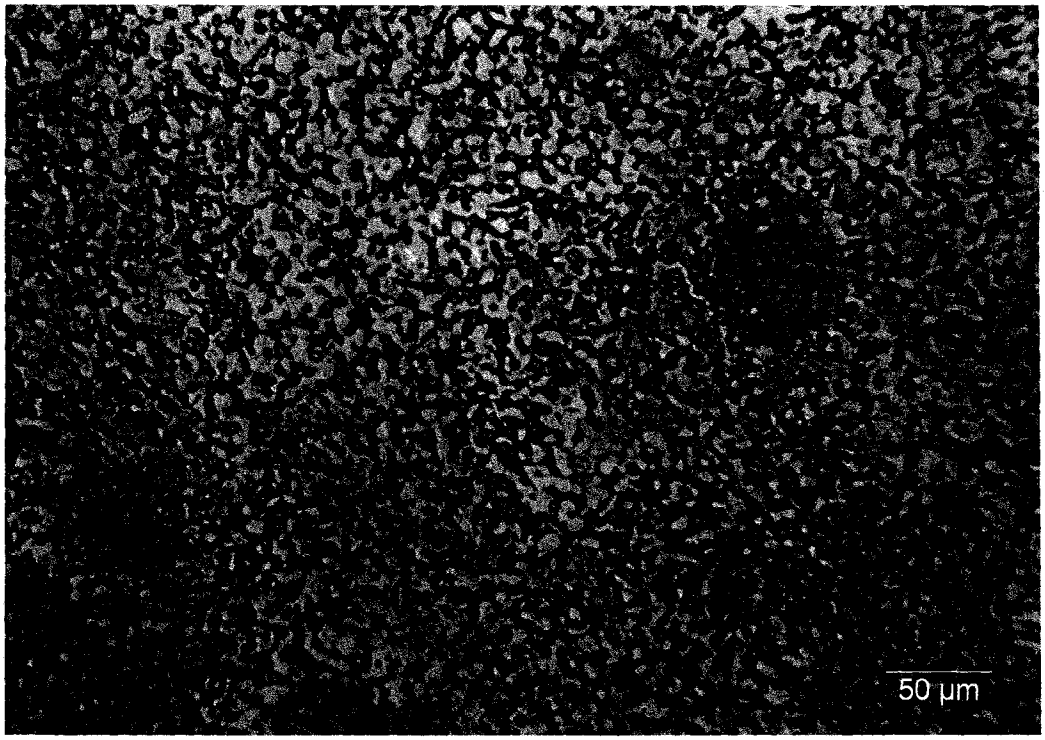

Figure 4.8 The optical picture of the surface of Ti-6Al-4V alloy oxidized in the furnace for 60 hr at 600 °C. The darker area have a typical Knoop hardness number up to 2500 KH while the lighter area has a mean Knoop hardness number of 1500 KH.

CHAPTER V

RESULTS

5.1 Wear Rates

5.1.1 Wear Rates of Untreated and Thermally Oxidized Ti-6Al-4V Alloy

The volumetric wear rates varied due to atmospheric conditions and contact surfaces. It was noted that the highest volumetric wear damage occurred for Ti-6Al-4V alloy worn by Ti-6Al-4V alloy counterface in ambient air whereas the lowest one occurred during sliding of TO-treated Ti-6Al-4V alloy against itself in vacuum (7×10^{-6} torr). **Fig 5.1** displays all the volumetric wear damages (mm^3/m) for all the tests. The wear rates obtained from data of volumetric wear rate (mm^3/m) presented in **Fig 5.2**. In **Fig 5.3,** the wear rates determined using analytic scale for measuring mass loss of samples. In later method, the analytic scale was not sensitive enough to measure the mass loss or gain for thermal oxidization Ti-6Al-4V alloy worn by 52100 steel in vacuum and for sample of Ti-6Al-4V alloy worn by Ti-6Al-4V alloy counterface, in ambient air.

5.1.2 Mass Loss from the Counterfaces

The 52100 steel counterfaces lost mass in tow cases. However, the analytic scale was not sensitive enough to measure the mass loss or gain for most counterfaces. The 52100 steel counterface slid on the untreated sample experienced the highest weight loss of 0.004±0.0002 g in ambient air and 0.006±0.0002 g in vacuum. The weight loss for the rest of the counterfaces was negligible.

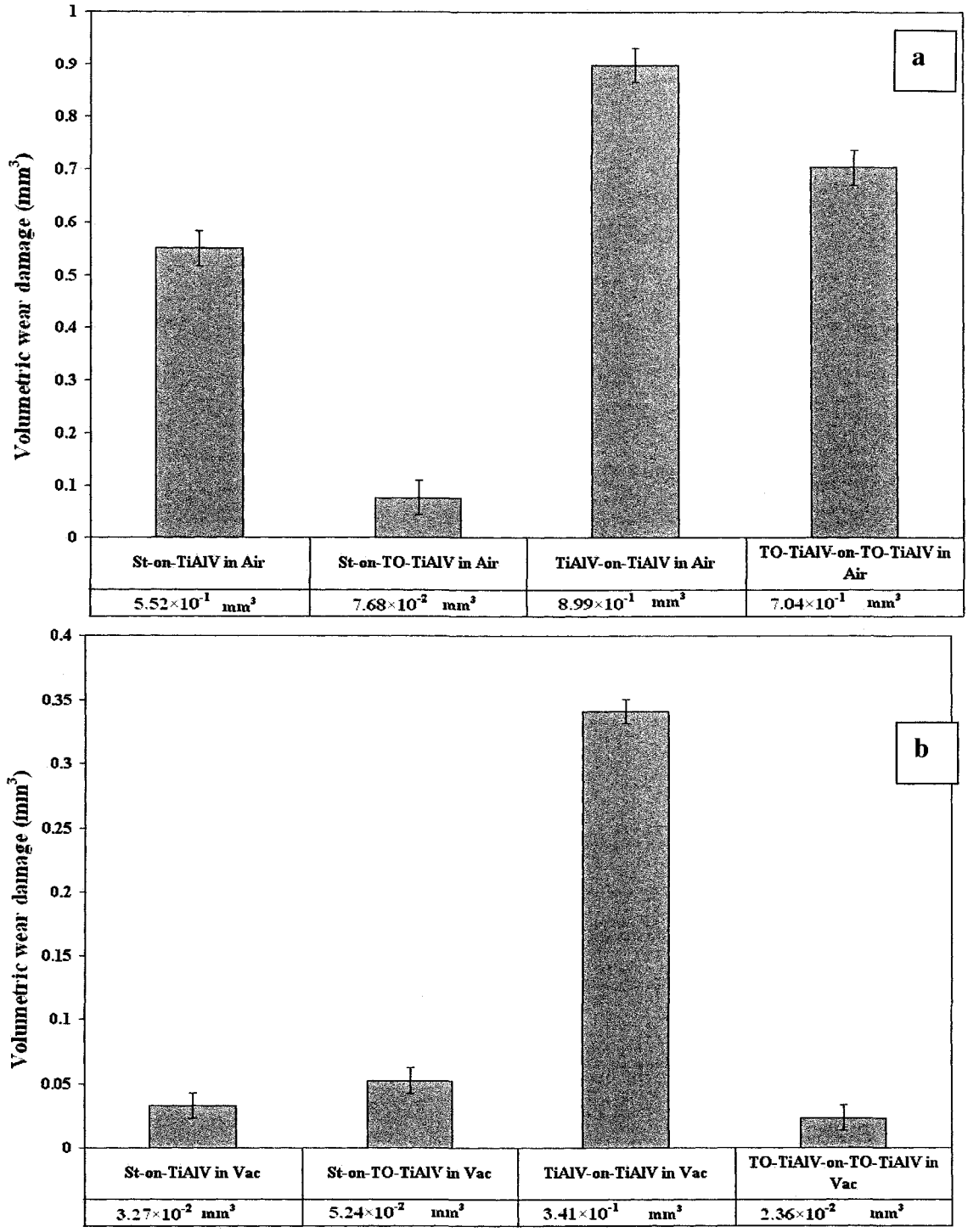

Figure 5.1 Volumetric wear damage for samples in (a) ambient air, (b) high vacuum. Error bar are presented for each result [St: 52100 steel, TO-TiAlV: TO-treated Ti-6Al-4V alloy, TiAlV: Untreated Ti-6Al-4V alloy, Air: Ambient air, and Vac: Vacuum of 7×10^{-6} torr]

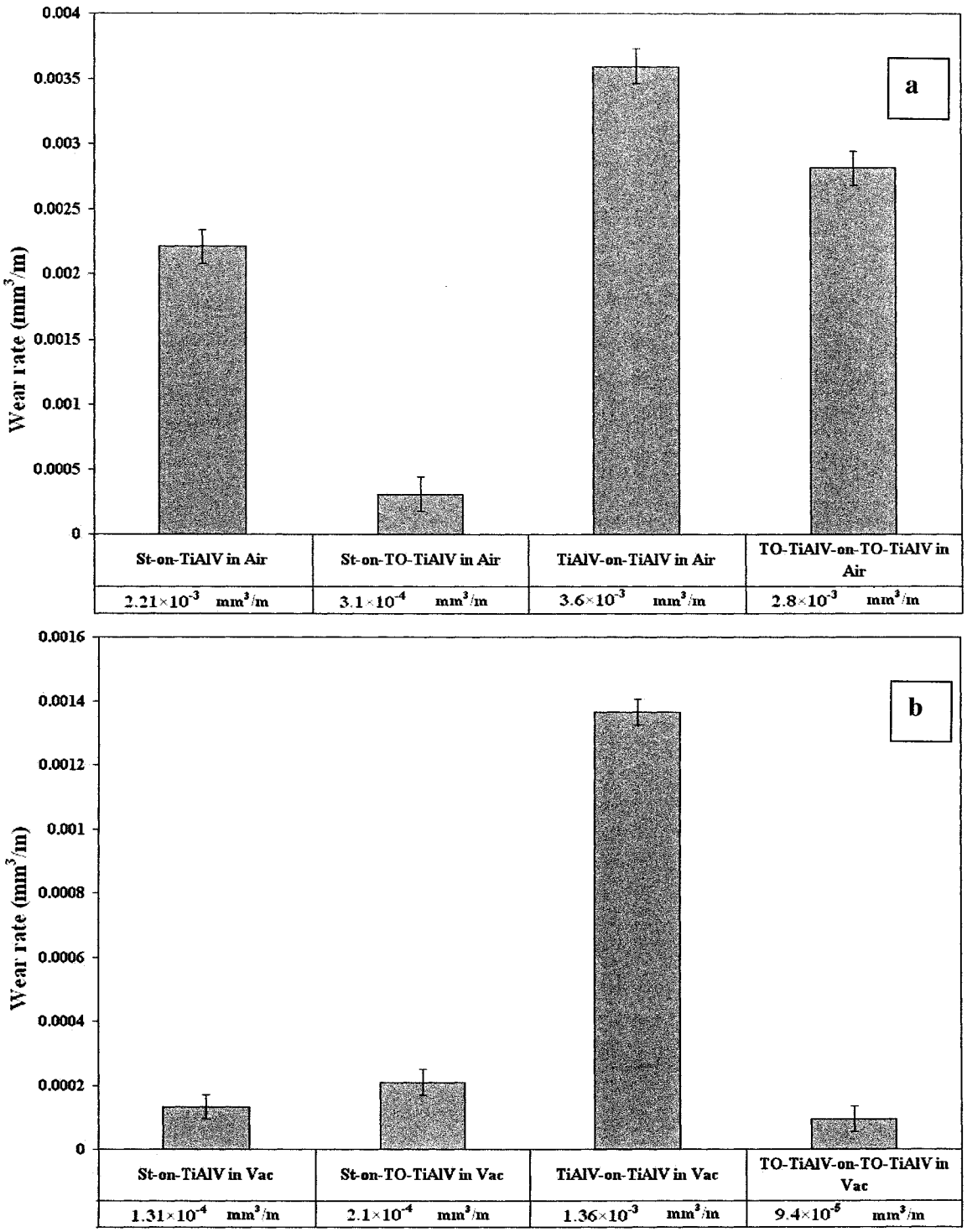

Figure 5.2 Wear rates calculated from volumetric wear damages for samples in (a) ambient air, (b) high vacuum [St: 52100 steel, OxTi: TO-treated Ti-6Al-4V alloy, Ti: Untreated Ti-6Al-4V alloy, Air: Ambient air and Vac: Vacuum of 7×10^{-6} torr]

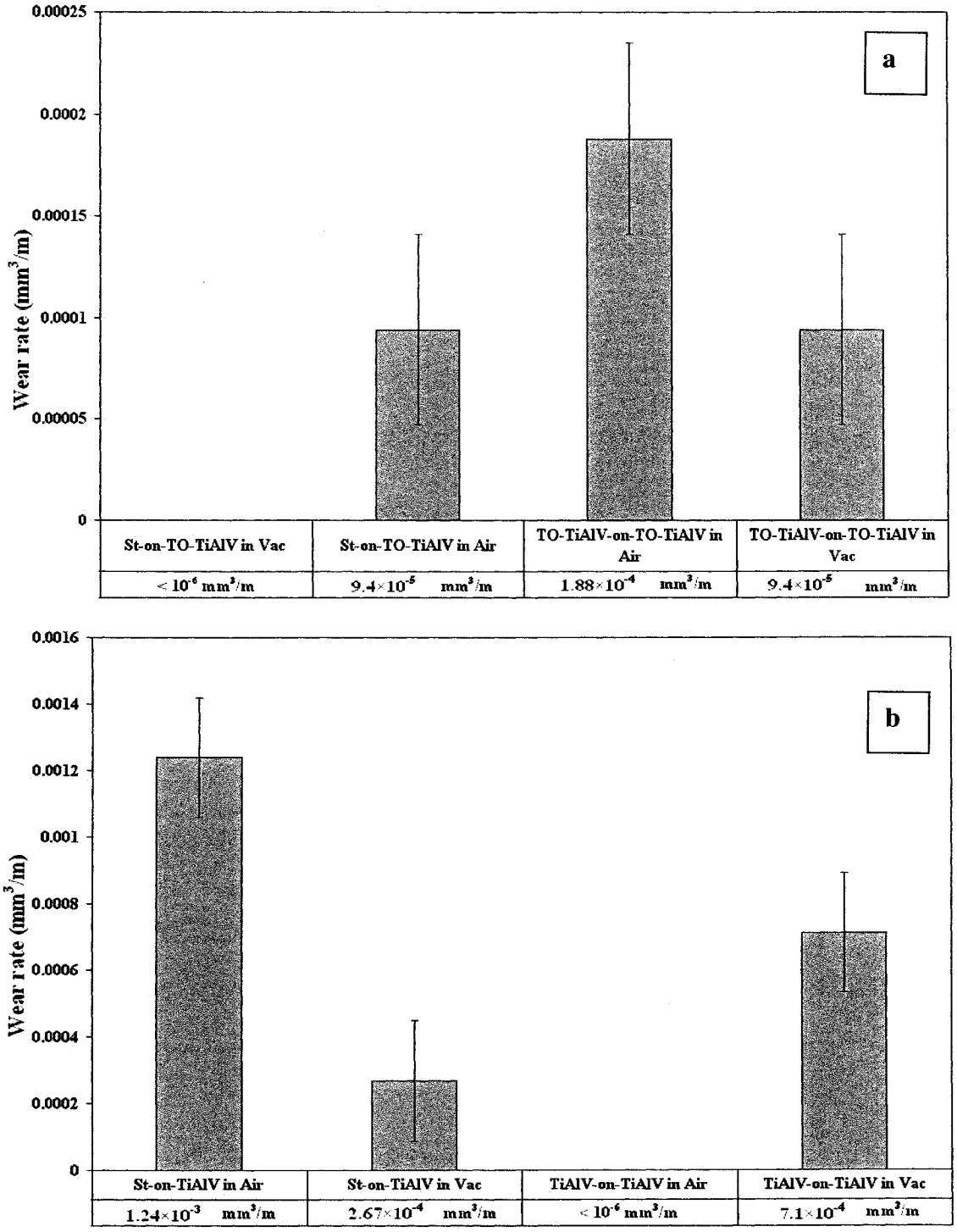

Figure 5.3 Wear rates calculated from mass loss/gain samples in (a) ambient air, (b) high vacuum [St: 52100 steel, OxTi: TO-treated Ti-6Al-4V alloy, Ti: Untreated Ti-6Al-4V alloy, Air: Ambient air and Vac: Vacuum of 7×10^{-6} torr]

5.2 Roughness

5.2.1 Roughness of Worn Surfaces

Surface profilometers of worn surfaces showed rougher surfaces compared to unworn ones. **Table 5.1** presents the roughness of exposed and unworn surfaces of untreated Ti-6Al-4V alloy and TO-treated Ti-6Al-4V alloy. In general, it shows that wear tracks formed during the tests in vacuum have higher surface roughnesses in comparison to the wear tracks in ambient air. Although there was an increase in the roughness in all the worn surfaces, these amounts for the untreated samples were more pronounced. **Fig 5.4-5.6** displays worn surfaces formed under different atmospheric conditions.

5.3. Coefficients of Friction (COF)

5.3.1 COF of Ti-6Al-4V Alloy against 52100 Steel Ball Measured in Air and Vacuum

High fluctuations during sliding between the contact surfaces in ambient air and high vacuum were observed. However, these fluctuations were much higher in case of sliding in ambient air. The steady state of coefficient of frictions for the test in ambient air occurred after 35 m of sliding distance, and it was is 0.60±0.10 (**Fig 5.7a**). The steady state during sliding in vacuum took place almost at the beginning of sliding. The magnitude of COF for vacuum is around 0.43±0.05 (**Fig 5.7b**).

Table 5.1 Roughness of unworn and worn regions of samples (disks) [TO-treated Ti-6Al-4V: TO-treated Ti-6Al-4V, S: 52100 Steel, Ti: Ti-6Al-4V alloy].

Sample (disk) / Counterface	Atmospheric Condition	R_a-Unworn Surface (μm)	R_a-Wear Track (μm)
Ti-6Al-4V / 52100 Steel	Ambient Air		3.4
Ti-6Al-4V / 52100 Steel	Vacuum (7×10^{-6} torr)	0.041	5.58
TO-treated Ti-6Al-4V / 52100 Steel	Ambient Air		N/A
TO-treated Ti-6Al-4V / 52100 Steel	Vacuum (7×10^{-6} torr)	0.159	0.202
Ti-6Al-4V / Ti-6Al-4V	Ambient Air		1.6
Ti-6Al-4V / Ti-6Al-4V	Vacuum (7×10^{-6} torr)	0.033	3.42
TO- treated / TO-treated	Ambient Air		0.182
TO- treated / TO-treated	Vacuum (7×10^{-6} torr)	0.132	0.337

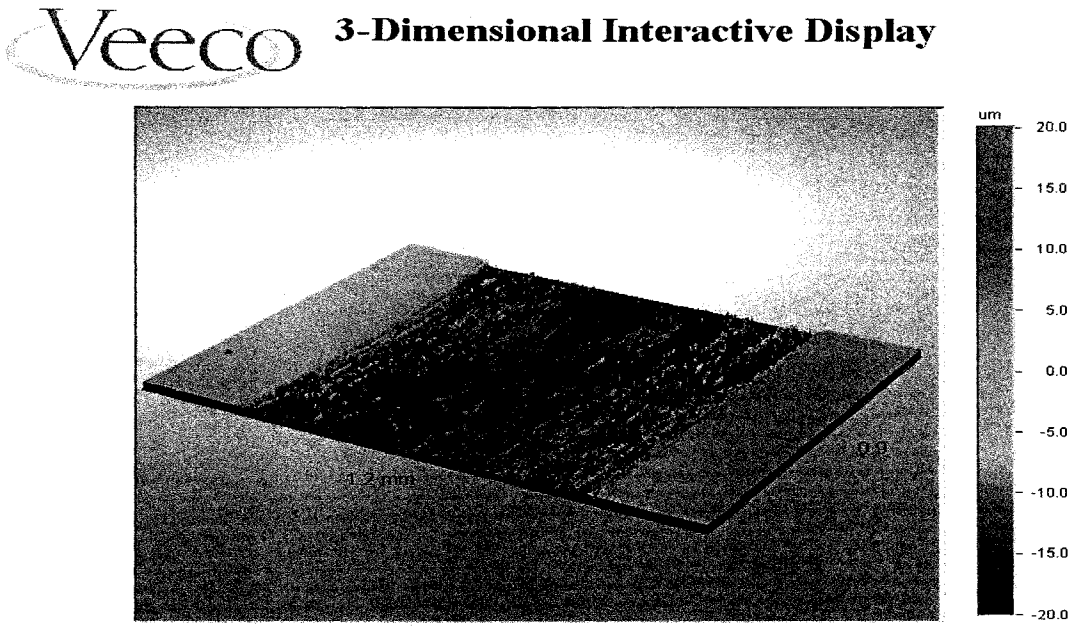

(a)

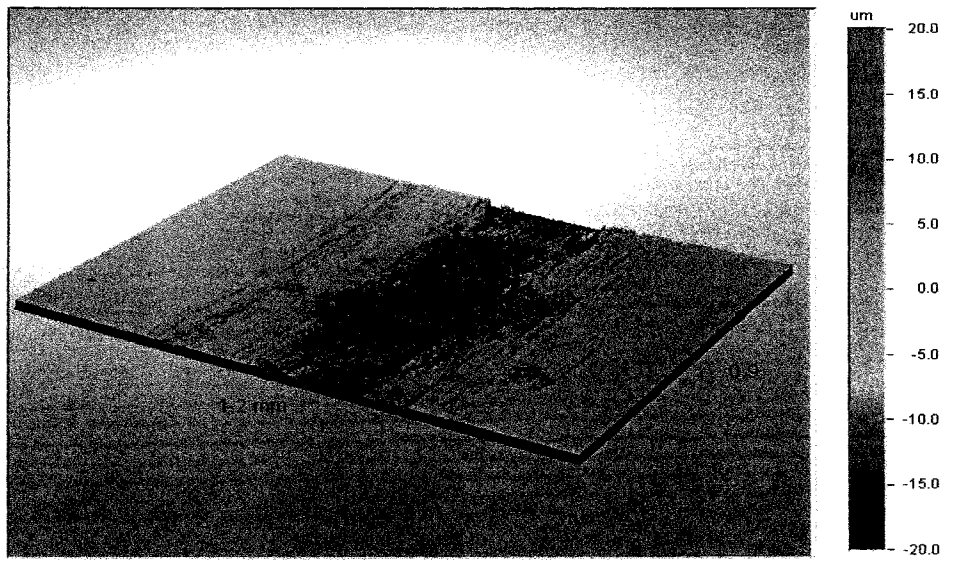

(b)

Figure 5.4 Surface profilometer images from the wear track of the wear track of (a) Ti-6Al-4V alloy slid by 52100 steel in ambient air (b) Ti-6Al-4V alloy slid by 52100 steel in Vacuum.

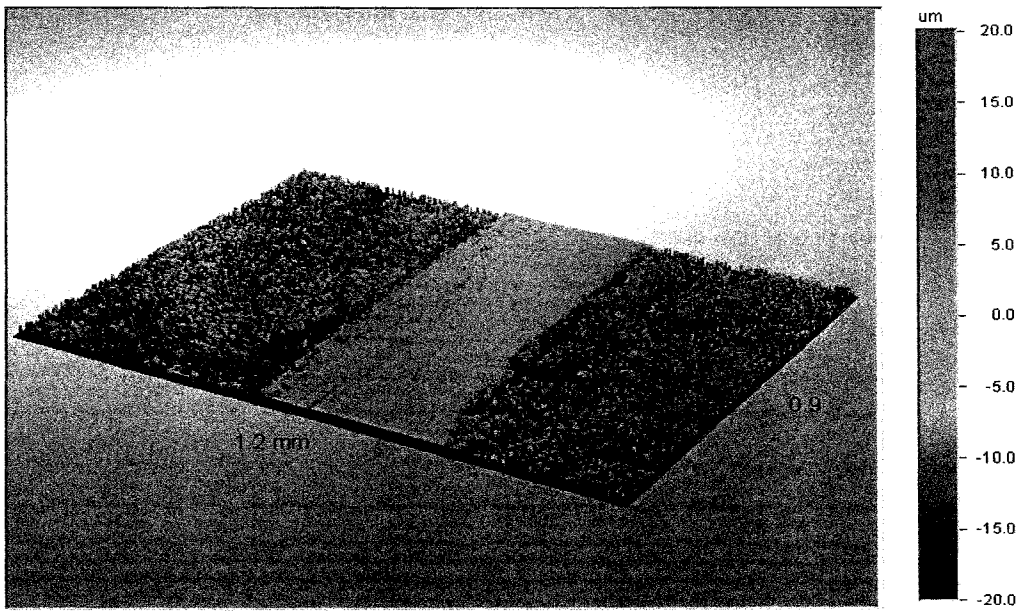

(a)

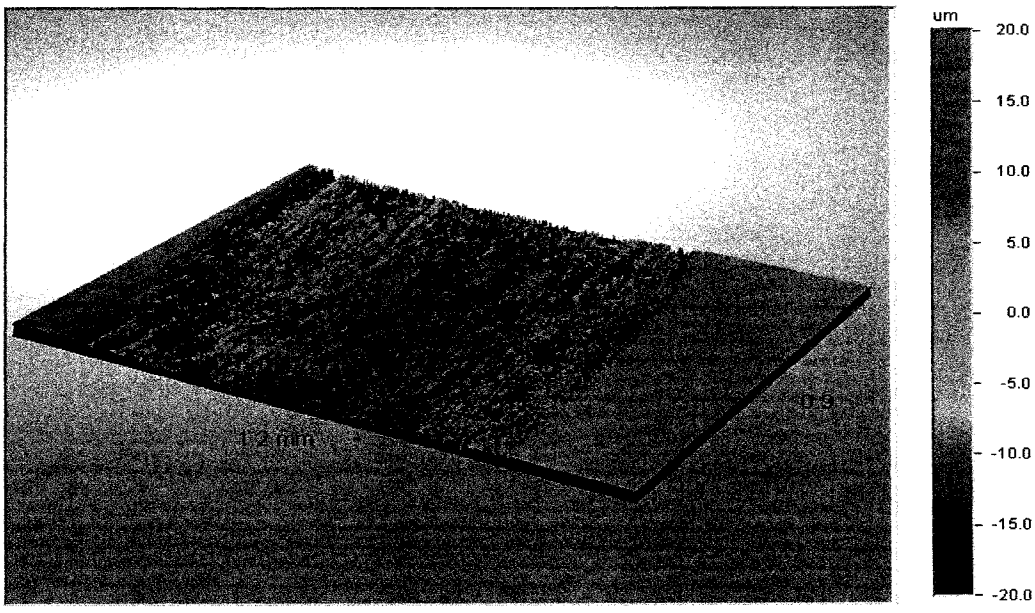

(b)

Figure 5.5 Surface profilometer images from the wear track of the wear track of (a) TO-treated Ti-6Al-4V alloy slid by 52100 steel in vacuum (b) Ti-6Al-4V alloy slid by Ti-6Al-4V alloy in ambient air.

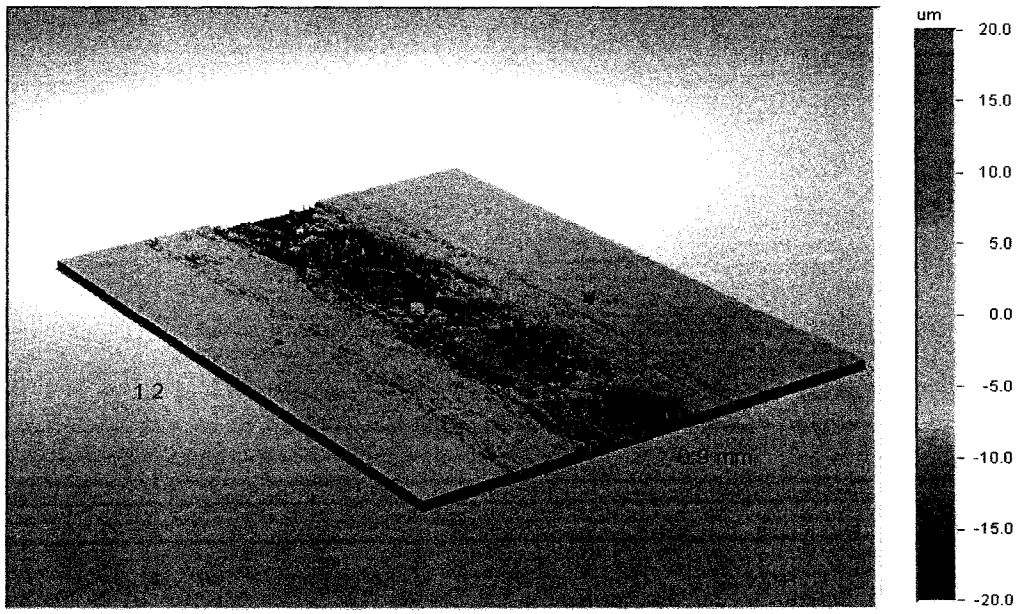

(a)

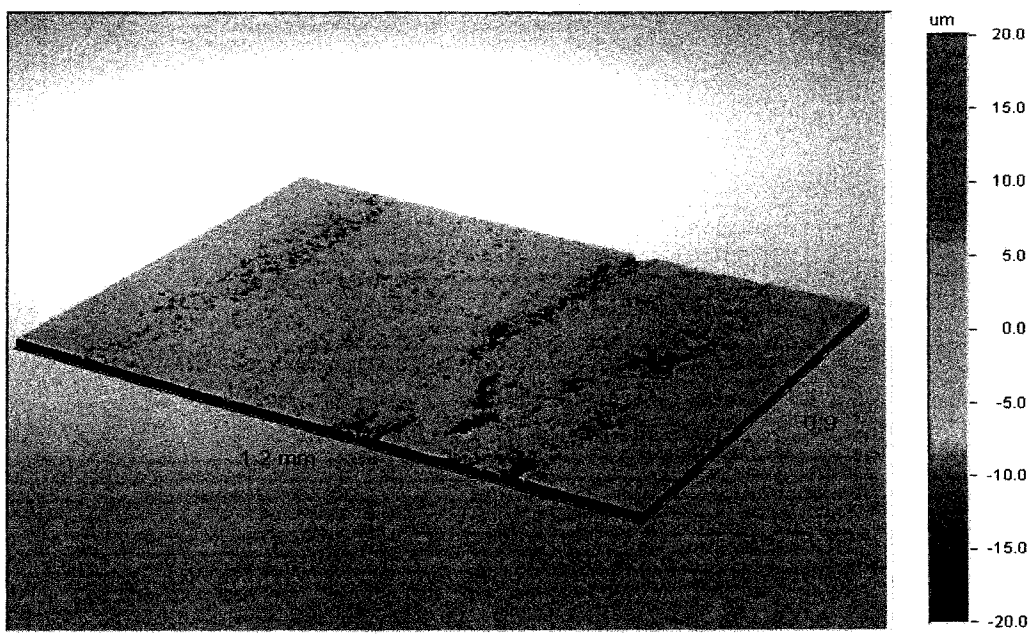

(b)

Figure 5.6 Surface profilometer images from the wear track of the wear track of (a) Ti-6Al-4V alloy slid by Ti-6AL-4V alloy in vacuum (b) TO-treated Ti-6Al-4V alloy slid by TO-treated Ti-6Al-4V in ambient air, in a ball-on-disk system.

5.3.2 COF of TO-treated Ti-6Al-4V Alloy against 52100 Steel Ball Measured in Air and Vacuum

A high steady state COF value in both atmospheric conditions was observed. the magnitude of COF in vacuum was slightly higher than the one in ambient air. The coefficient of friction in ambient air reached its steady state with magnitude of 0.80±0.10 (**Fig 5.8a**). In vacuum the COF was 0.90±0.05 at onset of sliding and decreased to 0.70±0.05 after 50 m of sliding. At this sliding distance COF commenced rising and reached relatively steady magnitude of 0.9±0.1 again (**Fig 5.8b**).

5.3.3 COF of Ti-6AL-4V alloy against Ti-6AL-4V Alloy ball Measured in Air and Vacuum

The coefficient of friction in ambient air between 52100 steel ball and Ti-6Al-4V alloy was 0.45±0.05 (steady state condition) (**Fig 5.9a**).The COF of Ti-6Al-4V worn against itself in vacuum was initially 0.20±0.15. After about 200 m of sliding distance it reached a steady state of 0.30±0.05 (**Fig 5.9b**).

5.3.4 COF of TO-treated Ti-6Al-4V alloy against TO-treated Ti-6Al-4V alloy ball Measured in Air and Vacuum

In ambient air, the COF increased to a high of 0.90±0.05 at 50 m of sliding distance. This magnitude drops and stays around 0.50±0.05 up to 220 m of sliding. At this point, the COF suddenly drops down to 0.7±0.05. The coefficient of friction stays at this level until end of the test (**Fig 5.10a**).The maximum value of coefficient of friction in vacuum reached 0.25±0.03 in vacuum. This value was almost constant during the test (**Fig 5.10b**).

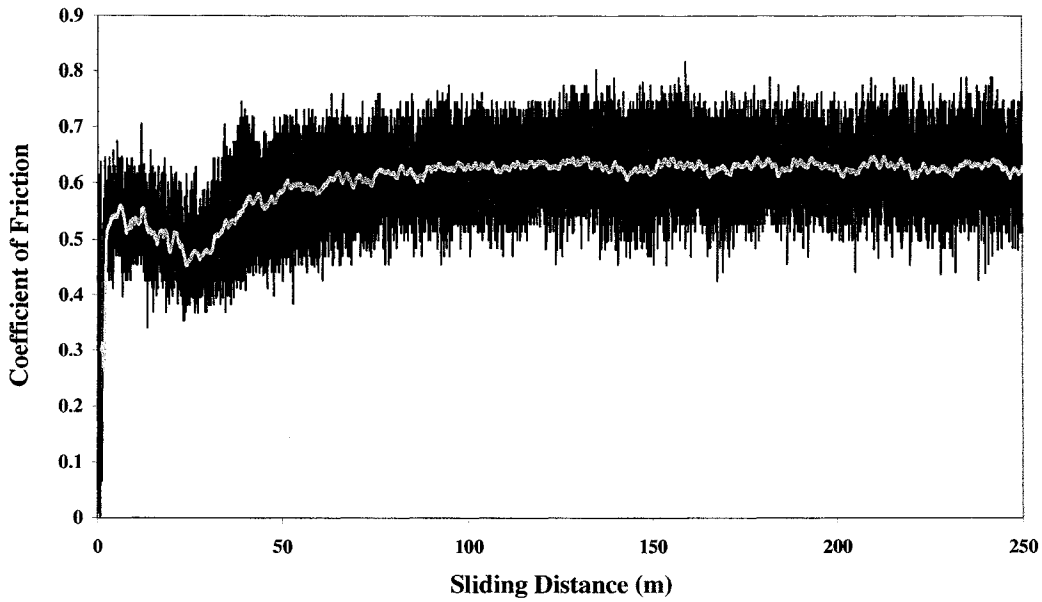

(a)

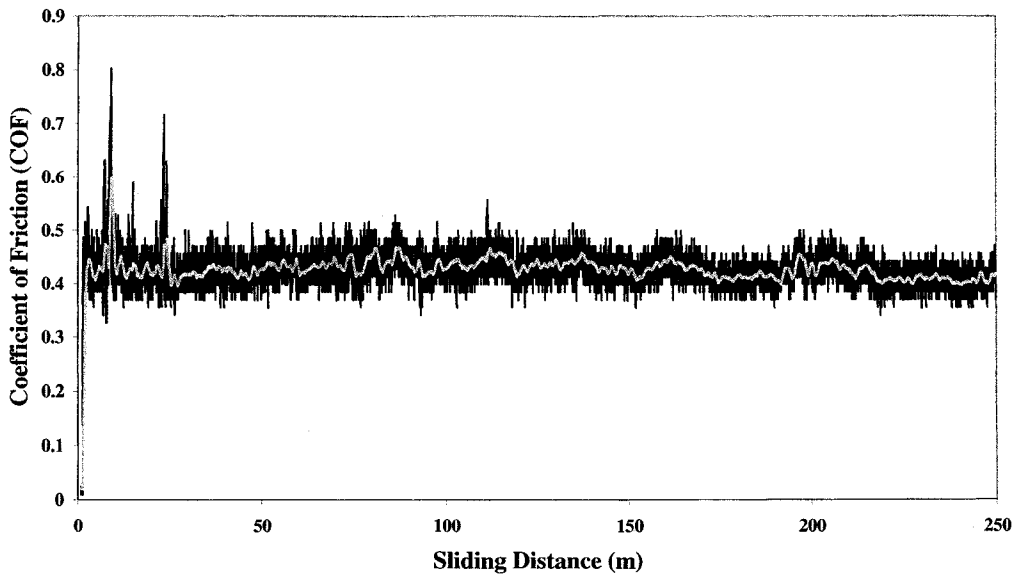

(b)

Figure 5.7 Coefficient of friction during the sliding of 52100 steel ball against disk of untreated Ti-6Al-4V in (a) ambient air (b) vacuum of 7×10^{-6} torr.

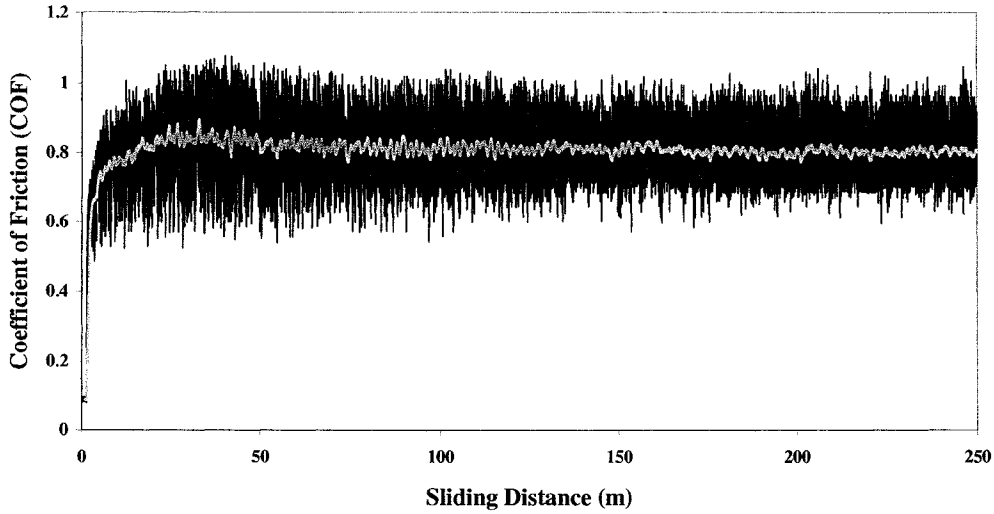

(a)

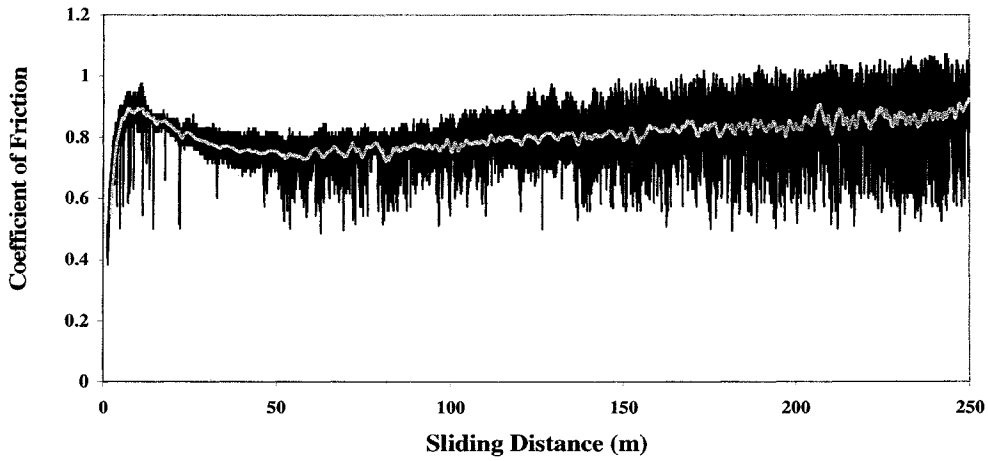

(b)

Figure 5.8 Coefficient of friction during the sliding of 52100 steel ball against disk of TO-treated Ti-6Al-4V in (a) ambient air (b) vacuum of 7×10^{-6} torr.

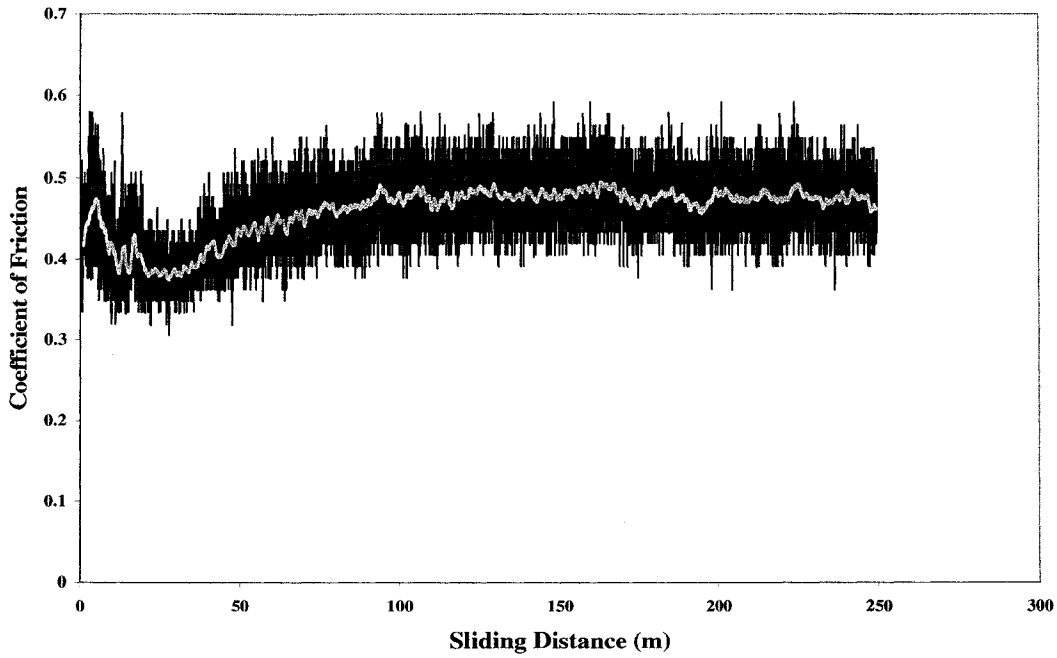

(a)

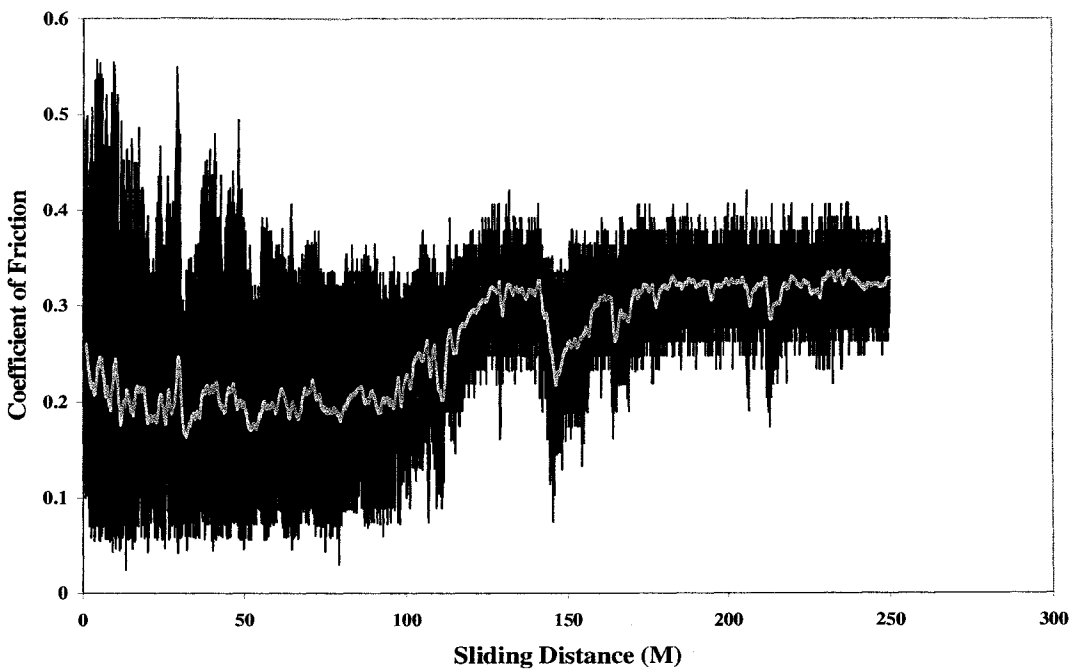

(b)

Figure 5.9 Coefficient of friction during the sliding of Ti-6Al-4V ball against disk of untreated Ti-6Al-4V in (a) ambient air (b) vacuum of 7×10^{-7} torr.

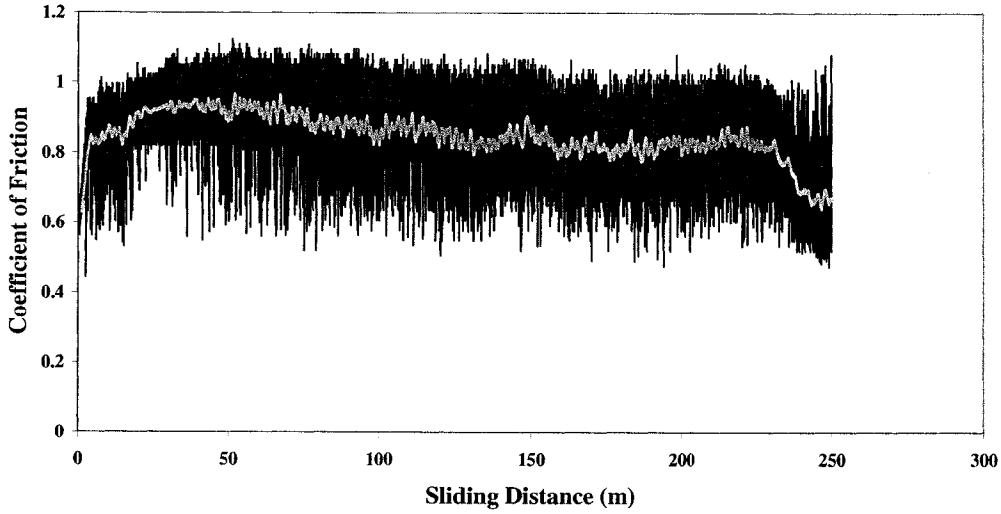

(a)

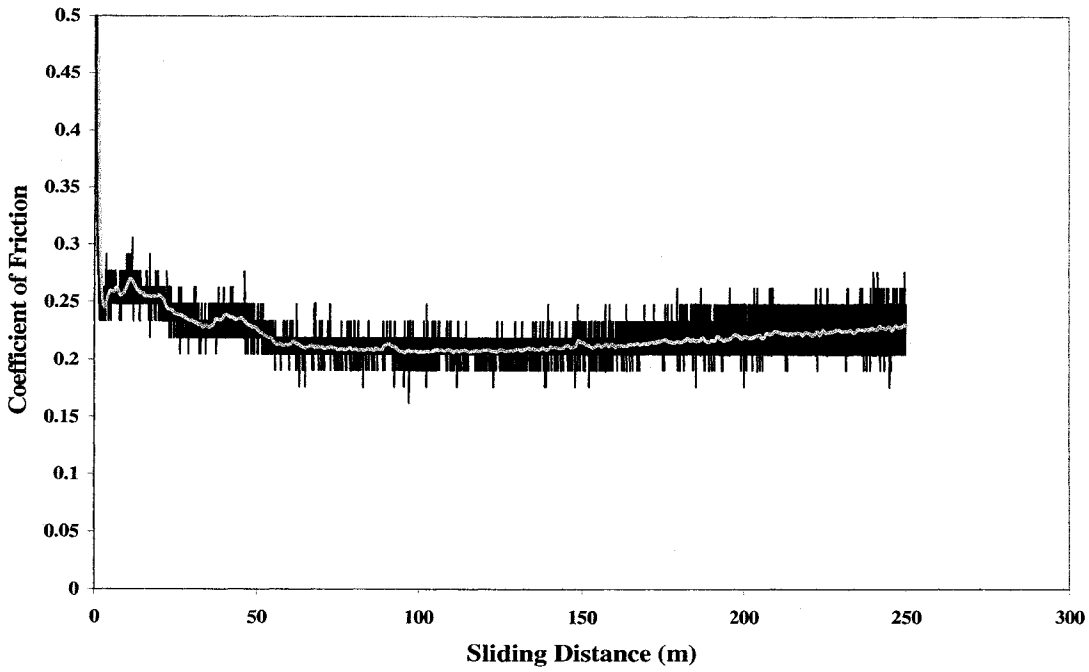

(b)

Figure 5.10 Coefficient of friction during the sliding of TO-treated ball Ti-6Al-4V against disk of TO-treated Ti-6Al-4V in (a) Ambient air (b) vacuum of 7×10^{-7} torr

5.4. SEM and EDS Observations

5.4.1 Wear of Ti-6Al-4V Alloy Disk against 52100 Steel Ball in Air and Vacuum

The secondary electron micrograph presented in **Fig 5.11a** depicts how the worn surface of Ti-6Al-4V alloy was covered by oxidized particles during tests in air. However, abrasive and deformed regions can be detected on the wear track (**See Fig 5.11b**). The backscattered electron image of counterface shows that the debris was adhered to the contact surface (**Fig 5.11c**). No significant worn area was observed on the counterface. In contrast, severe plastic deformation was observed on the worn surface of Ti-alloy tested in vacuum (**see Fig 5.12a**). The EDS analysis of worn surface revealed that no material was transferred from counterface on the damaged area of sample surface. The material transferred to the contact area of the counterface was rich in Ti, Al, and V (**Fig 5.12b**). Plate-like debris was seen on the disk after the tests. The EDS analysis confirmed that the debris was metallic hence no oxygen was detected by EDS. The size of the debris had a wide range from 23×23 μm^2 to 90×95 μm^2. Thus, the severe wear on the plastically deformed surface of Ti-6Al-4V occurred in vacuum and material was transferred to the counterface.

5.4.2 Wear of TO-treated Ti-6Al-4V against 52100 Steel Ball in Air and Vacuum

The secondary electron image of the wear track of TO-treated Ti-6Al-4V alloy tested against the 52100 steel counterface in ambient air was covered by a material of darker colour (**Fig 5.13a**). The EDS analysis confirmed that the material on the worn surface was transferred from the counterface as it consisted of high amounts of Fe (**Fig 5.13b**). The flattened area at the tip of the counterface is presented in **Fig 5.14.** Very little transferred material from the worn sample to the 52100 steel counterface is detectable.

In case of sliding of 52100 steel ball on the TO-treated Ti-6Al-4V alloy in vacuum, wear was observed on the sample but the wear track was mostly featureless (**Fig 5.15a). Fig 5.16a** and **Fig 5.16b** illustrate formation of the patches of agglomerated debris that were piled up at the edges of wear track. They consist of mixture of material from the worn surface of sample and transferred material from the counterface (Mo, Mn, Cr, and Fe).

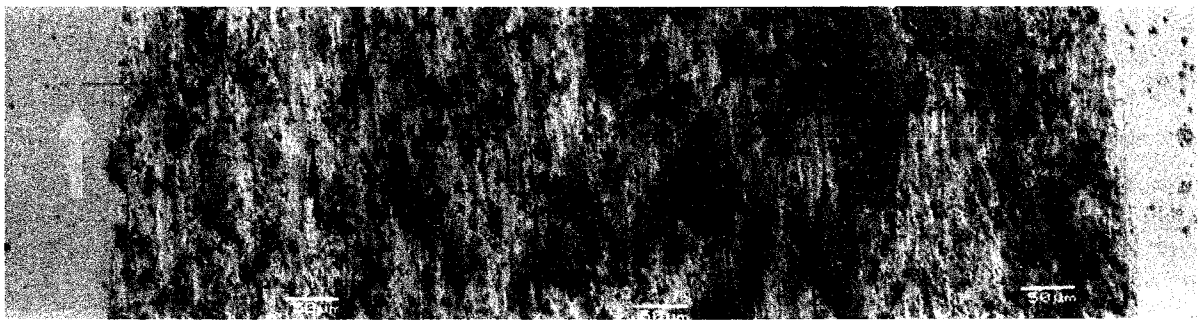

(a)

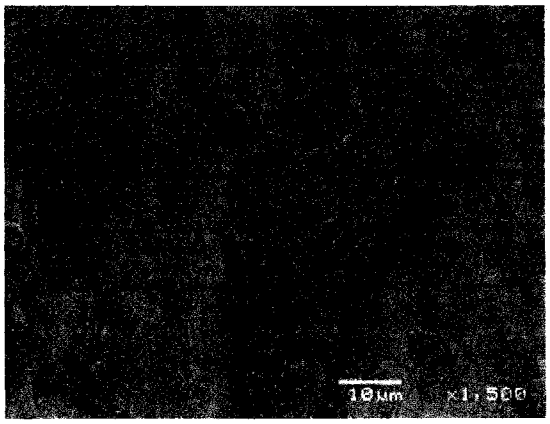

(b)

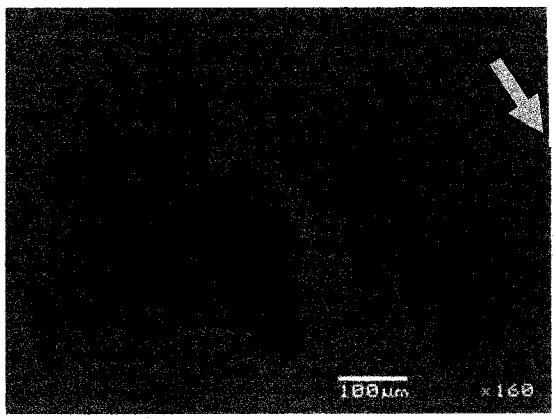

(c)

Figure 5.11 Secondary and Backscattered SEM micrographs of contact surfaces between 52100 steel and untreated Ti-6Al-4V in ambient air: (a) Secondary image of worn surface of untreated Ti-6Al-4V shows oxidization on the surface, (b) sign of abrasive wear on wear track of untreated Ti-6Al-4V (Backscattered SEM micrograph), (c) secondary SEM micrograph of oxidized Ti-6Al-4V alloy adhered on the contact surface of 52100 steel counterface. [Arrows show the sliding direction]

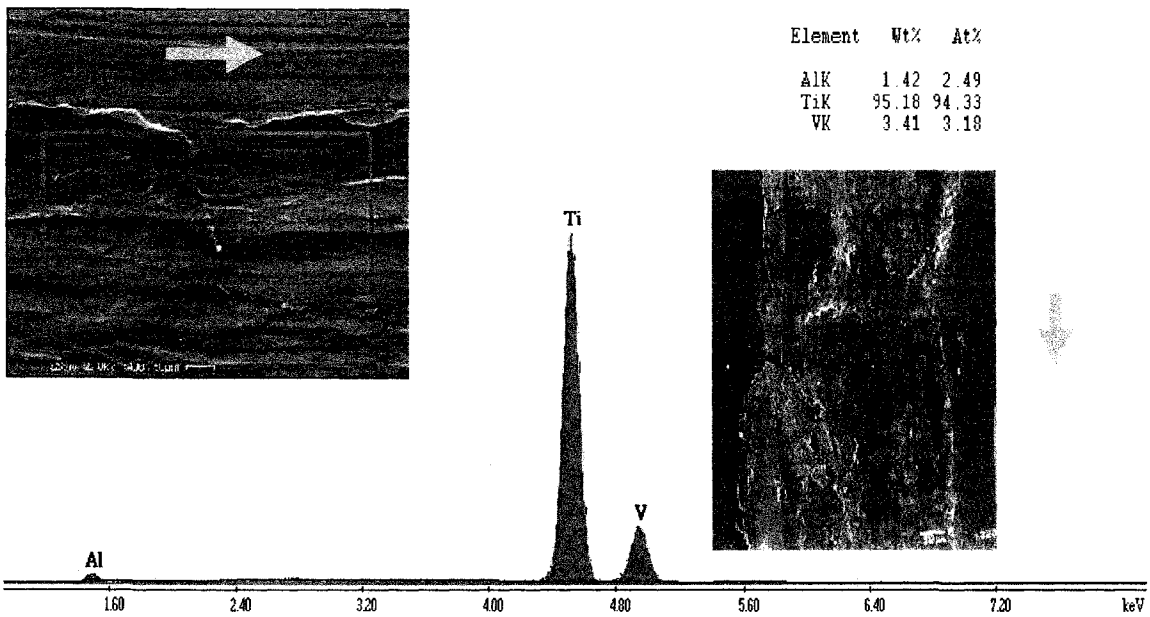

(a)

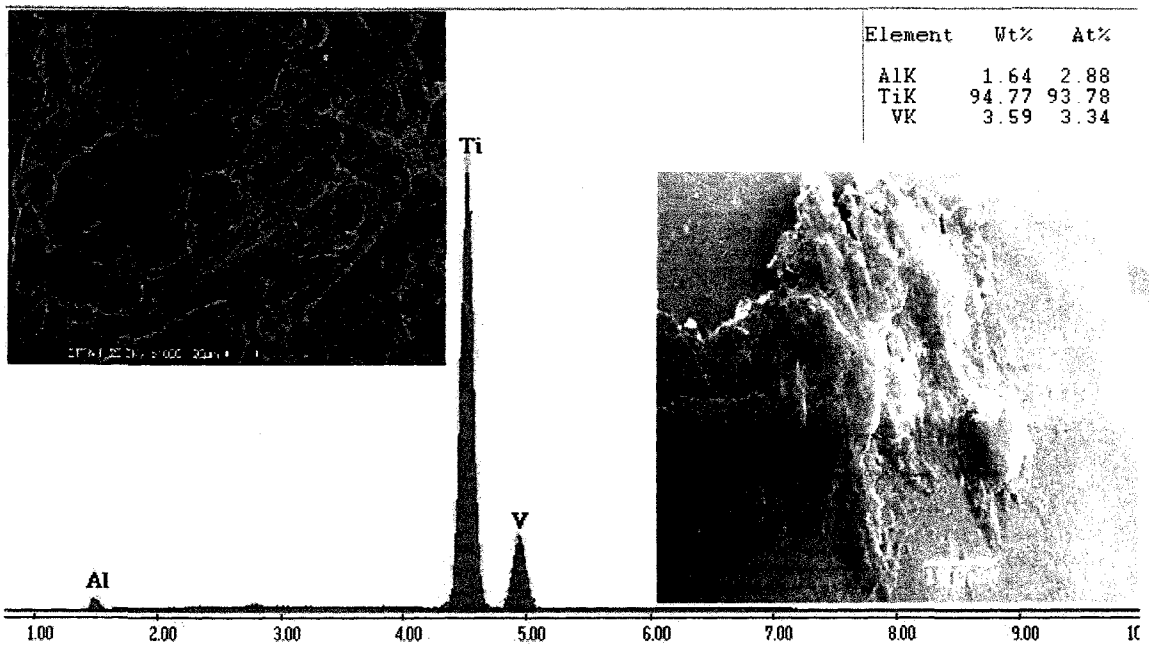

(b)

Figure 5.12 Secondary SEM micrograph and EDS analysis of (a) untreated Ti-6Al-4V surface worn by 52100 steel counterface in 7×10^{-6} torr, (b) transferred material from the surface of Ti-6Al-4V alloy to the ball of 52100 steel. [Arrows show the sliding direction]

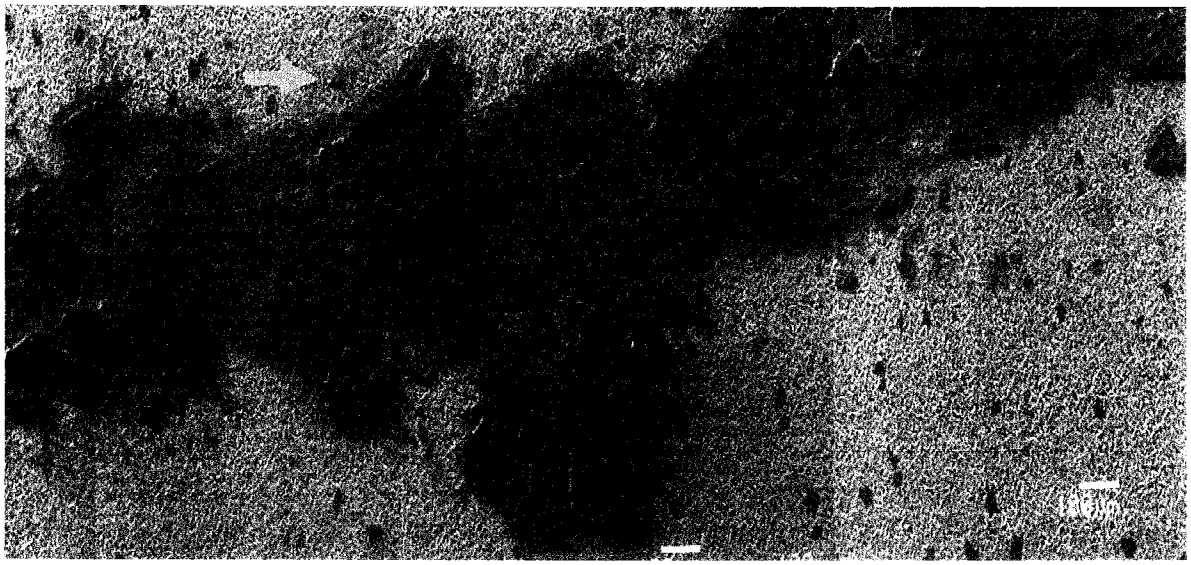

(a)

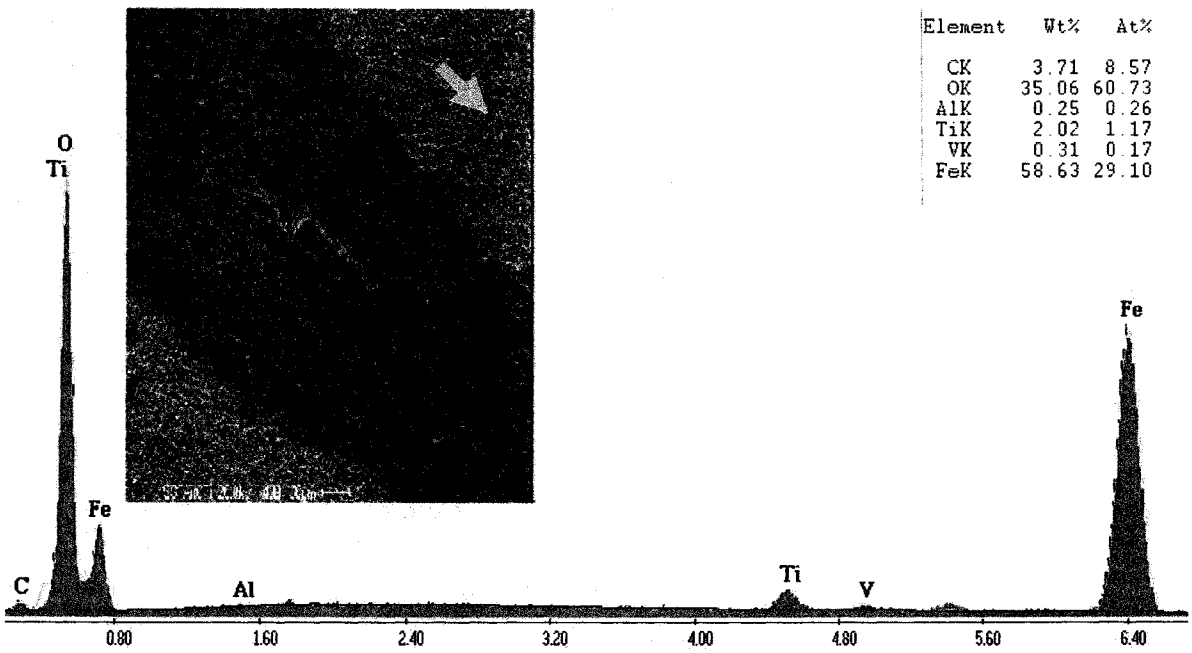

(b)

Figure 5.13 (a) Secondary SEM micrograph of the worn surface of TO-treated Ti-6Al-4V alloy sliding against 52100 steel in ambient air, (b) EDS analysis of wear track of TO-treated Ti-6Al-4V alloy shows the fragments consist of material from the counterface.[Arrows show the sliding direction]

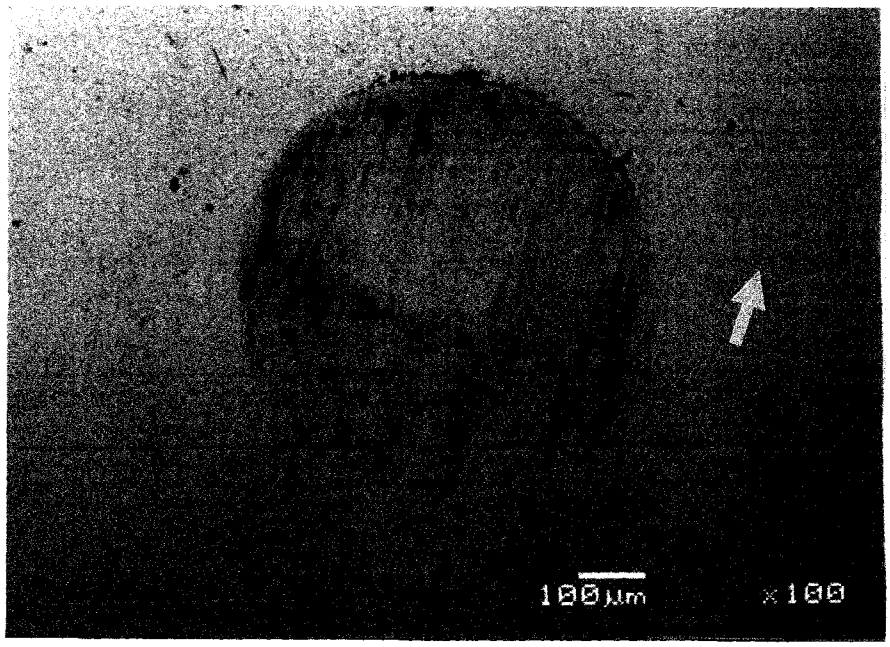

Figure 5.14 Secondary SEM micrograph of the flattened surface of ball (52100 steel) after sliding against TO-treated Ti-6Al-4V alloy in ambient air. [Arrows show the sliding direction]

In comparison to counterface in tested ambient air, a larger size of flattened area was seen on the SEM image of counterface in contact with thermally oxidized Ti-6Al-4V alloy in vacuum (see **Fig 5.15b**). The transferred material including O, Ti, Al, and V, namly material removed from the sample surface become adhered on the flattened area of counterface **Fig 5.17.**

5.4.3 Cross Sections (90° and 3.6° Taper) of Untreated Ti-6Al-4V Alloy Sample Slid by 52100 Steel Counterface under 7×10^{-6} torr of Pressure

Observation of plate-like debris in dry sliding wear of 52100 steel counterface against the untreated Ti-6Al-4V alloy sample triggered a set of experiment to examine the tapered cross sections of wear tracks. This was carried to find out if there were any micro-cracks underneath the worn area. Cross sectional metallurgy revealed that especially β-phase was smeared on the contact surface due to severe deformation and high damage during sliding. Highly deformed area was detectable on both secondary SEM images. No cracks could be detected at least in the observed regions (**Fig 5.18**). The effective depth of worn area used for 90° cross sectional analysis of the sample was 100±10 μm and for tapered section was 85±5 μm.

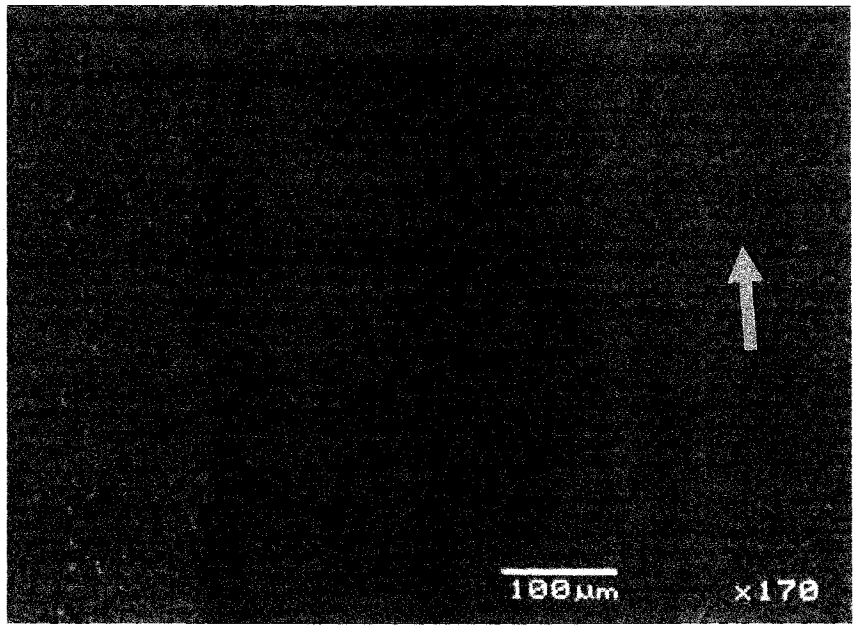

(a)

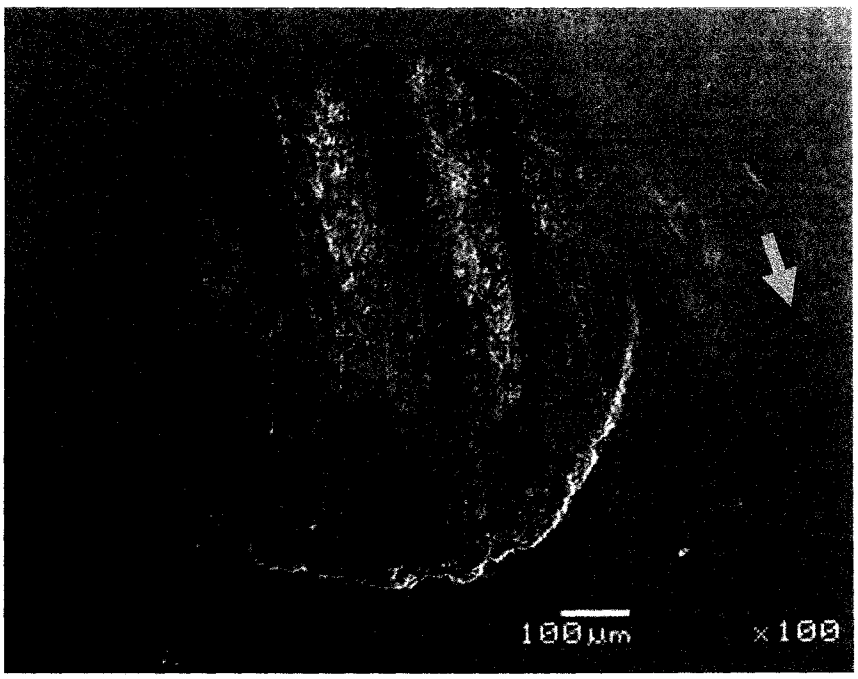

(b)

Figure 5.15 (a) Secondary SEM micrograph of worn surface of TO-treated Ti-6Al-4V alloy slid against 52100 steel in 7×10^{-6} torr, (b) secondary SEM micrograph of tip of counterface (52100 steel). [Arrows show the sliding direction]

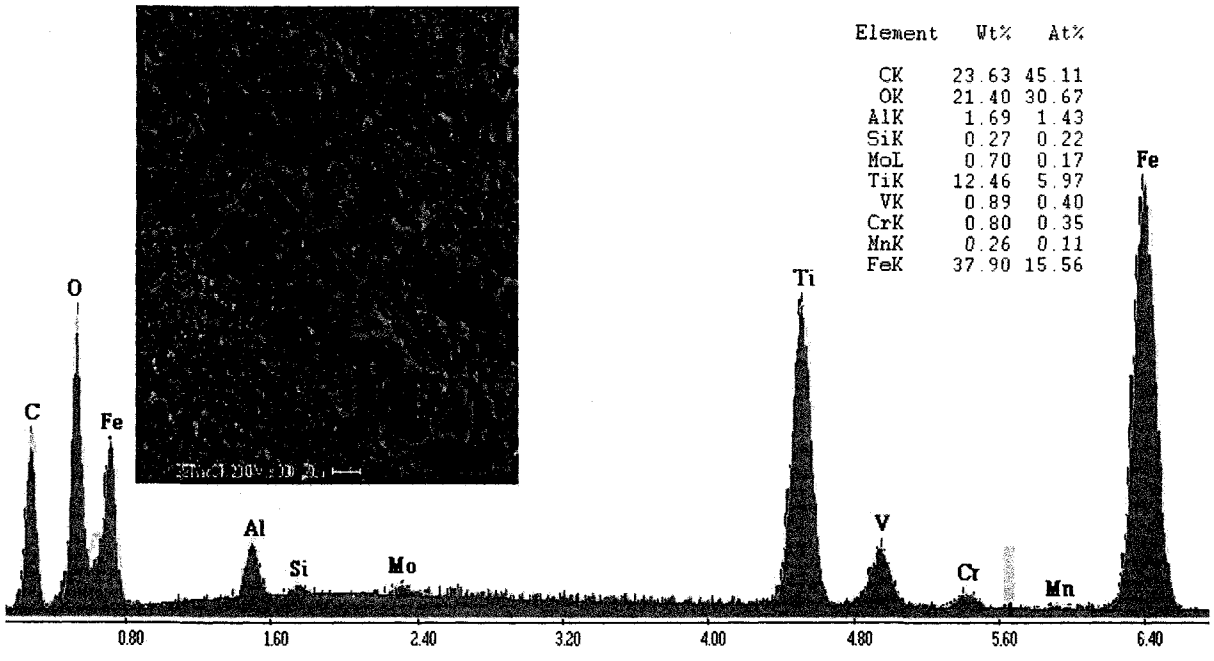

(a)

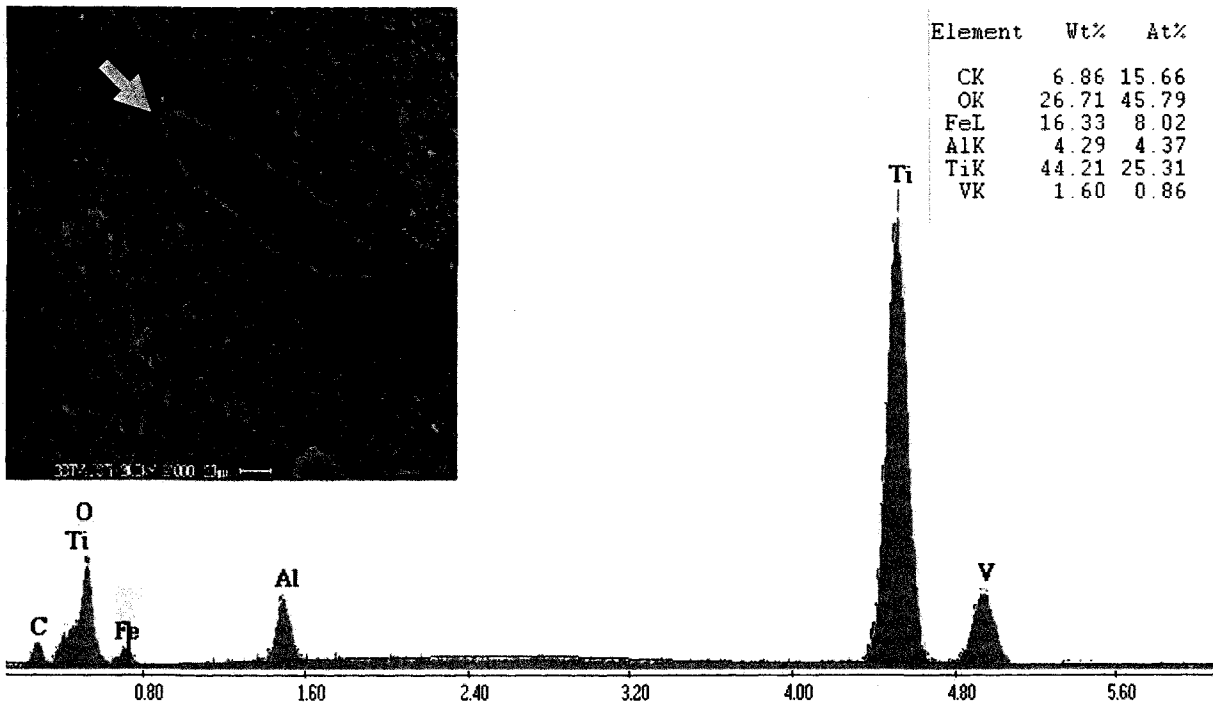

(b)

Figure 5.16 EDS analysis of wear track of TO-treated Ti-6Al-4V alloy worn by 52100 steel counterface in 7×10^{-6} torr shows (a) the debris accumulated around the wear track (b) worn area of sample consist of material from the counterface. [Arrows show the sliding direction]

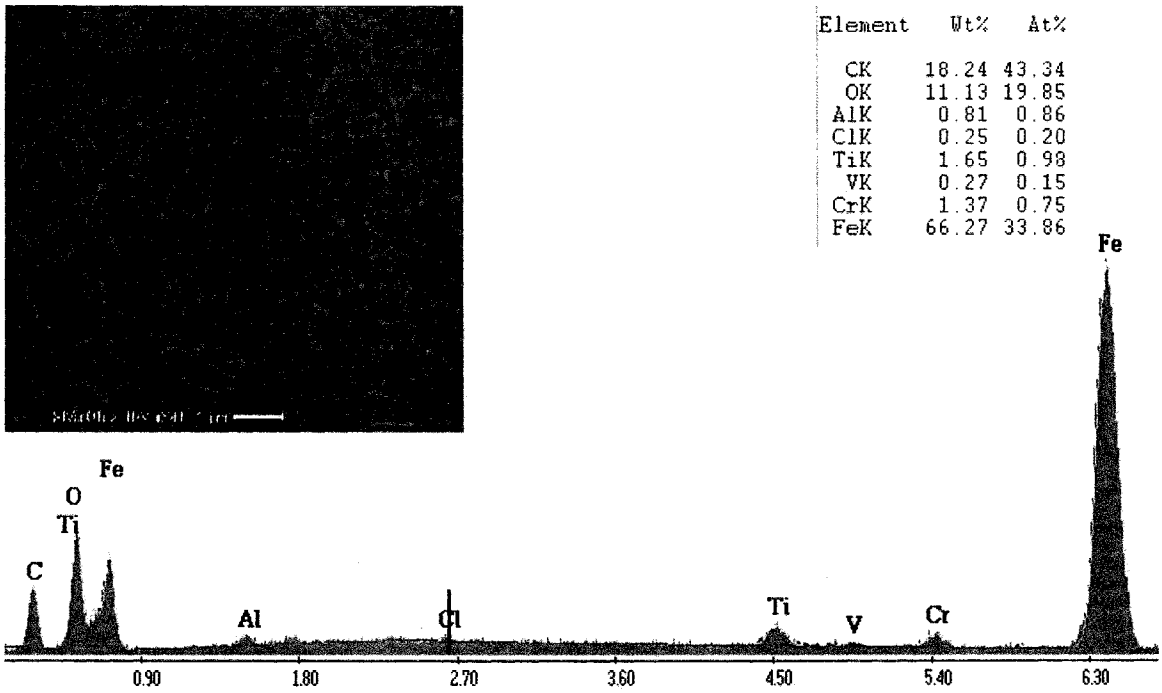

Figure 5.17 EDS analysis of flattened surface of 52100 steel counterface slid on TO-treated Ti-6Al-4V alloy in vacuum. The EDS analysis is related to transferred material and debris adhered on the flattened area

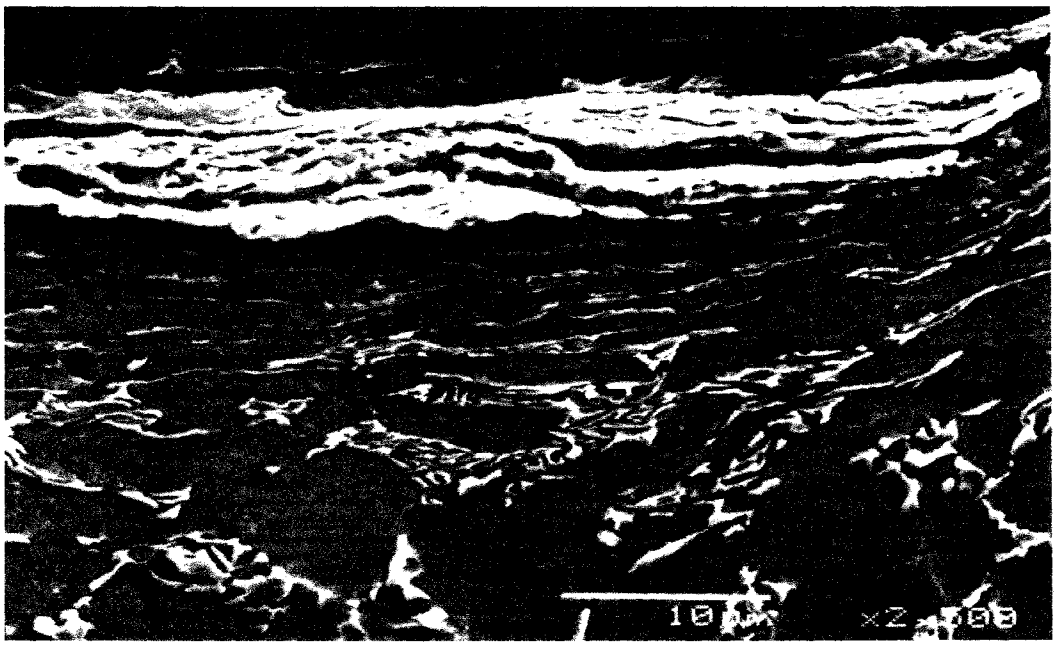

(a)

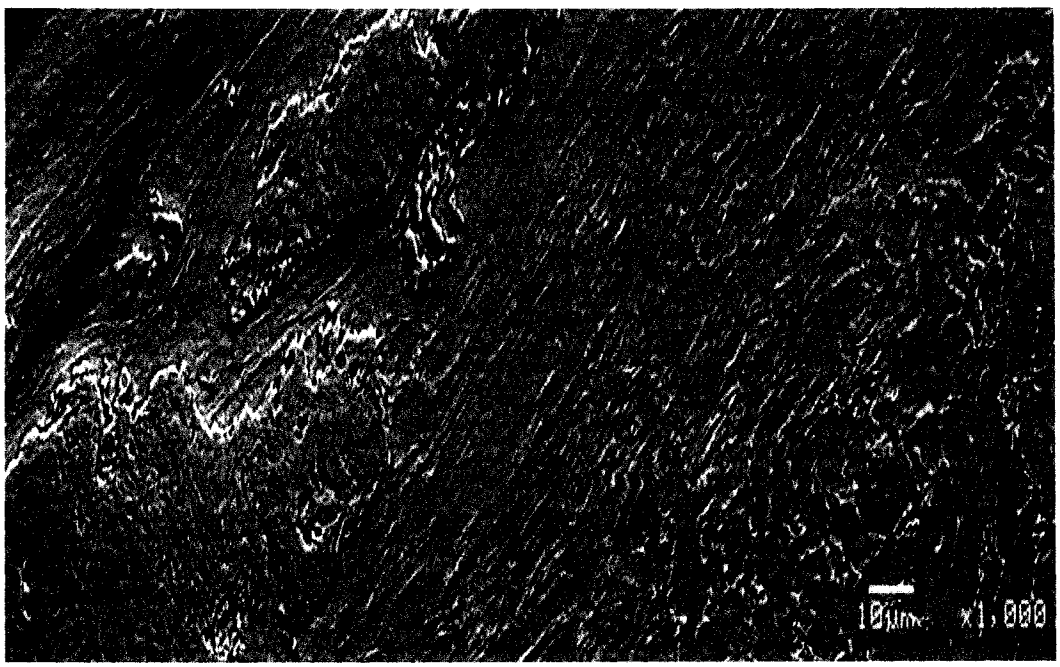

(b)

Figure 5.18 Secondary SEM micrographs of subsurface of Ti-6AL-4V alloy slid by a ball of 52100 steel at vacuum of 7×10^{-6} torr: (a) cross-section and (b) tapered section of Subsurface of wear track show the phases, particularly β-phase of Ti-alloy has been smeared due to combination of normal and shear load.

5.4.4 Wear of Ti-6Al-4V Alloy against Ti-6Al-4V alloy Ball in Air and Vacuum

The Secondary electron micrograph (SEM) of Ti-6Al-4V sample tested in air showed that the debris particles covered the whole wear track (**Fig 5.19a**). These particles did not agglomerate to each other, but were dispersed on the wear track. Higher magnification SEM micrograph confirmed the presence of abrasive wear (**See Fig 5.19b**). The SEM micrograph given in **Fig 5.19c** showed that the flattened surface of counterface was covered by debris. These debris particles were either transferred from the wear track or generated and oxidized during the wear of counterface and transferred back to the flattened surface. The EDS analysis of both contact surfaces confirmed occurrence of oxidation during wear as debris are oxidized (**Fig 5.20**).

In case of sliding of Ti-6Al-4V alloy on Ti-6Al-4V alloy tested in high vacuum, severe plastic deformation occurred on the worn area of the Ti-6Al-4V alloy. In addition to highly deformed surface, a slip-stick type phenomenon was apparent, as it was the case for sliding of a 52100 steel counterface on Ti-6Al-4V alloy (**Fig 5.21a**). The backscattered SEM micrograph presented in **Fig 5.21b**, displays a view of the transferred material from the worn surface, and metallic debris adhered on the ball surface. The worn area of counterface still can be seen in the image. The EDS analysis showed that no detectable oxidation occurred during the sliding process under vacuum (**Fig 5.22**). Presence of carbon was suspected to exist in the vapour of the diffusion pump.

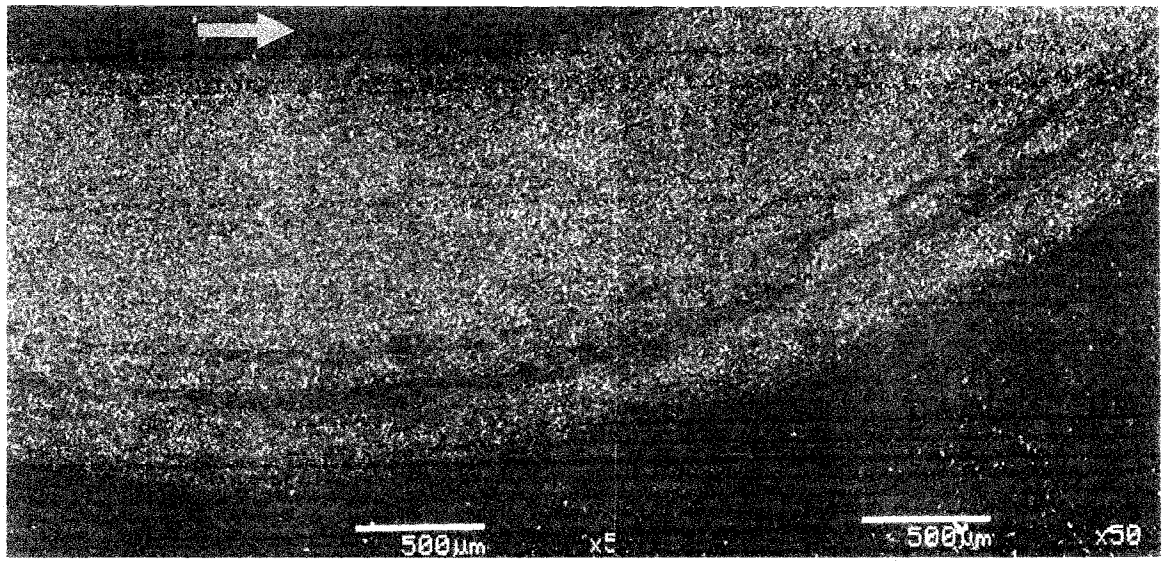

(a)

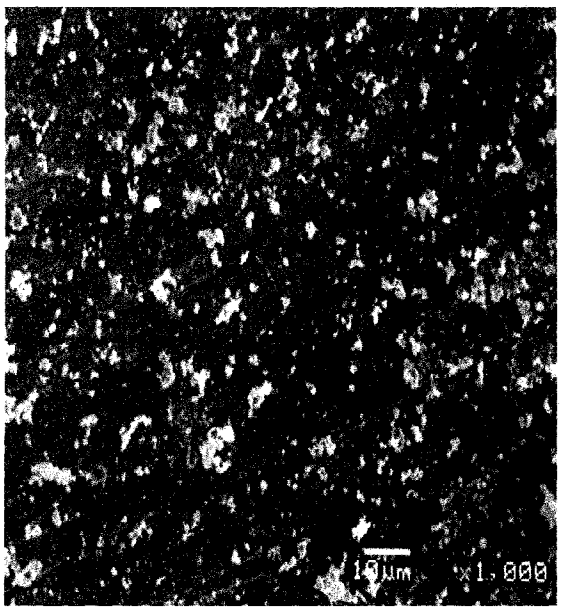

(b)

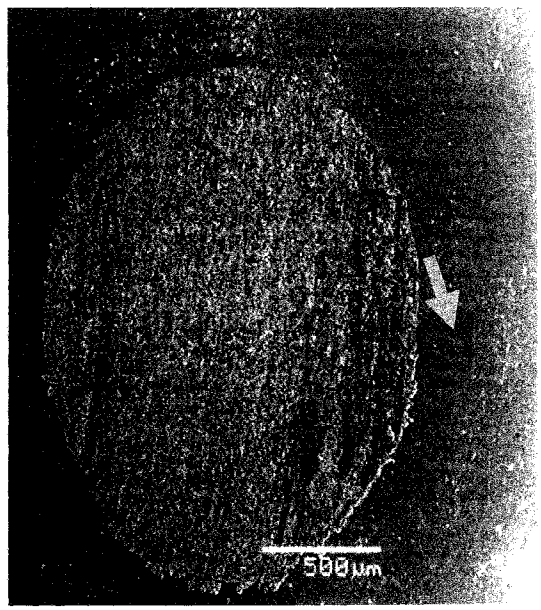

(c)

Figure 5.19 Secondary SEM micrographs of contact surface of Ti-6Al-4V alloy worn by Ti-6Al-4V alloy counterface in ambient air: (a) worn surface of Ti-6Al-4V alloy, (b) the abraded area emerges on the worn surface of sample (c) contact area of counterface. [Arrows show the sliding direction]

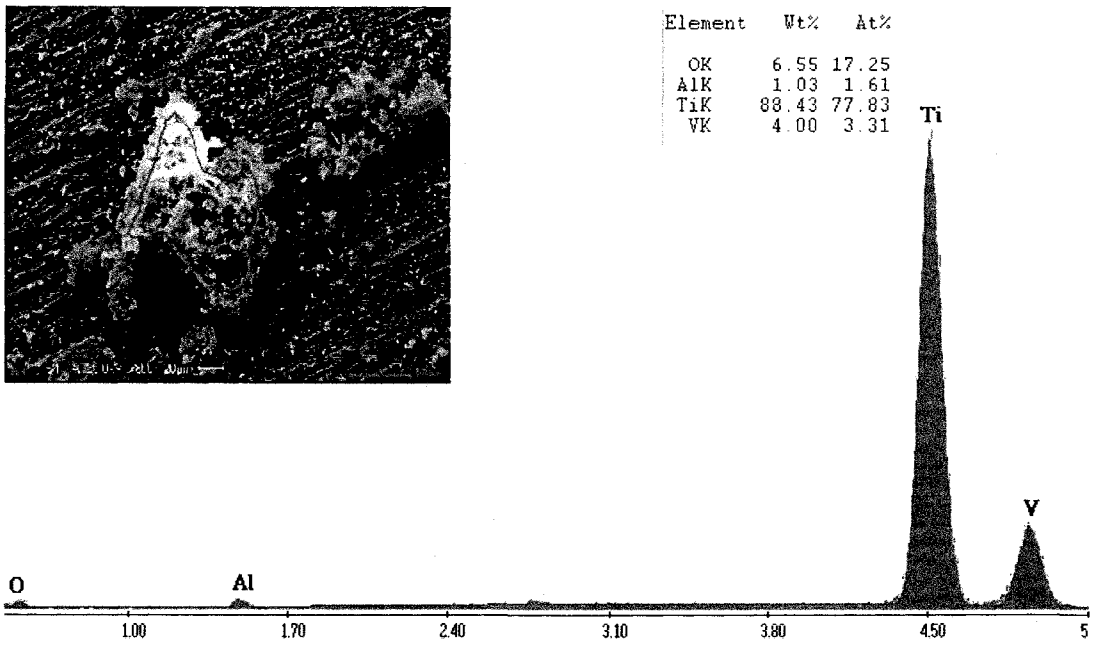

(a)

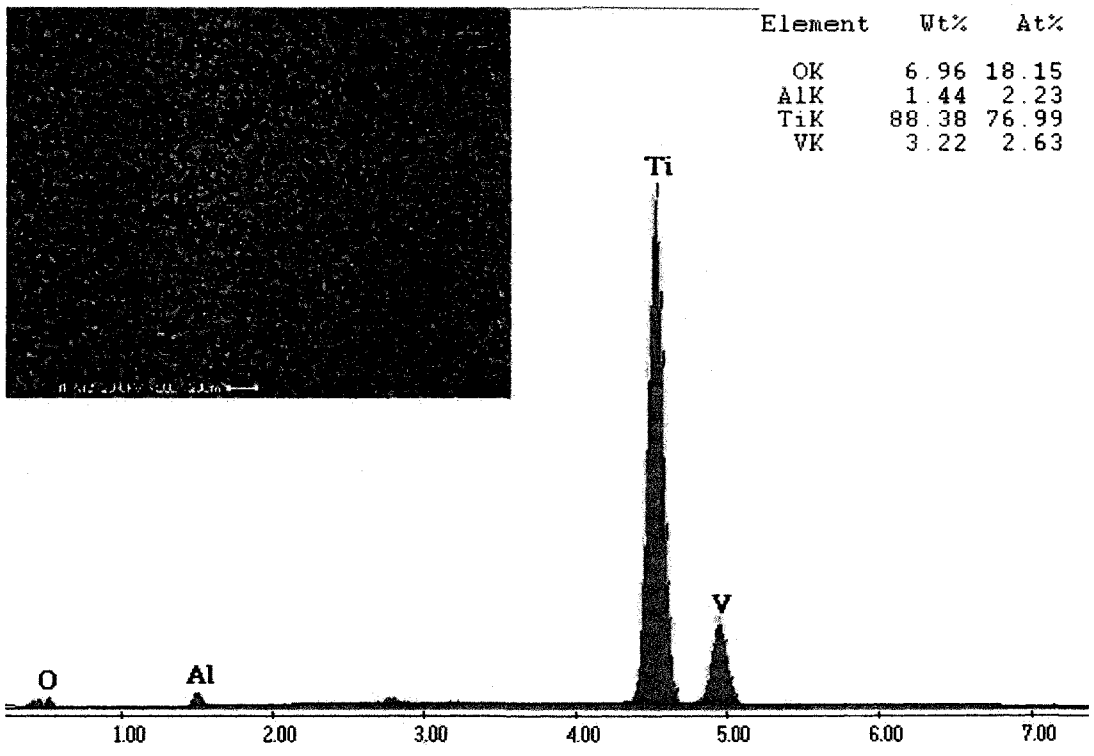

(b)

Figure 5.20 EDS analysis of (a) debris on the worn surface of Ti-6Al-4V alloy worn by the same material counterface in ambient air (b) debris on the flattened surface of Ti-6Al-4V counterface slid on Ti-6Al-4V alloy in ambient air.

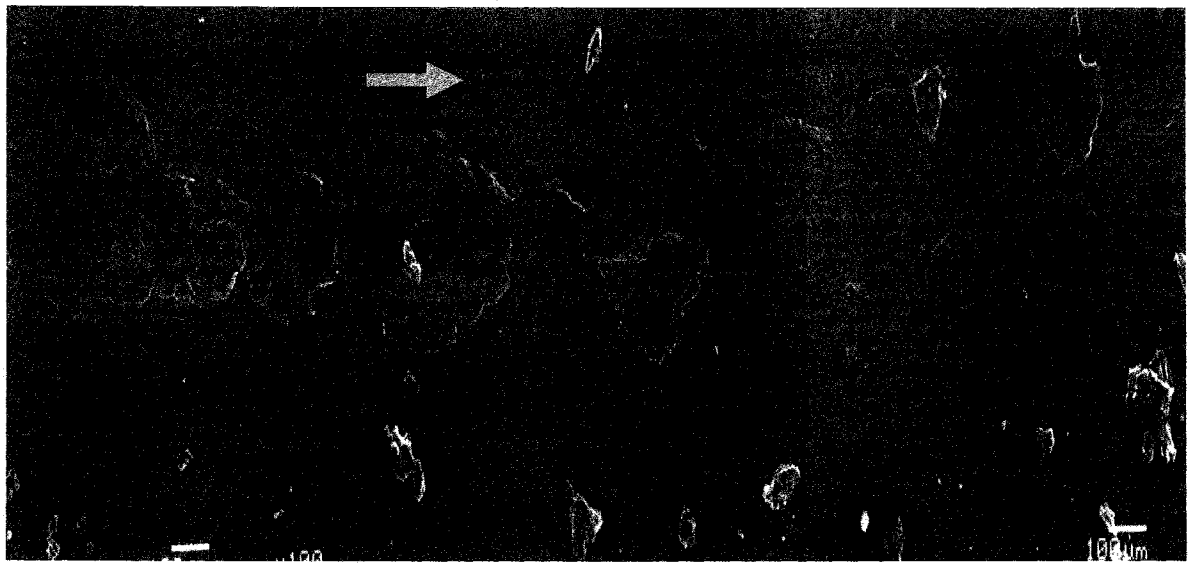

(a)

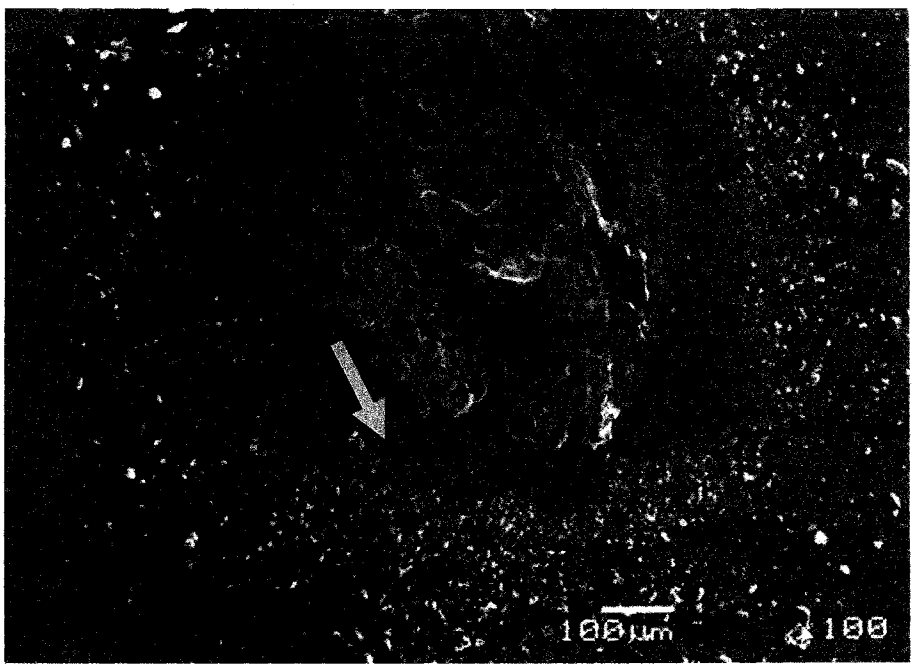

(b)

Figure 5.21 Secondary SEM micrographs of contact surfaces between ball of Ti-6Al-4V alloy against disk of Ti-6Al-4V alloy in 7×10^{-6} torr: (a) worn surface of Ti-6Al-4V alloy, (b) contact area of counterface. [Arrows show the sliding direction]

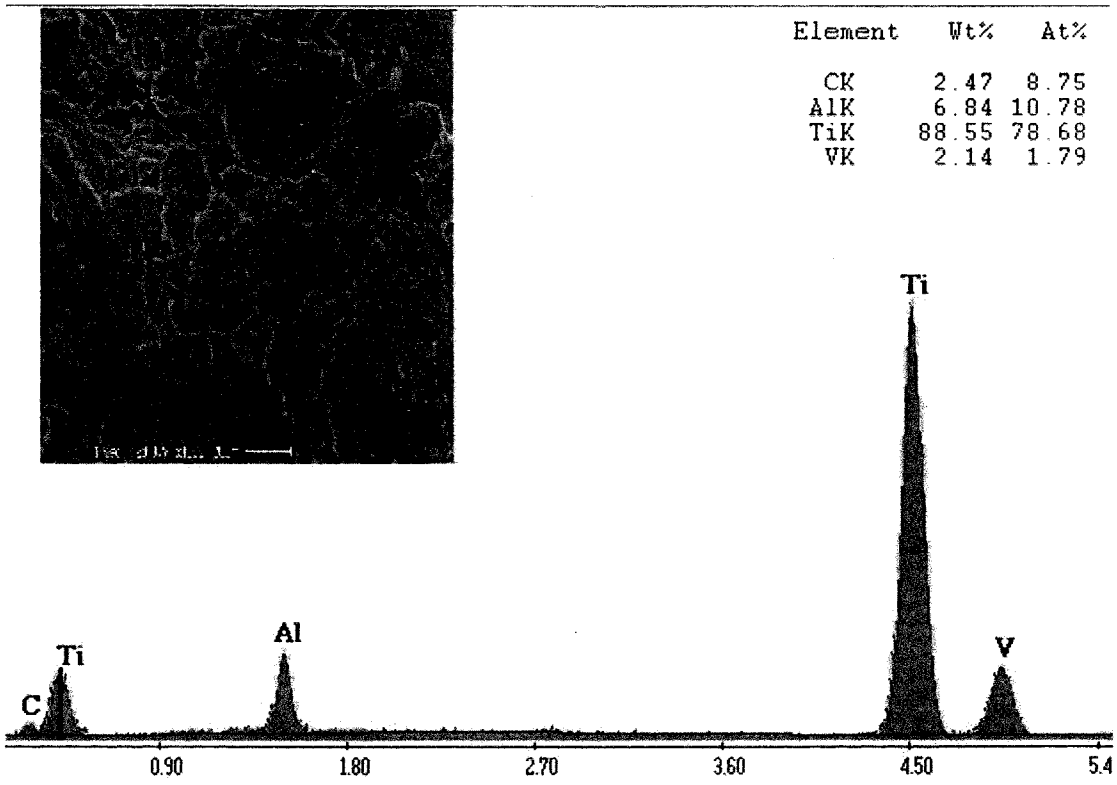

Figure 5.22 EDS analysis of transferred material to the Ti-6Al-4V alloy counterface slid on Ti-6Al-4V alloy sample in vacuum of 7×10^{-6} torr. No oxygen detected in vacuum.

5.4.5 Wear of TO-treated Ti-6Al-4V against TO-treated Ti-6Al-4V ball in Air and High Vacuum

The backscattered SEM micrograph of TO-treated Ti-6Al-4V alloy worn by the same counterface in air is given in **Fig 5.23a.** It is seen that the material on the worn surface was not the same as the oxidized material on the unworn area. The worn area illustrates that at least a thin layer of the oxidized surface formed on the surface of TO-treated Ti-6Al-4V alloy was removed during sliding between two contact surfaces. The same mechanism took place for the counterface, besides the flattened curve and abrasive wear occurred here as well (**Fig 5.23b**). The debris transferred from the surface or from the ball was observed to accumulate in the sliding direction.

The wear track of TO-treated sample tested against the same material counterface in high vacuum was free of deformation and only a small amount of debris was generated (**Fig 5.24a**). The worn surface exhibited presence of oxidized islands (**Fig 5.24b**). The flattened area of the worn counterface was almost 3 times smaller than the one in air. The secondary electron micrograph presented in **Fig 5.24c** shows the worn area of the counterface. **Fig 5.25** exhibits the EDS analysis of the worn surface of sample. The EDS analysis of the contact surface of the counterface exhibited presence of oxidized material (**Fig 5.26a**). Some oxidized debris was detected around the worn area as well (**Fig 5.26b**).

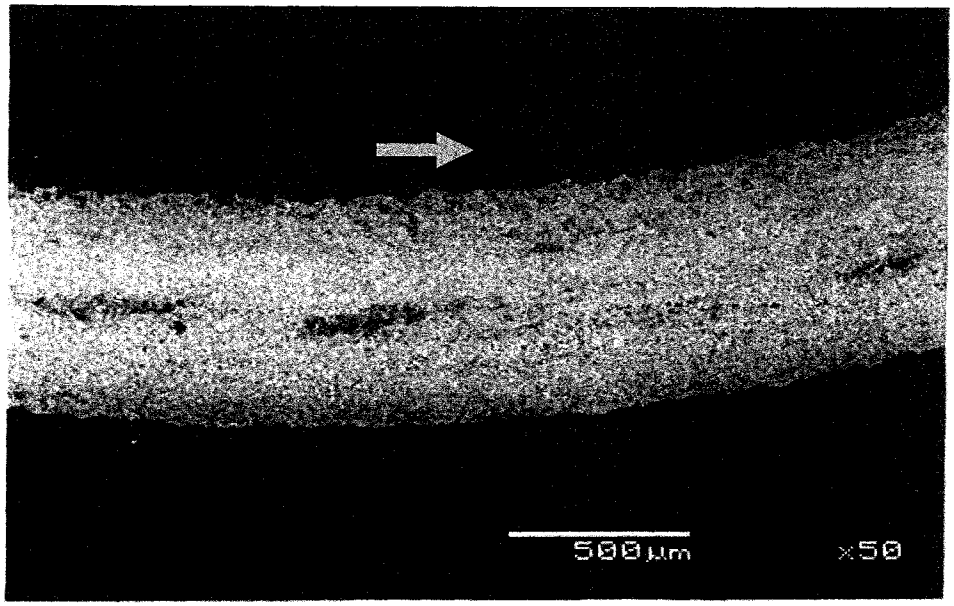

(a)

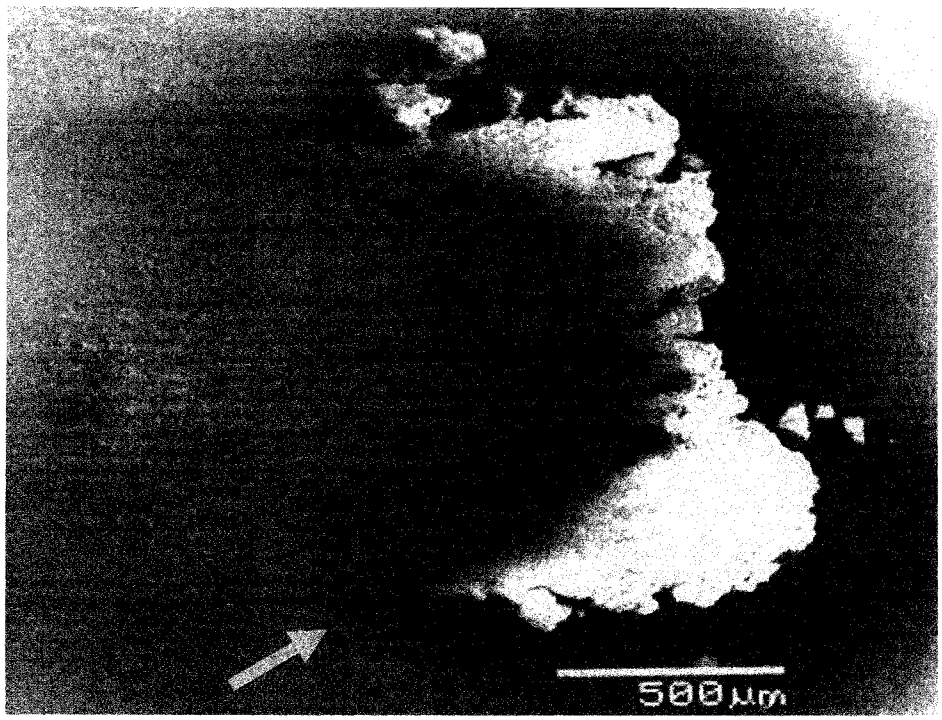

(b)

Figure 5.23 (a) Backscattered SEM micrograph of surface of TO-treated Ti-6Al-4V alloy slid against ball of TO-treated Ti-6Al-4V alloy in ambient air, (b) secondary SEM micrographs of ball of TO-treated Ti-6Al-4V alloy slid against disk of TO-treated Ti-6Al-4V alloy in ambient air. [Arrows show the sliding direction]

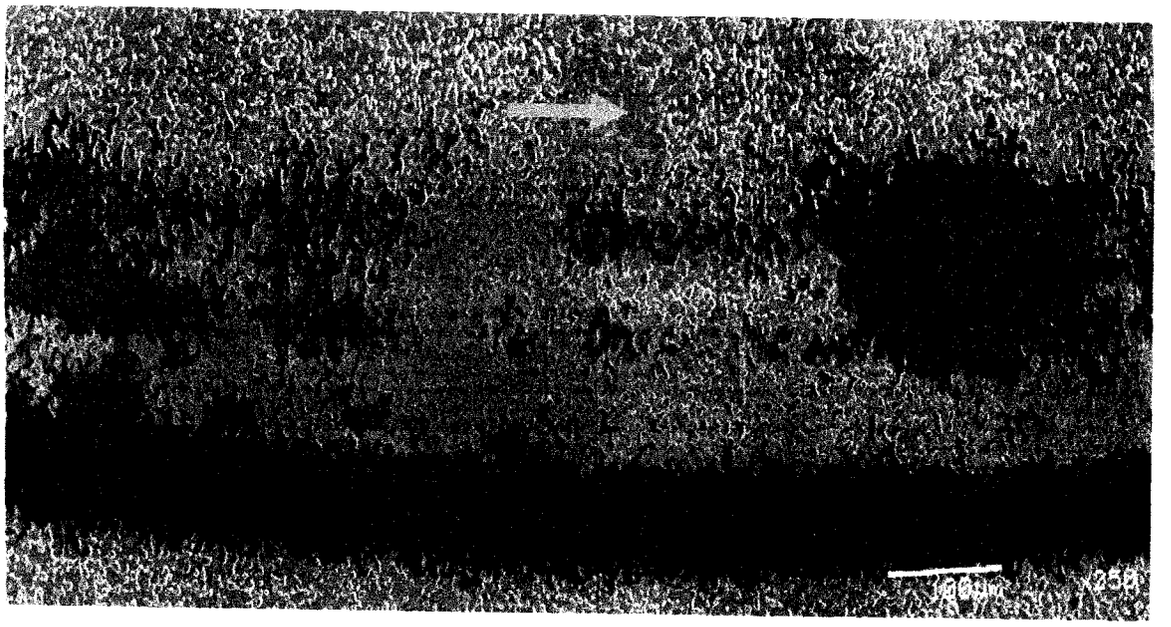

(a)

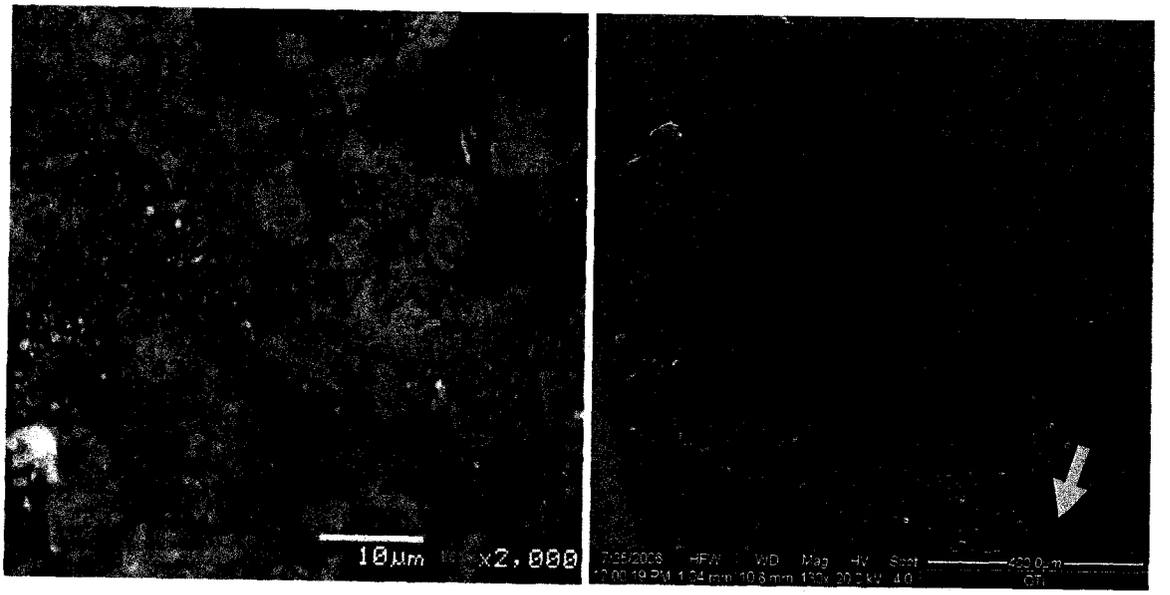

(b) (c)

Figure 5.24 (a) Secondary SEM micrographs of worn surface of TO-treated Ti-6Al-4V alloy slid against ball of TO-treated Ti-6Al-4V alloy in vacuum of 7×10^{-6} torr, (b) secondary SEM images of contact area of counterface of TO-treated Ti-6Al-4V alloy, (c) higher magnification of contact area of TO-treated sample [Arrows show the sliding direction]

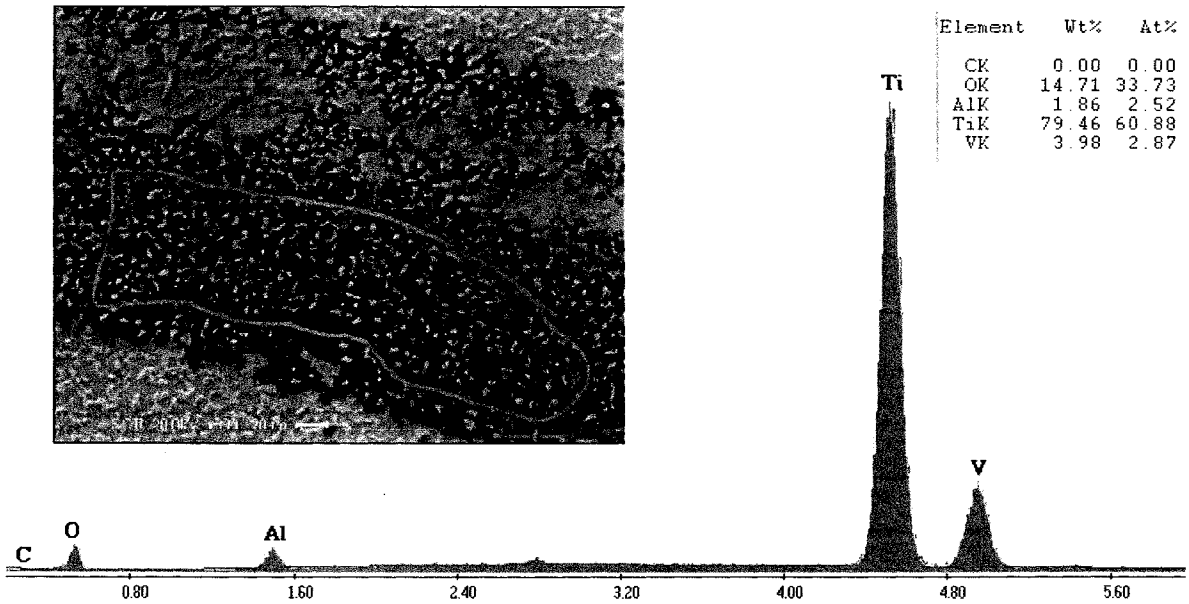

Figure 5.25 EDS analysis of TO-treated Ti-6Al-4V alloy sample slid by the same material counterface in vacuum of 7×10^{-6} torr for two different regions on worn surface.

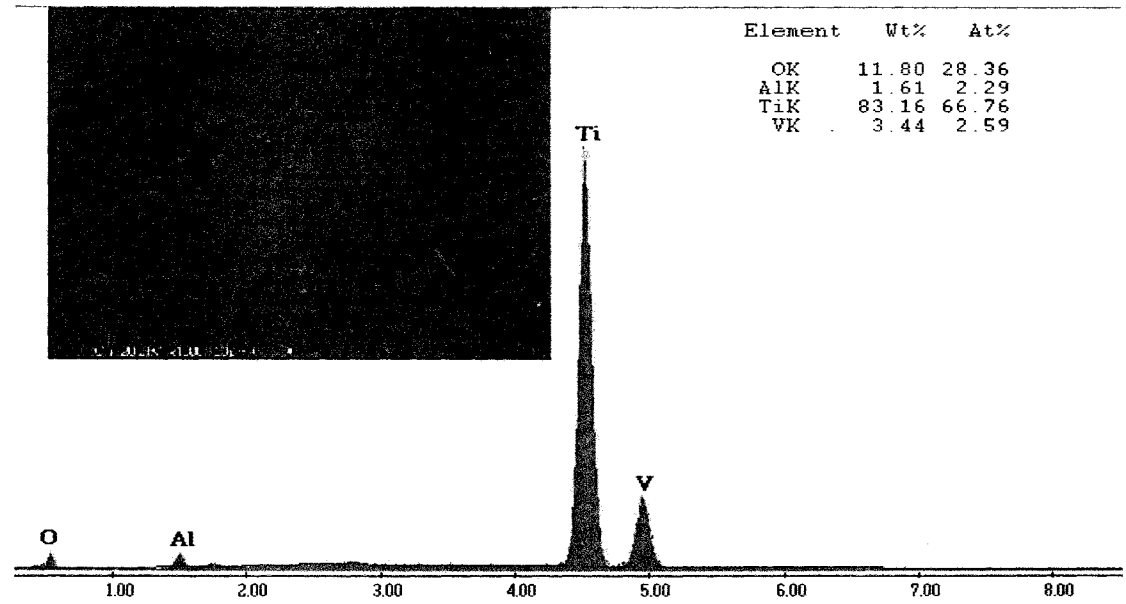

(a)

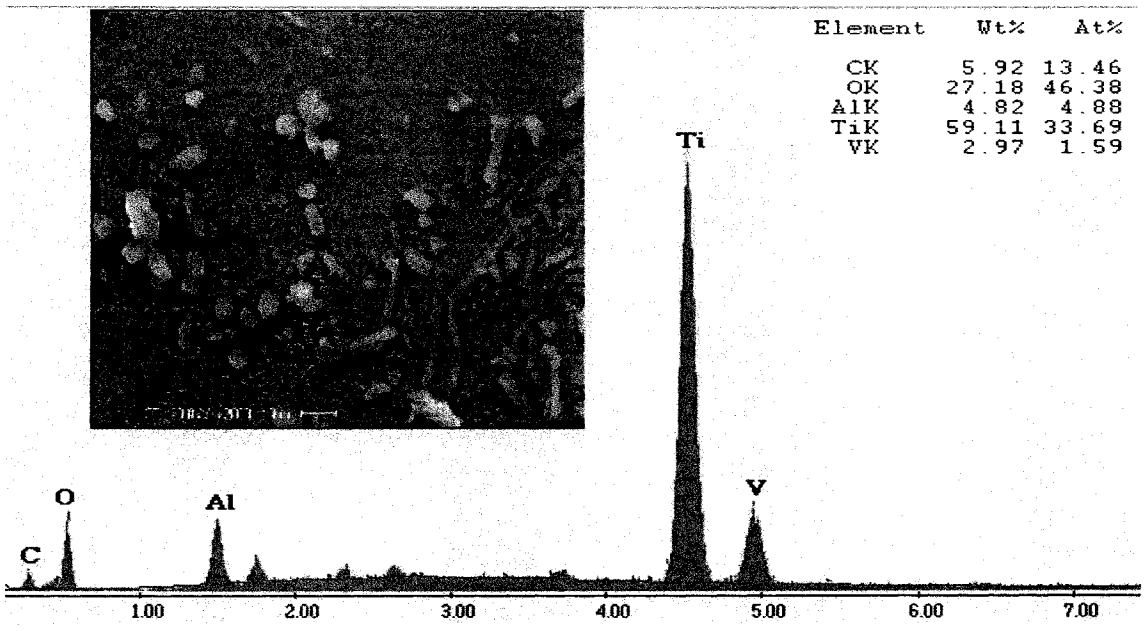

(b)

Figure 5.26 EDS analysis of TO-treated Ti-6Al-4V alloy counterface slid on the same material sample in vacuum of 7×10^{-6} torr (a) the contact surface, (b) some debris around the contact surface.

CHAPTER VI
DISCUSSION

6.1. Dry Sliding Wear of Ti-6Al-4V Alloy against 52100 Steel Ball in Ambient Air and at 7×10^{-6} torr

In ambient air the major wear mechanism of the Ti-6Al-4V worn by 52100 steel ball seems to be the oxidative wear. Very small oxidized debris particles ($\leq 1\mu m$), which in some cases agglomerated to each other and formed relatively large spongy shape particles, support this type of wear mechanism. Oxidations in ambient air at low velocity and low load have been reported in previous papers [13, 14, 51, 73]. SEM images (**Fig 5.11**) show that damage consistent with abrasion type damage on wear track occurred on the mating surfaces as well. According to the COF of Ti-6Al-4V alloy against the 52100 steel counterface, the abrasive wear and formation of oxidized particles occurred during first 30 m of sliding. Then, the contact takes place between relatively hard particles of oxidized on the surface and contact surface of counterface, and COF reaches the steady-state (**Fig 5.7**). As the oxidized particles become dispersed over the sample, a few oxidized particles have been seen to remain adhered to the contact surface of counterface. The same process took place during sliding of Ti-6Al-4V against itself. However, the flattened worn area on the counterface was covered with oxidized particles. The COF raised immediately to 0.80±0.10 and stayed there until the end of the test. The wear rate obtained from the volumetric wear damage (**Eq.4-1**) for this sliding process is higher than the wear rate obtained for former mating surfaces (Ti-6Al-4V alloy worn by 52100 steel counterface). This might be attributed to mechanically hardened subsurface of titanium alloy in contact with relatively higher hardness of 52100 steel [51]. Thus, the wear rate of Ti-6Al-4V alloy worn by 52100 steel ball is 56% less than that of obtained for the Ti-6Al-4V alloy worn by itself.

In high vacuum severe plastic deformation took place during the wear of Ti-6Al-4V against both 52100 steel and Ti-6Al-4V counterfaces. The metallic plate-like debris was formed during the sliding process. Presence of this metallic debris is usually attributed to crack formation in subsurface region of Ti-6Al-4V alloy although in this

work no crack was found in subsurface worn area in vacuum. It was observed that a slip-stick phenomenon occurred on the worn surface of Ti-6Al-4V tested in vacuum. As described by Buckley [21], in vacuum, if adhesive junction is stronger than the cohesive bonds initiated between two surfaces, the formation of the adhesive wear may start in the junction of the naturally weakest regions in materials. However, sliding damage between two contact surfaces commences a shear stress is exerted on the metal along the slip planes (or bands). As this happens, fracture occurs along these bands with the result that metal is pulled up and a surface bump is created. As sliding on the surface continues, the bumps formed may be removed by the counterface. On the other hand, it has been reported that, titanium alloys high ductility, which gives rise to the strong tendency to adhesion. Therefore, the adhesion strength of the junctions formed maybe higher than the strength of Ti-6Al-4V [17-18]. **Fig 5.18a** and **Fig 5.18b** demonstrate massive plastic deformation in the subsurface area below the wear track. The β-phase which makes 30% of total alloy composition becomes much thinner and formed layers that can not be distinguished from α-phase in the region adjacent to the contact surface. The effect of deformation decreased as layers are farther away the contact surface. Despite from highly deformed surfaces, mass loss in high vacuum is significantly less than those obtained in ambient air. The surface damage by deformation is significant but not as much loose debris was formed as in oxidative wear.

The metallic plate-like debris particles generated were transferred to the counterface, then after some rotation they smeared back on contact area of counterface. Apparently, after transferring the material to the contact surface of counterface, this material acted as an obstacle (a buffer) between the counterface and the sample. The real contact area was reduced between transferred material and wear track of the sample. The EDS confirmed that the material transferred to the contact area of counterfaces was rich in Ti, Al, and V. Therefore, it is safe to say that sliding process that happened in vacuum was between two Ti-6Al-4V surfaces. The SEM images of counterfaces slid on untreated Ti-6Al-4V alloy in vacuum display high amount of transferred material from the untreated sample of Ti-6Al-4V to the surface of the counterface (**Fig 5.12b** and **5.21b**). The coefficient of friction between the contact surfaces increased after a relatively thick

layer of material transferred on the counterface in vacuum (**Fig 5.7b** and **Fig 5.9b**). Adhesion mechanism was reported previously at high sliding speed in vacuum [51]. This work showed that the adhesion interaction in the contact area can take place even in low sliding speeds and low loads in vacuum.

6.2. Dry Sliding Wear of TO-treated Ti-6Al-4V Alloy against 52100 Steel Ball in Ambient Air and at 7×10^{-6} torr

In comparison to severe wear accompanied with the high plastic deformation in the case of dry sliding of Ti-6Al-4V alloy on 52100 steel, mild wear occurred on the contact surface of TO-treated sample tested in ambient air and vacuum. This improvement is related to formation of hard TiO_2 on the disks as reported earlier [4-5, 17-18]. The Secondary SEM images and EDS analyses of the TO-treated Ti-6Al-4V showed that the contact area was oxidized and had some adhered and smeared fragments transferred from the counterface. Therefore, if the sliding process takes place between the oxide layer (hardness= 700 KH) and 52100 steel (hardness=62 HRc), thus a considerable plastic deformation of the softer metal can be observed [73].

In contrast to the untreated Ti-6Al-4V, TO-treated Ti-6Al-4V alloy showed lower volumetric wear damage in both atmospheric conditions. However, TO-treated Ti-6Al-4V tested against 52100 steel experienced higher wear rates than untreated Ti-6Al-4V worn by 52100 steel in high vacuum.

Although the effect of adhesion was eliminated due to thermal oxidization treatment, and lower volumetric wear damage obtained for the treated samples, damage to 52100 counterface by shearing or tearing of the surface in both atmospheric condition. This was worse in high vacuum than in air. Considering the total damage to the tribo-system, increasing the wear resistance of TO-treated Ti-6Al-4V alloy to be used against a 52100 steel counterface was not a satisfactory achievement from an engineering point of view. So, a ferrous counterface is not suitable for vacuum tribological application of TO-treated Ti-6Al-4V, and another counterface required

6.3. Dry Sliding Wear of TO-treated Ti-6Al-4V Alloy against TO-treated Ti-6Al-4V Alloy Ball in Ambient Air and at 7×10^{-6} torr

The wear mechanism in ambient air in this ball-on-disk configuration was including abrasive. In comparison to the sliding 52100 steel counterface on TO-treated Ti-6Al-4V in air, the TO-treated Ti-6Al-4V experienced higher the wear rate and volumetric wear damage in contact with itself in air (**Fig 5.1a** & **Fig 5.3a**). The contact areas of both surfaces encountered layer removal as these illustrated on secondary SEM micrographs images of sample and counterface (**Fig 5.23**). It should be noticed that high hardness, excellent melting point, relatively low ductility, and high resistivity give a ceramic-like performance to the TiO_2. Therefore, it is not surprising to observe the high COF during the sliding between mating surfaces as well as high wear rate in ambient air. The obtained results for sliding of above mating surfaces correlated with those one that reported for ceramic/ceramic sliding process [74]. Sliney, H. E. et al [74] reported high coefficient of friction between (0.5-1.0), and relatively high wear rates for particularly oxide ceramics sliding on each other. However, COF found that the sliding of TO-treated Ti-6Al-4V was slightly higher than that observed for sliding of 52100 steel counterface on thermally oxidized Ti-6Al-4V in ambient air.

Under vacuum condition, the TO-treated Ti-6Al-4V tested against itself showed high wear resistance. The wear rate was lower than those obtained in air. This amount of wear rate was the same as the wear rate of TO-treated Ti-6Al-4V worn by 52100 steel counterface in ambient air. The oxidized islands on the sample were affected during the sliding as surface roughness of wear track increased. Yet, the morphology of the surface is preserved after the sliding process. However, the flattened area at the tip of TO-treated Ti-6Al-4V counterface has micrograph less radius in comparison to the worn surface of TO-treated Ti-6Al-4V counterface in ambient air. The mass loss of counterface was undetectable with the analytical scale. The abrasive area on the flattened area of the ball is observed on flattened surface of counterface (**Fig 5.24**). Therefore, the configuration of TO-treated Ti-6Al-4V disk against itself under low atmospheric pressure (7×10^{-6} torr) demonstrates improvement in wear resistance of TO-treated Ti-6Al-4V disk while lower wear observed on the counterface.

6.4. Summary of the Results

The next four tables represent all the results that were obtained throughout the tests:

Table 6.1 Results for wear of 52100 steel ball against Ti-6Al-4V alloy sample.

Sample: Ti-6Al-4V alloy, Counterface: 52100 Stainless Steel, Normal Load:2N, Sliding Velocity:0.05 m/s			
		Air	Vacuum ($6–8\times10^{-6}$)
Worn Surfaces	Samples (SEM, WYKO)	Area covered by oxide:40% Oxidized spread out over the worn surface Abrasive wear observed on the track	No oxidation observed Severe plastic deformation Abrasion seen on the surface
	Counterface (SEM)	Oxidized debris scatteredly adhered to the ball	Layers of Ti-alloy adhered on the surface of the ball
Wear Debris	Colour	Black/Spongy	Shiny and Metallic
	Size(arbitrary size)/Shape	$20\times15\ \mu m^2$	Plate-like $80\times60\ \mu m^2$
	XRD	N/A	N/A
Surface (sample)	XRD	α-Ti and some β-Ti	α-Ti and some β-Ti
Worn surface (sample)	EDS	N/A	Ti, Al, V, and No O
Worn surface (ball)	EDS	N/A	Adhered at the tip of the ball: Ti, Al, V
Wear Rate (mm^3/M)	Sample	0.00124	0.000267
Volumetric Wear damage	Sample (mm^3)	0.5517	0.0327
Weight loss (g)	Counterface	N/A	N/A or very small
COF (Steady State)	Ball-on-Disk	0.6	0.45
Roughness (μm)	Initial Surface	0.024	0.058
	Worn Surface	3.4	5.58
Width of wear track (mm)		0.766	0.342

Table 6.2 Results for wear of 52100 steel ball against TO-treated Ti-6Al-4V sample.

Sample: TO-treated Ti-6Al-4V alloy, Counterface: 52100 Stainless Steel, Normal Load:2N, Sliding Velocity:0.05 m/s			
		Air	Vacuum ($6\sim8\times10^{-6}$)
Worn Surfaces	Samples (SEM, WYKO)	Patches of oxide material from counterface adhered on the wear track	Abrasive wear is easily detectable
	Counterface (SEM)	Oxidized material materials transferred to the flattened surface of the ball	Oxidized material materials transferred to the flattened surface of the ball The flattened area is larger here
Wear Debris	Colour	N/A	N/A
	Size(arbitrary size)/Shape	N/A	N/A
Oxidized Surface	XRD	Rutile and a few Anastile (TiO2)	Rutile and a few Anastile (TiO2)
Worn surface (sample)	EDS	Ti, Al, and V, O and some Fe	Ti > Fe > Al ≥ V, and O
Worn surface (ball)	EDS	N/A	Fe >Ti >Al ≥ V, and O
Wear Rate (mm^3/M)	Sample	$9.4*10^{-5}$	N/A
Volumetric wear damage	Sample	0.07676	0.0524
Weight loss (g)	Counterface	0.004	0.006
COF (Steady State)	Ball-on-Disk	0.8	0.9
Roughness (μm)	Initial Surface	0.156	0.161
	Worn Surface	N/A	0.202
Wear Mechanism	Ball-on-disk configuration	Abrasive and Oxidative wear	Severe damage along with Abrasive Wear
Width of wear track (mm)		0.4	0.342

Table 6.3 Results for wear of Ti-6Al-4V alloy ball against Ti-6Al-4V alloy sample.

Sample: Ti-6Al-4V alloy, Counterface: Ti-6Al-4V alloy, Normal Load:2N, Sliding Velocity:0.05 m/s			
		Air	Vacuum ($6\sim8\times10^{-6}$)
Worn Surfaces	Samples (SEM, WYKO)	Oxide material scattered over the wear track They might be from counterface as well on the wear track	Severe Plastic Deformation The same as steel on Ti-alloy Abrasion seen on the surfaces
	Counterface (SEM)	Oxidized Particles all over the flattened area of ball	Layers of Ti-alloy adhered on the surface of the ball
Wear Debris	Colour	Spongy/Brown or black	Shiney and mettalic
	Size(arbitrary size)/Shape	Diameter (average): 5 μm	Plate-Like100×50 μm^2
Surface (sample)	XRD	α-Ti and some β-Ti	α-Ti and some β-Ti
Worn surface (sample)	EDS	Ti, Al, and V, O	Ti, Al, and V
Worn surface (ball)	EDS	Ti, Al, and V, O	Ti, Al, and V
Wear Rate (mm^3/M)	Sample	N/A	0.00071
Volumetric Wear damage	Sample	0.8966	0.341
Weight loss (g)	Counterface	0.0004	It gained weight:0.0004
COF (Steady State)	Ball-on-Disk	0.45	0.3
Roughness (μm)	Initial Surface	0.039	0.026
	Worn Surface	1.6	3.42
Width of wear track (mm)		0.901	0.654

Table 6.4 Results for wear of TO-treated Ti-6Al-4V ball against TO-treated Ti-6Al-4V sample.

Sample: TO-treated Ti-6Al-4V alloy, Counterface: TO-treated Ti-6Al-4V alloy, Normal Load:2N, Sliding Velocity:0.05 m/s				
			Air	Vacuum ($6\sim8\times10^{-6}$)
Worn Surfaces	Samples (SEM, WYKO)		Thin layer of surface has beem removed / Distorted islands observed	smaller area were distorted Trace of islands are still existed
	Counterface (SEM)		The tip of counterface has been flattened / Patches of transferred material adhered (hammered) piled up on the surface of the ball	Smallest flattened region after test observed some materials transferred and adhered to flattened area
Wear Debris		Colour	Black	N/A
		Size(arbitrary size)/Shape	Spherical	N/A
Surface (sample)	XRD		Rutile and a few Anastile (TiO2)	Rutile and a few Anastile (TiO2)
Worn surface (sample)	EDS		Ti, Al, and V, O	Ti, Al, V, O, and C
Worn surface (ball)	EDS		N/A	Ti, Al, V, O
Wear Rate (mm^3/m)	Sample		N/A	0.00094
Volumetric Wear damage			0.704	0.0236
Weight loss (g)	Counterface		N/A	N/A
COF (Steady State)	Ball-on-Disk		0.75	0.25
Roughness (μm)	Initial Surface		0.103	0.161
	Worn Surface		0.182	0.337
Wear Mechanism	Ball-on-disk configuration		Abrasive and Oxidative wear	Very low wear or mild wear
Width of wear track (mm)			0.83	0.27

CHAPTER VII
CONCLUSIONS

The main objectives of the present study were to investigate the wear mechanisms and friction behaviour of Ti-6Al-4V alloy in order to assess whether an increase in the wear resistance of Ti-6Al-4V can be achieved under low atmospheric pressure. Thus, thermally oxidized Ti-6Al-4V alloy samples were obtained by heat treating samples with polished surfaces at 600 °C and for 60 hours. Two counterfaces of 52100 steel and Ti-6Al-4V were selected to be used in the dry sliding wear tests of thermally oxidized Ti-6Al-4V alloy.

A special apparatus was needed to explore the wear mechanisms, wear rate and trend of coefficients of friction under vacuum. Therefore, a ball-on-disk system was designed and constructed for this project. The system was built in such a way that could run at high vacuum of 7×10^{-6} torr. For comparison tests were conducted in ambient air as well. The applied load of 2N at the sliding velocity of 0.05m/s was constant for all the tests. Based on analyses of SEM, EDS, XRD investigations as well as the COF, hardness and roughness measurements of contact surfaces, the observed wear rates obtained and could be rationalized. The following conclusions were drawn, and with respect to the vacuum tribological behaviour categorized in four subsections:

7.1. Dry Sliding Wear of Untreated Ti-6Al-4V on Untreated Ti-6Al-4V Alloy in High Vacuum:

1. Severe plastic deformation in the form of a "slip-stick" behaviour characterized untreated Ti-6Al-4V alloy run against 52100 steel or Ti-6Al-4V alloy.
2. Transferred material from Ti-alloy to the surface of counterfaces in early stages of sliding cause damage by adhesion due to bonding between mating surfaces.
3. Existence of plate-like debris on the worn area of Ti-6Al-4V samples might be attributed to occurrence of delamination wear even in low loads and low sliding velocities.

7.2. Dry Sliding Wear of Thermally Oxidized Ti-6Al-4V Alloy in High Vacuum:

1. Low wear rate and small weight loss of TO-treated Ti-6Al-4V demonstrated that an improvement occurred in the wear resistance of TO-treated Ti-6Al-4V alloy in high vacuum.

2. The material transfer occurred from TO-treated Ti-6Al-4V to 52100 steel counterface. Large flattened areas observed on the contact surface of counterface showed that 52100 steel was not a good choice for dry sliding of the TO-treated Ti-6Al-4V. The high hardness of thermally oxidized sample is the major cause for high wear of the tip of the counterface.

7.3. Dry Sliding Wear of TO-treated Ti-6Al-4V Alloy against TO-treated Ti-6Al-4V Alloy in High Vacuum:

1. The TO-treated Ti-6Al-4V alloy counterface had the smallest worn area compared to other counterfaces in various testing conditions. The wear rate was negligible.

2. The worn surface of the TO-treated Ti-6Al-4V sample was very small and the islands of oxidized material (mostly TiO_2) were hardly detectable. This suggested that thermal oxidization method that made Ti-6Al-4V more wear resistant used in ambient air and corrosion media can be successfully applied in high vacuum tribological conditions as well.

7.4. Comparison of Air and Vacuum Tribological Properties of TO-treated Ti-6Al-4V

1. The wear rates of TO-treated Ti-6Al-4V against ferrous material in air and vacuum are small. However, the value of wear rate was less in air compared to the result obtained in vacuum.
2. Sliding of TO-treated Ti-6Al-4V against itself in air exhibited high wear rates although the wear rate in vacuum was drastically decreased. The latter value of wear rate is similar to that obtained against ferrous material in air.

Future Work

In order to continue research on enhancement of wear properties for Ti-6Al-4V alloy, following suggestions present here:

1. The wear resistance of TO-treated Ti-6Al-4V should be tested under lower atmospheric pressure as well as different varieties of gases including N, Ar, etc...

2. A better way of oxidization should be considered to attain sufficient thickness for Ti-6Al-4V counterface.

3. The other non-ferrous material should be tested as counterfaces to study the wear mechanisms of TO-treated Ti-6Al-4V alloy in contact with mentioned material under low atmospheric pressure.

4. To avoid effect of carbon that was initiated from the oil of diffusion pump during the sliding under evacuation, a more reliable pump such as should be used for vacuum system.

REFERENCES

[1] I. I. Garbar, Gradation of oxidational wear of metals, Tribology International 35, p.749-755 (2002).

[2] F. H. Stott, The role of oxidation in the wear of alloys, Tribology International, Vol.31, Nos.1-3, p.61-71 (1998).

[3] T. F. J. Quinn, Role of oxidation in mild wear of steel, Brit. J. Appl. Phys., 13, p.33-37 (1962).

[4] H. Guleryuz, and H. Cimenoglu, Effect of thermal oxidation on corrosion and corrosion-wear behaviour of a TI-6Al-4V alloy, Biomaterials 25 p.3325-3333 (2004)

[5] J. Komotori, B. J. Lee, H. Dong, and P. A. Dearnley, Corrosion response of surface engineering titanium alloys damaged by perior abrasion, Wear 251 p.1239-1249 (2001)

[6] T. F. J. Quinn and W. O. Winer, The thermal aspects of oxidational, Wear, 102, No.1-2, p.1-160 (1985).

[7] M. F. Ashby, J. Abulawi and H. S. Kong, Temperature maps for frictional heating in dry sliding, Tribology Transactions, Vol.34,4, p.577-587 (1991).

[8] I. M. Hutchings, Trobology: Friction and wear of engineering materials, London: CRC Press, 1992.

[9] H. So, The mechanism of oxidational wear, Wear 184, p.161-167 (1995).

[10] K. Hiratsuka, Y. Ando, and A. Sugahara, Effect of atmospheric oxygen on the enhancement of a growth process of transfer particles in adhesive wear, Journal of JSLE International Edition, p.33-38 (1999).

[11] W. Hirst and J. K. Lancaster, The influence of speed on metallic wear, Proc. Roy. Soc.A, Vol.295, p.228-241 (1960).

[12] K. G. Budinski, Tribological properties of titanium alloys, Wear 151 (1991) 203-217.

[13] G. Straffelini and A. Molinari, Dry sliding wear of Ti-6Al-4V alloy as influenced by the counterface and sliding conditions, Wear, Vol.236, p.328-338 (1999).

[14] Y. Liu, D. Z. Yang, S. Y. He, and W. L. Wu, Microstructures developed in the surface layer of Ti-6Al-4V alloy after sliding wear in vacuum, in Materials Characterization, Vol.50 p.275-279 (2003).

[15] H. Dong and T. Bell, Enhanced wear resistance of titanium surfaces by a new thermal oxidation treatment, Wear 238, p.131-137 (2000).

[16] H. Dong, A. Bloyce, T. Bell, and P. H. Morton, Surface engineering to improve tribological performance of Ti-6Al-4V,Surface Engineering 13 p.402-406 (1997).

[17] H. Guleryuz, and H. Cimenoglu, Surface modification of a Ti-6Al-4V alloy by thermal oxidation, Surface and Coating Technology 192 p.164-170 (2005).

[18] F. Boorgioli, E. Galvanetoo, F. Iozzeli, G. Pradelli, Improvement of wear resistance of Ti-6Al-4V alloy by means of thermal oxidation, Material Letters 59 p.2159-2162 (2005).

[19] D. H. Buckley, The influence of various physical properties of metals on their friction and wear behaviour in vacuum, Metals Engineering Quarterly, American Society For Metals, p. 44-53, May (1967).

[20] F. P. Bowden and D. Tabor, The Friction and Lubrication of solids, Clarendon Press, Oxford p.337 (1950)

[21] D. H. Buckley, Adhesion, friction, wear and lubrication in vacuum, Japan. J. Appl. Phys. Suppl. 2, p.297-304 (1974).

[22] T. Sasada, S. Norose, and J. Nagai, Wear in different metal combinations in vacuum, The 21st Japan Congress on Material Research- Metallic Material, p. 112-116, May (1978).

[23] T. Akagaki, and D. A. Rigney, Sliding friction and wear of metals in vacuum, Wear of Materials, ASME, p. 265-275 (1991).

[24] S. Venkatesan and D. A. Rigney, Sliding friction and wear of plain carbon steels in air and vacuum, Wear 153, p.163-178 (1992)

[25] H. Kong, E-S. Yoon and O. K. Kwon, Self-formation of protective oxide films at dry sliding mild steel surfaces under a medium vacuum, Wear Vol.181-183, p.325-333 (1995).

[26] A. Edrisy, "Investigation of Wear and Scuffing Behaviour of Ferrous Thermal Spray Coatings for Aluminum Engines," PhD Dissertation, University of Windsor p.3-8 (2004).

[27] J. F. Archard and W. Hirst, The wear of metals under unlubricated conditions, Proc. Roy. So.A, Vol.236, p.379-393 (1956).

[28] S. C. Lim and M. F. Ashby, Wear-mechanism maps, Acta Metall, 35, No1, p.1-24 (1987).

[29] W. Hirst and J. K. Lancaster, Surface film formation and metallic wear, J. Appl. Phys. 27, p.1057-1065 (1956)

[30] A. Edrisy, and A. T. Alpas, Microstructures and sliding wear resistances of 0.2% carbon steel coatings deposited by HVOF and PTWA thermal spray processes, Thin Solid Films 420-421, p.338-344 (2002).

[31] A. Edrisy, T. Perry, and A. T. Alpas, Investigation of scuffing damage in aluminum engines with thermal spray coatings, Wear 259, p.1056-1062 (2005).

[32] N. P. Suh, The delamination theory of wear, Wear 25, p.111-124 (1973).

[33] N. P. Suh, S. Jahanmir, D. A. Colling and E. P. Abrahamson, The delamination theory for wear of metals sliding at low speeds, Alberta Research Council, Information Series, p 117-127 (1974).

[34] J. Zhang and A. T. Alpas, Transition between mild and severe wear in aluminium alloys, Acta Mater, 45, No.2, p.513-528 (1997).

[35] I. I. Garbar, Critical Structure of metal destruction under the process of wear, Journal of Tribology, Vol.122, p.361-366 (2000).

[36] I. I. Garbar, The effect of load on the structure and wear of friction pair materials (example of low-carbon steel and copper), Wear 205, p.240-245 (1997).

[37] G. E. Dieter, Mechanical Metallurgy (SI Metric Edition, Third Edition, McGraw-Hill Book Company, London, 1988).

[38] T. Sasada, S. Norose and H. Mishina, The behaviour of adhered fragments interposed between sliding surfaces and the formation process of wear particles, Journal of Lubrication Technology, 103, p.195-202 (1981).

[39] K. N. Tandon and X. Y. Li, Wear debris characrization of Al-Si alloys sliding agains steel under wear conditions, Seripta Materialia, 38, No. 1, p.7-13 (1998)

[40] E. de Wit, L. Froyen and J. P. Celis, Oxidation reaction during sliding wear influencing the formation of either amorphous or nanocrystalline debris, Wear, 231, p.116-123 (1999)

[41] M. A. Moore, R. C. D. Richardson, and D. G. Attwood, The limiting strength of worn metal surfaces, Metallurgical Transactions, 3, p.2485-2491 (1972).

[44] J. Zhang and A. T. Alpas, Delamination wear in ductile materials containing second phase particles, Material Science and Engineering, A.160, p.25-35 (1993).

[42] K. Hiratsuka and M. Goto, The role of changes in hardness of subsurfaces, transfer particles and wear particles in initial-steady wear transition, Wear, Vol.238, p.70-77 (2000).

[43] T. Sasada, S. Norose, and J. Nagai, Wear in different metal combinations in vacuum, mmm p.112-116 (1982).

[45] P. Heilmann, W. A. T. Clark, D. A. Rigney, Orientation determination of subsurface cells generated by sliding, Acta Metal Vol. 31, No.8, p.1293-1305 (1983).

[46] C. Perrin and W. M. Rainforth, Work hardening behaviour at the worn surface of Al-Cu and Al-Si alloys, Wear, 203-204, p.171-179 (1997).

[47] C. Kittel, Introduction to solid state physics, John Wiley and Sons, New York (1996).

[48] H. Hong, The role of atmospheres and lubricants in the oxidational wear of metals, Tribology International, 35, p.725-729 (2002).

[49] S. C. Lim, The relevance of wear-mechanism maps to mild-oxidational wear, Tribology International 35, p.717-723 (2002).

[50] T. F. J. Quinn, J. L. Sullivan and D. M. Rowson, Origins and development of oxidational wear at low ambient temperatures, Wear, 94, No.2, p.174-191 (1984).

[51] I. L. Lebedeva and G. N. Presnyakova, Adhesion wear mechanisms under dry friction of titanium alloys in vacuum, Wear, 148, p.203-210 (1991).

[52] N. Saito, Y. Hemmi, T. Arima, M. Oishi, and M. Hosokawa, Sliding wear tests of stainless steel couples in water at temperature, high sliding speed and high load, Wear, 204, p.145-154 (1996).

[53] K. Hiratsuka and K. Muramoto, Role of wear particles in severe-mild transition, Wear, 259, p.467-476 (2005).

[54] S. Wilson and A. T. Alpas, Wear mechanism maps for TiN-coated high speed steel, Surface and Coating Technology, Vol.120-121, p.519-537 (1999).

[55] S. C. Lim and J. H. Brunton, A dynamic wear rig for the scanning electron microscope, Wear, 101, p.81-91 (1985).

[56] Ye. L. Ostrovskaya, T. P. Yukhno, G. D. Gamulya, Yu. V. Vvedenskij, and V. I. Kuleba, Low temperature tribology at the B. Verkin Institute for low temperature physics & engineering (historical review), Tribology International, 32, p.265-276 (2001).

[57] T. Akagaki and D. A. Rigney, Sliding friction nd wear of metals in vacuum, in Wear of Materials, ASME, p.265-275 (1991).

[58] Y. Liu, D. Z. Yang, S. Y. He and W. L. Wu, Dry Sliding wear of Ti-6Al-4V alloy in air and vacuum, Trans. Nonferrous Met. Soc. China, Vol.13, No.5, p.1137-1140 (2003).

[59] K. Miyoshi, Aerospace mechanisms and tribology technology case study, Tribology International, Vol.32, p.673-685 (1999).

[60] P. Cong, H. Nanao, J. Imai and S. Mori, Tribology behaviour and tribochemical reactions of alumina in HFC-134a environment, Tribology International, 35, p.145-151 (2002).

[61] W. A. Glaeser, Wear experiments in the scanning electron microscope, Wear, 73, p.371-386 (1981).

[62] L. H. Chen and D. A. Rigney, Adhesion theories of transfer and wear during sliding of metals, Wear 136, p.223-235 (1990).

[63] M. Kuo and D. A. Rigney, Sliding behaviour of aluminum, Materials Science and Engineering, A157 p.131-143 (1992).

[64] K. Lepper, M. James, J. Chashechkina, and D. A. Rigney, Sliding behaviour of selected aluminum alloys, Wear 203-204 p.46-56 (1997).

[66] J. Qu, P. J. Blau, T. R. Watkins, O. B. Cavin, and N. S. Kulkarani, Friction and wear of titanium alloys sliding against metal, polymer, and ceramic counterfaces, Wear 258, p.1348-1356 (2005)

[65] M.J. Donachie, Jr. Introduction to titanium and titanium alloys, in: M. J. Donachie (Ed.), Titanium and Titanium alloys: Source Book, American Society for Metals, Ohio, p.3-10 (1982).

[67] S. R. Seagle and L. J. Bartlo, Physical metallurgy and Metallography of titanium alloys, Metals Engineering Quarterly, Vol.8, p.1-10 (1968).

[68] M. Long and H. J. Rack, Friction and surface behaviour of selected titanium alloys during reciprocating-sliding motion, Wear 249, p.158-168 (2001).

[69] http://www.msm.cam.ac.uk/phse-trans/2004/titanium/titanium.html.

[70] Y. B. Gue, Q. Wen and M. F. Hostemeyer, An internal state variable plasticity-based approach to determine dynamic loading history effects on material property in manufacturing process, International Journal of Mechanical Sciences 47, p.1423-1441 (2005)

[71] A. Molinari, G. Straffelini, B. Tesi, and T. Bacci, Dry sliding wear mechanisms of the Ti-6Al-4V alloy, Wear, 208, p.105-112 (1997).

[72] P. A. Dearnely, K. L. Dahm, and H. Cimenoglu, The corrosion-wear behaviour of thermally oxidized CP-Ti and Ti-6Al-4V, Wear 256 p.469-479 (2004).

[73] K. Miyoshi, Considerations in vacuum tribology (adhesion, friction, wear, and solid lubrication in vacuum), Tribology International 32 p. 605-616 (1999).

[74] H. E. Sliney and C. Dellacorte, The friction and wear of ceramic/ceramic and ceramic/metal combinations in sliding contact, National Aeronautics and Space Administration (NASA), Lewis Research Center, Cleveland, Ohio (1993).

APPENDICIS

APPENDIX A

THE PREPARATION OF THE PIN-ON-DISK SYSTEM FOR OPERATION

1. Place the ball in the ball-holder. Tight the screw in a way that ball merely fixed in its place.
2. Mount the Ball-holder to the long arm of ball-holder fixed in terminal.
3. Align the distance of the contact surface of the ball from center of sample by loosing and tightening the screw-sets. When the screw-sets are loosen the whole wear rig moves (except the Sample-holder). Therefore, the radius of wear track can be fixed to a desired value using the indicator next to the scale located to lower part of Pivot-holder (**Fig.1a**).
4. Put the Ball-holder arm of pin-on-disk in horizontal altitude using a level while the contact surface of ball touches the surface of sample. Level the Ball-holder arm is in such a way that the arm is parallel to the surface of the sample (disk).
5. Place the dead weight in the arm of the Ball-holder (**Fig.1b**)
6. Close the chamber.

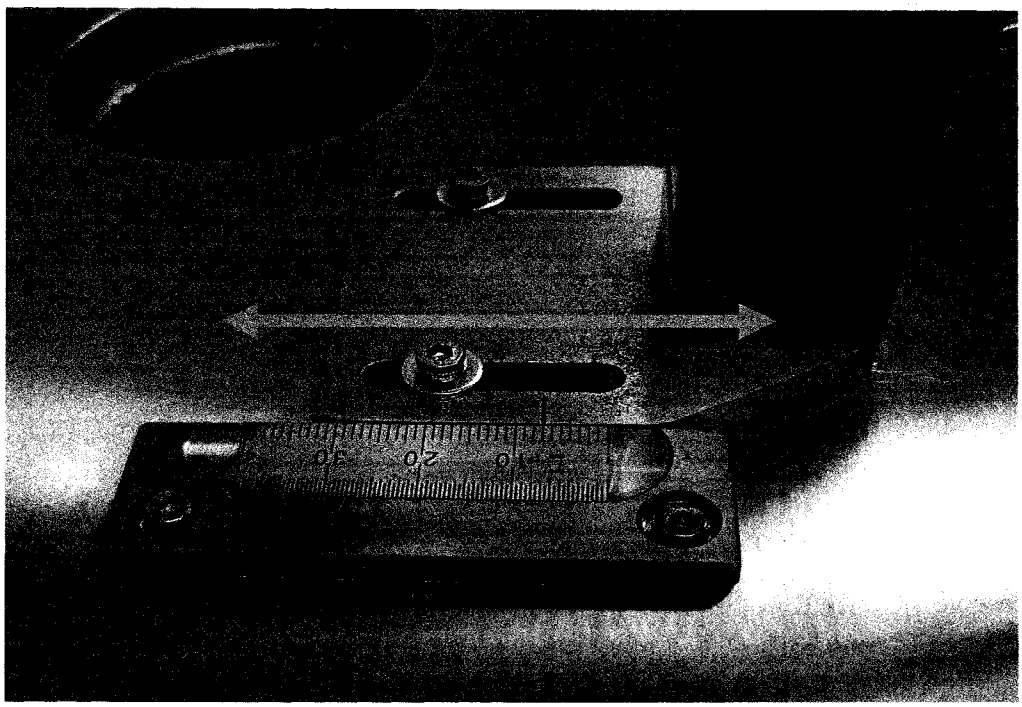

Figure 1 Screw and scale for setting a desired radius of wear track.

APPENDIX B

ATTAIN LOW ATMOSPHERIC PRESSURE INSIDE THE VACUUM CHAMBER

The procedure to achieve relatively high vacuum of 7×10^{-6} torr in side the vacuum chamber as is follow (**see Fig 3.1**):

1. All the valves except *Foreline* valve (V1) must be close.
2. Water circulation should be opened before plugging the diffusion pump cable into the electrical socket.
3. Mechanical and diffusion pump should be on.
4. While the cascade of diffusion pump is very hot, V1 should be close and *Roughing* valve (V2) must be open.
5. When the pressure inside the chamber decrease to 10^{-3} torr, V2 should be close and V1 and *High-vacuum* valve (V3), subsequently, should be open.
6. Depend on presence of water vapour molecules in side the chamber, it takes about 5 to 15 hours to reach the desire pressure inside the chamber.
7. By means of a *Needle* valve (V4) connected to argon cylinder, argon can be purged inside the chamber.

APPENDIX C

DRAWING THE MAJOR PARTS Of TRIBO-TESTER MECHANISM

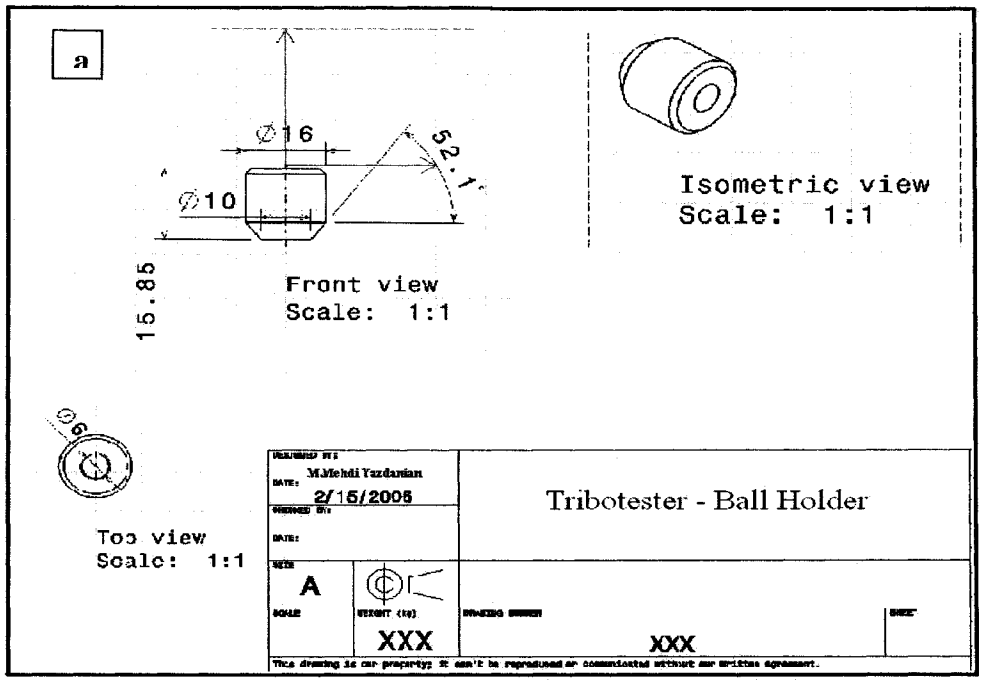

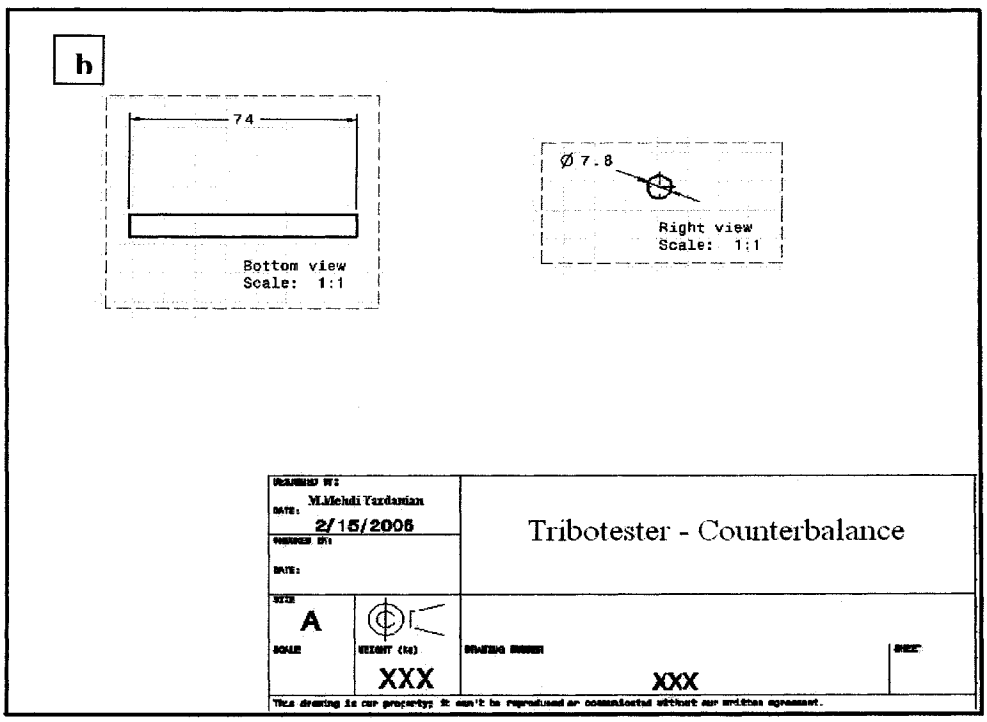

Figure.1 Tribo-tester parts: (a) Ball holder, (b) counterbalance (sizes are in mm)

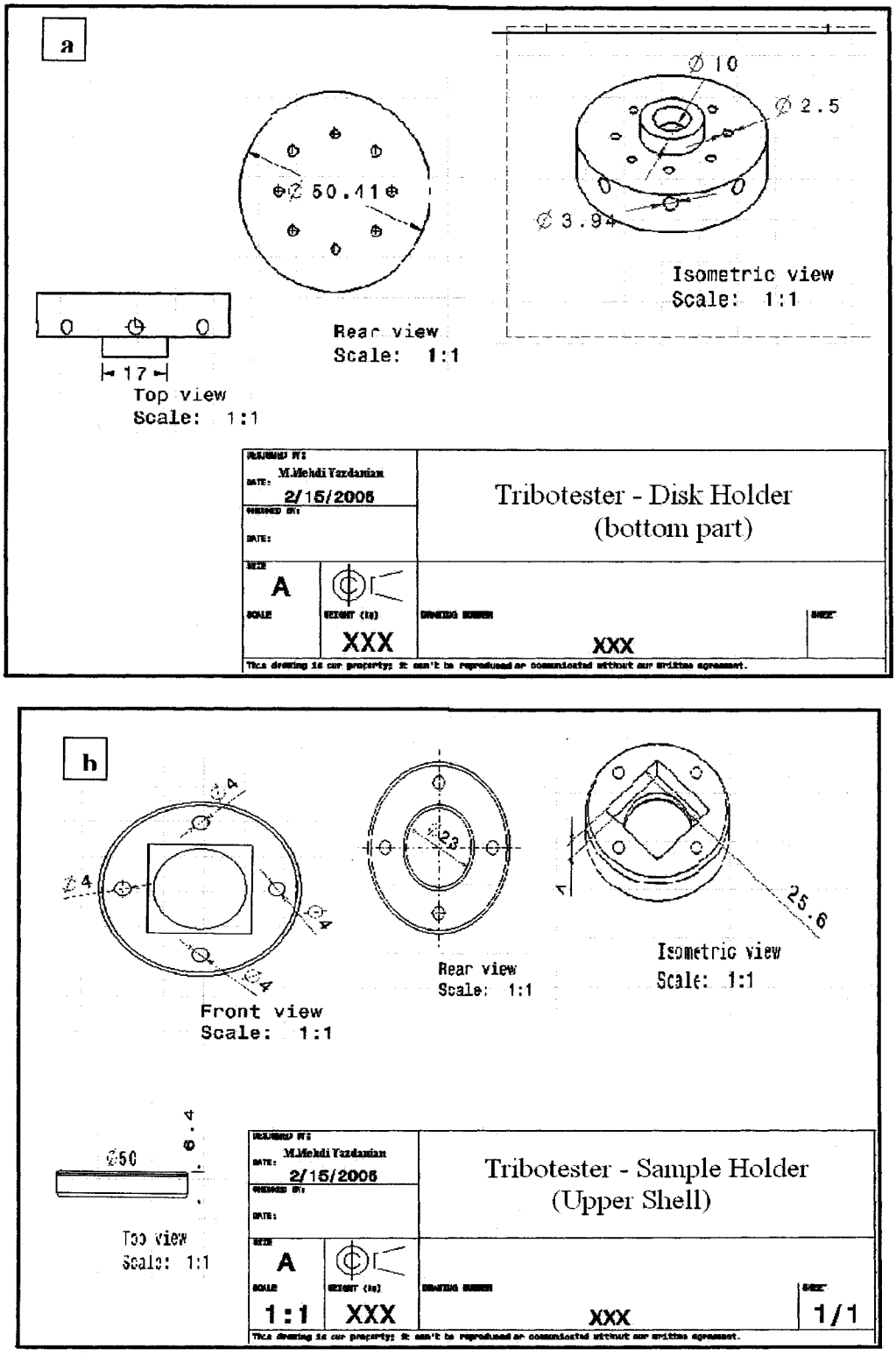

Figure.2 Tribo-tester part: Disk holder (a) bottom part, (b) upper sPell (sizes are in mm)

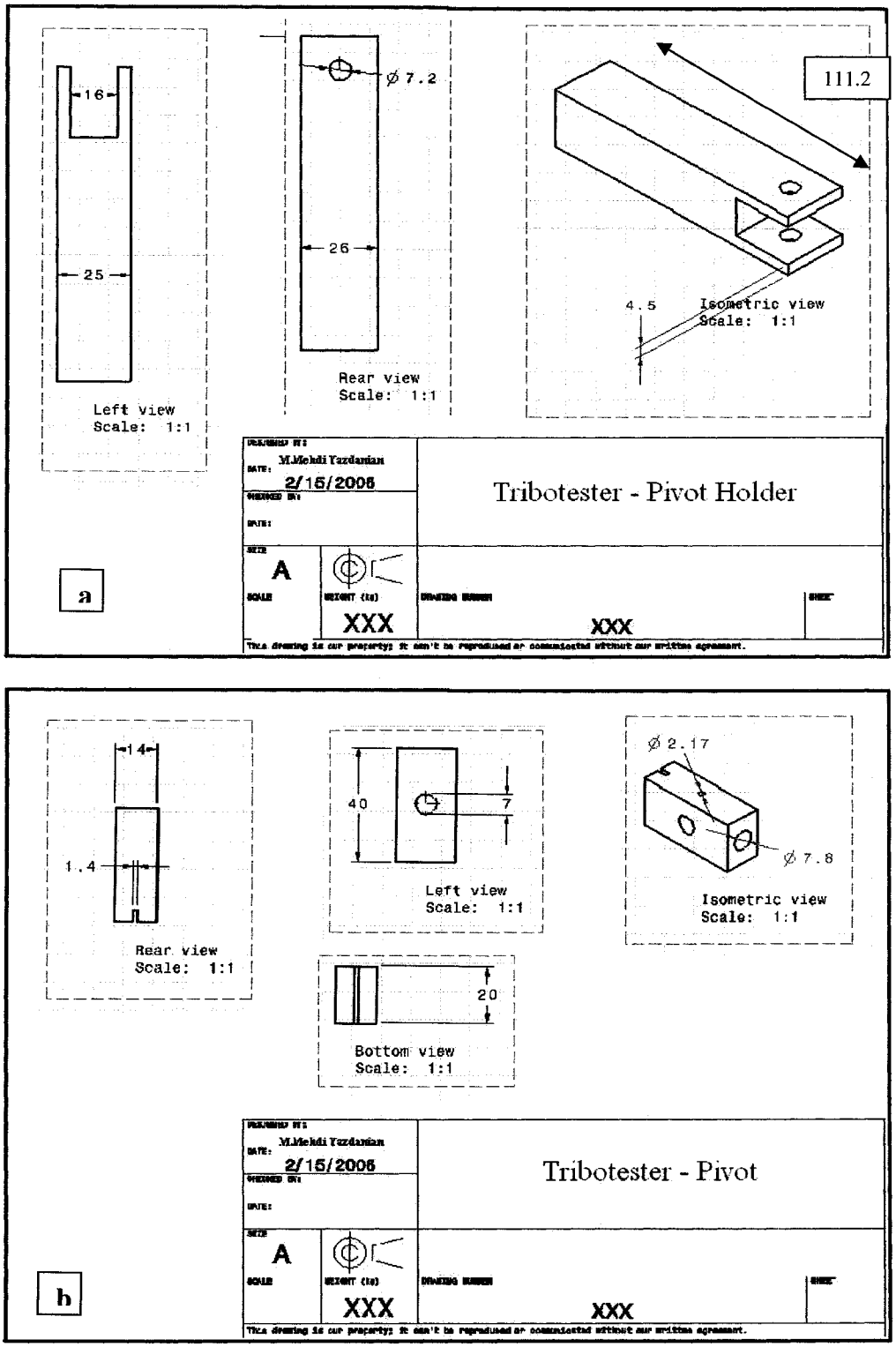

Figure.3 Tribo-tester part: (a) Pivot, (b) pivot holder (sizes are in mm)

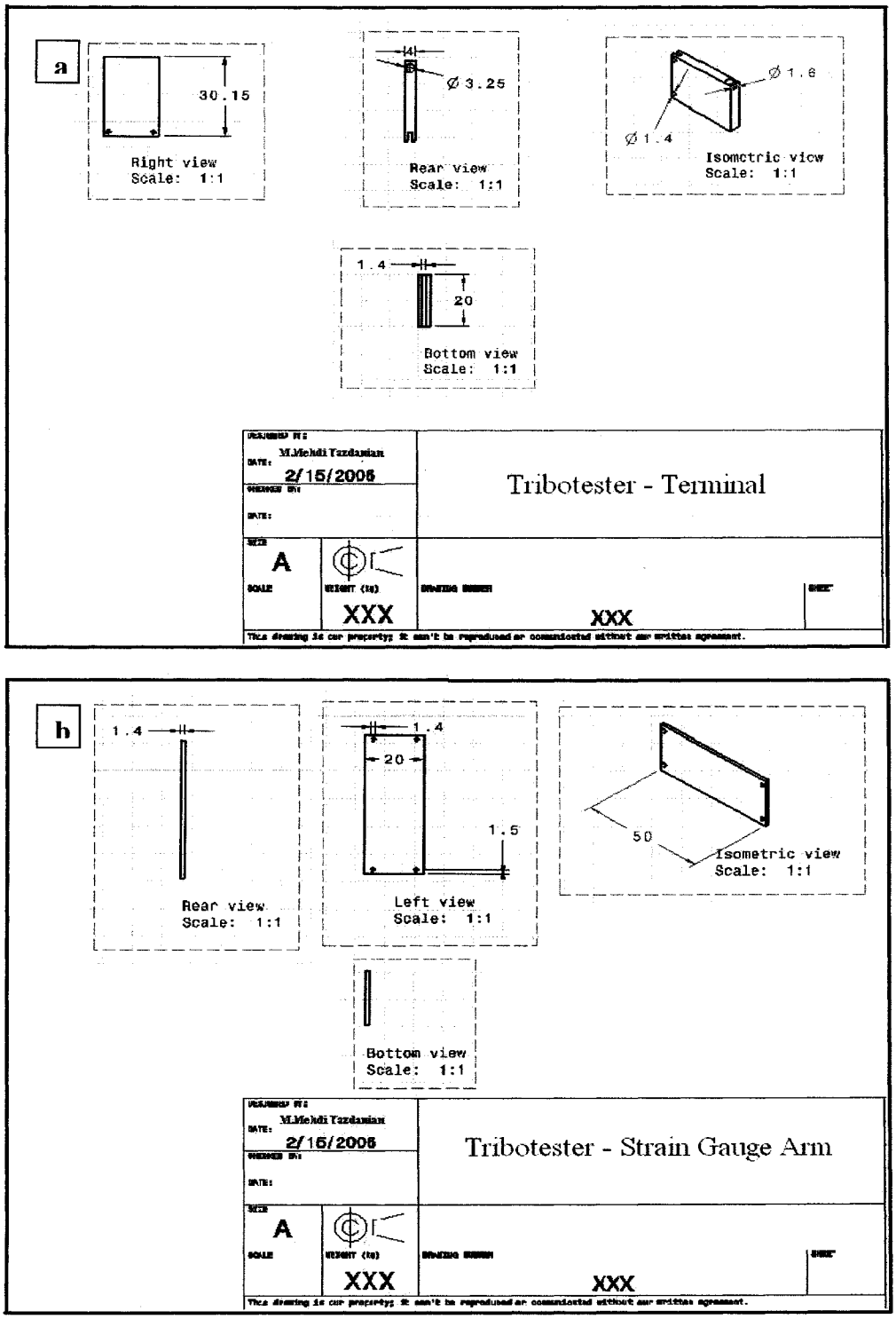

Figure.4 Tribotester part: Disk Holder (a) terminal, (b) strain gauge arm (sizes are in mm).

VITA AUCTORIS

M. Mehdi Yazdanian was born in 1973 in Tehran. He received his first university degree in Mechanical Engineering (Fluid Mechanics) from Mazandaran University in 1998. After moving to Canada, he continued his education in Master of Science (Physics) and graduated from Brock University in St.catharines, Ontario. He is currently a candidate for the Master's degree in Engineering Materials at the University of Windsor.